2009

Effective Simulation and Optimization of a Laser Peening Process

Gulshan Singh
Wright State University

Effective Simulation and Optimization of a Laser Peening Process

A dissertation submitted in partial fulfillment
of the requirements for the degree of the
Doctor of Philosophy

By

GULSHAN SINGH
B.S., Jai Narain Vyas University, Jodhpur, India, 2001
M.Tech., Indian Institute of Technology, Kanpur, India, 2003

2009
Wright State University

Wright State University
SCHOOL OF GRADUATE STUDIES

August 10, 2009

I HEREBY RECOMMEND THAT THE DISSERTATION PREPARED UNDER MY SUPERVISION BY GULSHAN SINGH ENTITLED Effective Simulation and Optimization of a Laser Peening Process BE ACCEPTED IN PARTIAL FULFILLMENT OF THE REQUIREMENTS FOR THE DEGREE OF Doctor of Philosophy .

_____

Ramana V. Grandhi, Ph.D.
Dissertation Director

_____

Ramana V. Grandhi, Ph.D.
Director, Engineering Ph.D. Program

_____

Joseph F. Thomas, Jr., Ph.D.
Dean, School of Graduate Studies

Committee on Final Examination

_____

Ramana V. Grandhi, Ph.D.

_____

Nathan Klingbeil, Ph.D.

_____

Ravi Penmetsa, Ph.D.

_____

Allan H. Clauer, Ph.D.

_____

Robert Brockman, Ph.D.

Abstract

Singh, Gulshan, Ph.D. in Engineering Program, Wright State University, 2009. Effective Simulation and Optimization of a Laser Peening Process.

Laser peening (LP) is a surface enhancement technique that has been applied to improve fatigue and corrosion properties of metals. The ability to use a high energy laser pulse to generate shock waves, inducing a compressive residual stress field in metallic materials, has applications in multiple fields such as turbomachinery, airframe structures, and medical appliances. In the past, researchers have investigated the effects of LP parameters experimentally and performed a limited number of simulations on simple geometries. However, monitoring the dynamic, intricate relationships of peened materials experimentally is time consuming, expensive, and challenging.

With increasing applications of LP on complex geometries, these limited experimental and simulation capabilities are not sufficient for an effective LP process design. Due to high speed, dynamic process parameters, it is difficult to achieve a consistent residual stress field in each treatment and constrain

detrimental effects. With increased computer speed as well as increased sophistication in non-linear finite element analysis software, it is now possible to develop simulations that can consider several LP parameters.

In this research, a finite element simulation capability of the LP process is developed. These simulations are validated with the available experimental results. Based on the validated model, simplifications to complex models are developed. These models include quarter symmetric 3*D* model, a cylindrical coupon, a parametric plate, and a bending coupon model. The developed models can perform simulations incorporating the LP process parameters, such as pressure pulse properties, spot properties, number of shots, locations, sequences, overlapping configurations, and complex geometries. These models are employed in parametric investigations and residual stress profile optimization at single and multiple locations.

In parametric investigations, quarter symmetric 3*D* model is used to investigate temporal variations of pressure pulse, pressure magnitude, and shot shape and size. The LP optimization problem is divided into two parts: single and multiple locations peening optimization. The single-location peening optimization problems have mixed design variables and multiple optimal solutions. In the optimization literature, many researchers have solved problems involving mixed variables or multiple optima, but it is difficult to find multiple solutions for mixed-variable problems. A mixed-variable Niche Particle Swarm Optimization (MNPSO) is proposed

that incorporates a mixed-variable handling technique and a niching technique to solve the problem.

Designing an optimal residual stress profile for multiple-location peening is a challenging task due to the computational cost and the nonlinear behavior of LP. A Progressive Multifidelity Optimization Strategy (PMOS) is proposed to solve the problem. The three-stage PMOS, combines low- and high- fidelity simulations and respective surrogate models and a mixed-variable handling strategy. This strategy employs comparatively low computational-intensity models in the first two stages to locate the design space that may contain the optimal solution. The third stage employs high fidelity simulation and surrogate models to determine the optimal solution. The overall objective of this research is to employ finite element simulations and effective optimization techniques to achieve optimal residual stress fields.

Contents

List of Figures

List of Tables

.

Dedicated to

my wife

ACKNOWLEDGEMENTS

I would like to thank my advisor, Professor Ramana V. Grandhi, for his help in the performance and critique during this research.

I would also like to extend my thanks to the Ph.D. committee members: Dr. Nathan Klingbeil, Dr. Ravi Penmetsa, Dr. Allan Clauer, and Dr. Robert Brockman. My thank also goes to my friends, Mr. Hemanth Amarchina, Dr. Todd Benezer, Dr. Jong-bin Im, Jason King, Justin Maurer, Inseok Park, Matthew Reliy, T J Spradlin, and Randy Tobe whose friendship and encouragement were always with me during my Ph.D. research work. I would also like to thank Alysoun Taylor, whose corrections and suggestions on English style and grammar is really appreciated. I am also grateful to Dr. Kalyanmoy Deb of Indian Institute of Technology Kanpur, who introduced me to the field of optimization and patiently taught many valuable lessons.

I would like to thank Dr. David Stargel and Dr. Kristina Langer for their support, feedback, and help during the research. I would like to acknowledge the support from the Wright-Patterson Air Force Base under grant FA8650-04-D-3446-25 and from the Ph.D. fellowship granted by the Dayton Area Graduate Studies Institute (DAGSI).

I would like to give my special thanks to my parents, Harpal and Maghar Singh, my brother and his family, Balvinder Singh, Jaspal Kaur, Chandan, and Mukul for their continuous support that enabled me to complete this work. I would like to thank my son Gahan Singh.

And finally, I am greatly indebted to my lovely wife, Meenakshi Singh, who always believed in me. I would like to express my heartfelt gratitude and admiration to her for her constant love and trust in me. Without her support, I would not have made it through the program. We have made it together as a family.

Chapter 1

Surface Enhancement Techniques

Material is subjected to degradation from the moment it is prepared. Mechanical, chemical, or thermal loading continues to degrade the material throughout its lifetime. Damage by fretting, fatigue, corrosion, and wear are a few examples of the degradation that can inflict a cost penalty on a material by requiring design changes to accommodate degradation. Material damage can also cause loss of performance. Most types of material degradation tend to originate at the surface of a component. The objective of surface enhancement techniques is to inhibit degradation by altering material properties at the surface and to maintain the required level of performance without imposing high cost implications. However, it is an intriguing, but challenging to achieve the objective by tailoring the surface enhancement techniques. In this research, a simulation-based strategy is employed on a selected surface enhancement technique to engineer optimal surface properties.

The main focus of this research is the surface enhancement technique called

Laser Peening (LP). In the LP process, favorable residual stresses are induced on a surface to improve fatigue and fretting properties of metals. In the literature, experimental [1–7] and simulation [8–11] work have been performed to drive maximum benefits from the process. However, time consuming and expensive experiments and limited simulations on simple geometries are not sufficient for optimal LP process design. A comprehensive procedure is required that can not only perform simulations but also can be employed in obtaining optimal process parameters.

The overall goal of this chapter is to provide a brief introduction of surface enhancement techniques and to present a detailed description of a specific process called Laser Peening. This chapter begins with Section 1.1, an introduction to surface enhancement techniques such as shot peening, low plasticity burnishing, and waterjet peening, and their use in manufacturing processes. Section 1.2 presents an introduction to the LP process. The next three sections present the laser generation mechanism, component preparation, and shock wave propagation. In Section 1.3 includes, a preliminary explanation of a laser generation mechanism. Section 1.4 presents component surface preparation details. After the component is prepared, a laser is fired on the surface. Section 1.5 deals with the shock wave propagation and residual stress generation in a component. Section 1.6 discusses the advantages and disadvantages of LP compared to other mechanical surface enhancement techniques. Section 1.7 presents the organization of the dissertation, and the final section summa-

rizes the chapter.

1.1 Surface Enhancement Processes

Connecting rods in automobiles, turbine blades in aircraft engines, and lugs in aircraft structures are a few components that experience material damage due to fretting and fatigue loading conditions. These type of loads cause failure by initializing and propagating cracks. In the case of turbine engines, foreign object damages result in early crack initiation and growth, causing a decrease in fatigue performance. The possibility of such failures leads to increased inspection and maintenance expenses because the failure of one critical component limits the operational time and service life of the entire system. Fatigue can cause catastrophic failure, leading to structural and automobile failure, aircraft losses, and, at worst, loss of life. Apart from standard design requirements and inspections, many material treatments have been developed to mitigate such failures. Surface enhancement techniques treat the intended surfaces to improve the desired surface properties. These techniques are becoming an integral part of manufacturing processes because the behavior of manufactured parts is dependent on the structure and properties both of bulk material and of the surface.

Every metallic material consists of a micro-structure of small crystals called grains or crystallites. The properties of these grains (i.e. grain size, orientation, and composition) determine the overall behavior of the material. Mate-

rial treatment (and/or surface enhancement techniques) provides an efficient way to influence the properties of the metal by controlled processes. These material treatments are generally classified into mechanical, thermal, thermo-mechanical, and thermo-chemical treatments. In the case of mechanical treatments, some form of mechanical force is employed to modify the properties of the material to the advantage of an application. Common mechanical treatment techniques are shot peening, low plasticity burnishing, water jet peening, cold rolling, and case hardening.

In the case of thermal treatments, some form of temperature controls are used to modify material properties. Common thermal treatment techniques are hardening, tempering, and annealing. Hot rolling and plating are examples of thermo-mechanical treatment, a category that combines the effect of both mechanical and thermal treatments. In the case of thermo-chemical treatments, a metallic or non-metallic coating is applied on the surface. Painting, oxidizing, and vapor deposition are a few examples of thermo-chemical treatments. Depending upon the usage, a few of these processes are also referred to as surface enhancement techniques. Surface enhancement techniques have significant industrial applications. The following section talks about mechanical surface enhancement techniques.

1.1.1 Shot Peening

Shot peening (SP) is a traditional surface enhancement technique that has been used for more than six decades. SP was discovered and patented by Lockheed Aircraft Corporation in Burbank, California in the late 1940's. For example, Boeing Commercial Aircraft Company have standard setup to peening aircraft components [12]. Many other companies are using SP, or a modified form, Glass Bead Peening (GBP), to improve fatigue life of mechanical components. In the SP process, small, spherical metal or ceramic balls are bombarded on the surface to be peened. In the GBP process, glass balls are used instead of metallic balls. This bombardment creates elastic and plastic deformation. This deformation tends to produce compressive stress on the surface and tensile stress in the interior. The schematic of the SP process is shown in Figure 1.1. SP results in a small depth of induced compressive residual stress. This process results in a roughened surface due to the physical contact between the bombarding ball and the peened component. This effect is more severe in soft materials, and may not be an ideal process if the surface finish is an important factor for a product. With proper parameters, the SP technique [13–17] is used to induce compressive residual stresses in components. The physical principle of changing the mechanical properties is approximately the same for most mechanical surface enhancement techniques. The principle is that elastic and plastic deformation result in residual stress generation. This generation is studied in detail in Section 1.2.

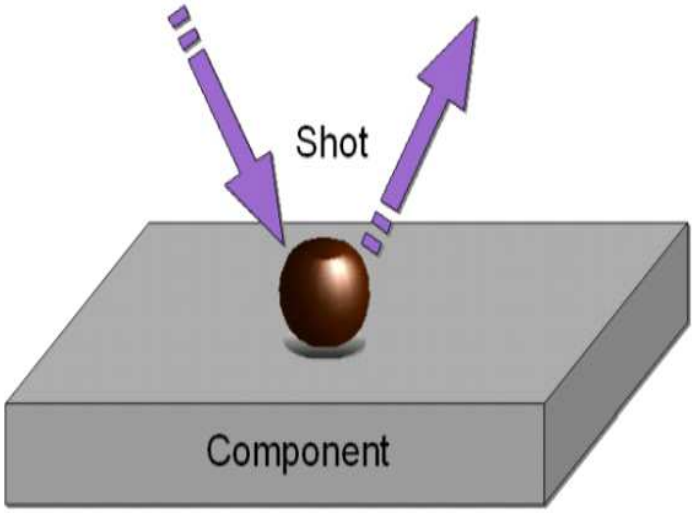

Figure 1.1: Schematic of shot peening process

1.1.2 Low Plasticity Burnishing

Low Plasticity Burnishing (LPB) is a recently developed (1998) surface enhancement technique. The LPB process [18, 19] consists of rolling a high-modulus ball or roller over the intended surface of the component (Figure 1.2). Depending upon the controlling parameters, this process alters the mechanical behavior of the material by low-cold working, just like SP. This is a low-cost, easy-to set-up process that provides a better surface finish compared to SP. An advantage of this process is that it can be carried out in any numerically controlled apparatus, including a lathe, mill, or CNC machine. The surface finish obtained depends upon the finish of the ball used in LPB process; the ball is a wear-prone component. Just like SP, this process produces elastic and plastic

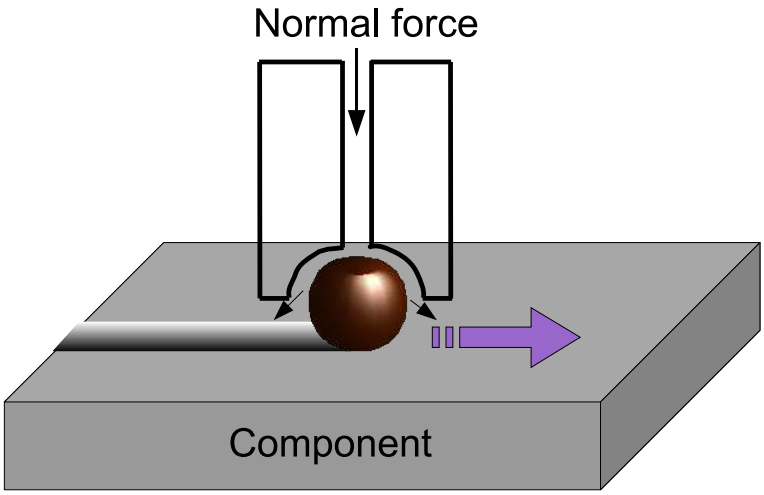

Figure 1.2: Schematic of the low plasticity burnishing process

deformation by contact between the burnishing ball and the surface. A disadvantage of the LPB process is that it is difficult to apply to curved or complex geometries.

1.1.3 Waterjet Peening

High pressure waterjets have been studied to understand the mechanisms associated with the jet material interface and to apply it to multiple processes such as cleaning, cutting, and paint removal. The application of an ultra-high-pressure waterjet as a surface enhancement technique is relatively new (2000) compared to SP and LPB. Waterjet Peening or Water Peening (WP) [20, 21] is similar to SP except that it uses high pressure droplets that disintegrate in the waterjet flow field instead of solid shots [22]. Compared to other available techniques, the lower cost, the absence of heat that could affect the region, and a clean surface are the major advantages of the process. The WP process is a

physically complex technique that is difficult to model and requires extensive further research.

1.2 Laser Peening

High-power Light Amplification by Simulated Emission of Radiation (LASER) is used in many manufacturing processes of aircraft engine and airframe structures, such as laser drilling, welding, and glazing. LP is a surface enhancement technique for metallic components that uses the shock wave generation capability of lasers to induce favorable residual stresses. Apart from improving fatigue life, LP has also been applied to improve fretting and corrosion properties.

The ability of a pulsed laser beam to generate shock waves was first recognized and explored in the early 1960's. Initial facilities were developed and feasibility studies were performed at Battelle Laboratories in Columbus, OH. Also at Battelle, researchers succeeded in the application of LP to enhance fatigue properties of fastened joints for aeronautical applications. After this success, further research was performed to examine various fundamental principles such as the confined interaction mode, the dielectric breakdown factor, and analytical modeling of the physical process involved. As a result of these numerous efforts, LP is emerging as an alternative and complementary process to conventional peening processes.

Compared with traditional surface enhancement techniques such as SP and

LPB, a higher depth of compressive residual stress and a lower cold-work amplitude are obtained from the LP treatment. Among the major advantages of the LP process, four important ones are the absence of contact (prevents severe relief of residual stresses during cyclic loading), better surface finish than shot peening, precise parameter control, and the ability to peen complicated geometries.

1.2.1 Laser Generation

To generate a laser [23,24], the atoms and molecules of a crystal, gas, or liquid are excited so that more of these are at higher energy levels than are at lower energy levels. When a photon of the frequency that corresponds to the energy difference between the excited and lower states strikes an excited atom, this process causes atoms to fall back to a lower energy state and to emit a second photon of the same or a proportional frequency, in phase with and in the same direction as the striking photon. This process is called stimulated emission, in which an atom is stimulated to produce a second photon. The striking and the emitted photon may stimulate further atoms to emit photons, all with the same frequency and phase. This process is a rapid chain reaction that produces a sudden burst of coherent radiation as all the atoms discharge.

Based on different laser parameters, there are many varieties of lasers available. The intensity, duration (mid-span), and wave length of the laser are significant properties. In the case of the LP process, these properties should

be such that the laser produces the required volume, depth, and magnitude of residual stress in the peened material. The LP process requires a laser with high power (100 to 1000 watts), moderate frequency (10 to 50 shots per minute), and high laser pulse energy (100 Jules) for suitable industrial applications. A very high repetition rate may not be needed because in the LP process, repetition is limited setup for each shot. Consequently, the laser peening speed is limited by component preparation time rather than laser frequency.

1.2.2 Component Preparation

The ability of a laser to create stresses in a metal component was recognized far in advance of its practical application. In the process of bringing LP to the level of industrial application, the use of opaque and transparent overlays have played a significant role. To generate plasma, the component surface must be painted with an opaque overlay. The sudden expansion of plasma causes a pressure pulse in the metal. The pressure pulse peak and mid-span can be increased if the surface is confined with a transparent overlay. The role of overlays is further discussed in the following sections.

Opaque Overlay

When the laser beam is directed onto the surface, it passes through the transparent overlay and strikes the opaque overlay. This produces a high temperature of the order of $10,000^{o}F$ during the plasma creation stage. Direct contact

of a metal surface with the high temperature plasma will, in most cases, form a thin melted layer. Therefore at the nascent stage of the process, the metal component is covered with a protective coating to avoid the thermal effects of such high temperatures.

However, the role of this coating has changed over time. At present time, the opaque overlay has two purposes: augmenting the creation of plasma and providing protection of the component surface to be peened. For the first purpose, the opaque overlay supplies material for plasma creation. For the second purpose, it provides protection to the component surface from high temperature. Because of this protection, the material undergoes reduced thermal and micro-structural changes. If allowed, these thermal and micro-structural changes can alleviate the required effects of LP. The important factors in selecting an opaque overlay material for a particular material surface are the cost, ease of application and removal, layer thickness, interaction with laser, opaque integrity for multiple shots, applicability over complex geometries, disposal of used opaque material, and repeatability. Among all opaque coatings black paint, aluminum, zinc or copper and organic coating are used commonly. These are preferred because of the ease of handling and disposal.

Transparent Overlay

When a dielectric material, transparent to laser light, is placed over the opaque overlay, plasma created by LP is trapped between the component and the trans-

parent overlay. This trapping increases the pressure pulse magnitude by factors of 5 (for the peak pressure level) and 3 (for the pulse mid-span/duration) compared to a direct ablation mode.

In industrial applications where a large number of shots is needed in less time, water is used most often for the overlay because of ease of availability and handling. However, solid overlays of glass, fused quartz, and acrylic have also been used. As with the opaque overlay, the cost, speed of control, ease of application and removal, and ease of clean-up and disposal are major factors in selecting the transparent overlay.

Along with these factors, dielectric breakdown thresholds, degree of transparency, acoustic impedance, and control of thickness also affect selection of the overlay. Proper selection of the transparent overlay is important because it ultimately affects the peak and duration of the shock wave in the material. It is important to remember that in the industrial application of opaque and transparent overlays, a traditional manual application of overlays may not be most suitable. Instead, a liquid jet is used for efficient processing, as shown in Figure 1.3. These jets and the laser beam must be properly sequenced to produce the desired results. Proper positioning of the component is also necessary for successful completion of the process.

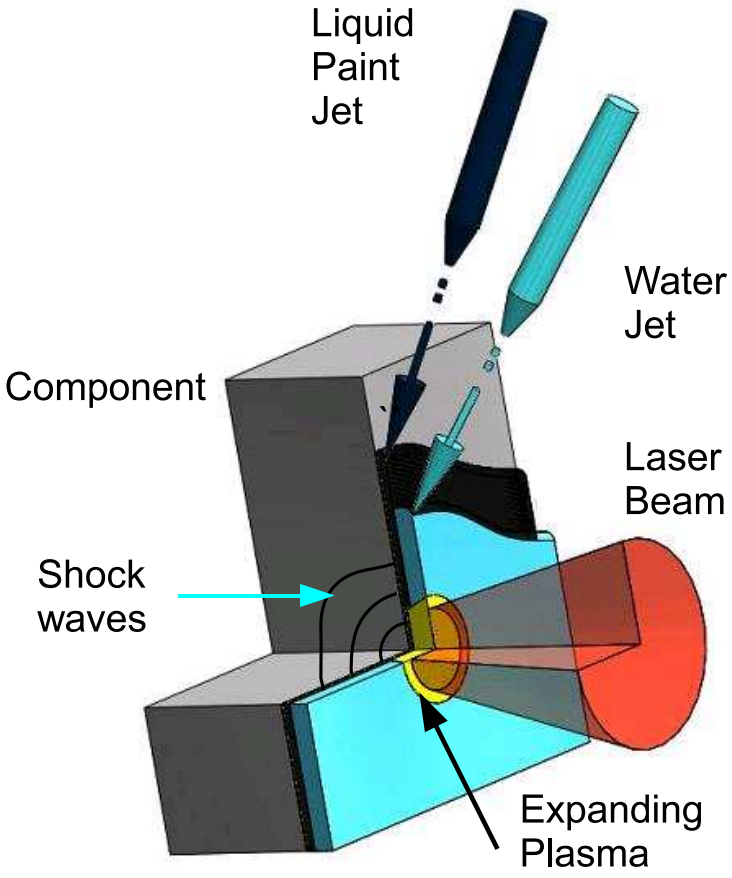

Figure 1.3: Schematic of Laser Peening process

1.2.3 Residual Stresses

The component surface to be peened is coated with a opaque material and covered with a transparent overlay. When the component is ready for peening, a high energy laser is fired on the prepared surface. The laser passes through the transparent layer and causes the opaque overlay to vaporise and then convert into plasma when it absorbs more energy. As the vapor continues to absorb the laser energy, it expands. As the confined plasma expands, it generates a high pressure, short duration shock wave that travels into the base material and the water. The presence of water tends to confine the energy and increase the intensity of the pressure pulse in the component. Depending upon the magnitude of the pressure wave in the base metal, this can cause elastic and plastic deformation. This deformation generates compressive and tensile residual stresses. The mechanics of the residual stress generation process are explained below.

Shock Wave Propagation

Depending upon its magnitude, an LP pressure pulse can cause plastic deformation in the top region of a component. As the shock wave progresses through the component, its magnitude is reduced according to the attenuation rate. After a certain depth, the shock wave magnitude is below the proportional limit and can only cause elastic deformation. The final outcome of the process is a residual stress field in the component. The top region of the component tends to have compressive stresses, followed by a tensile region beneath it.

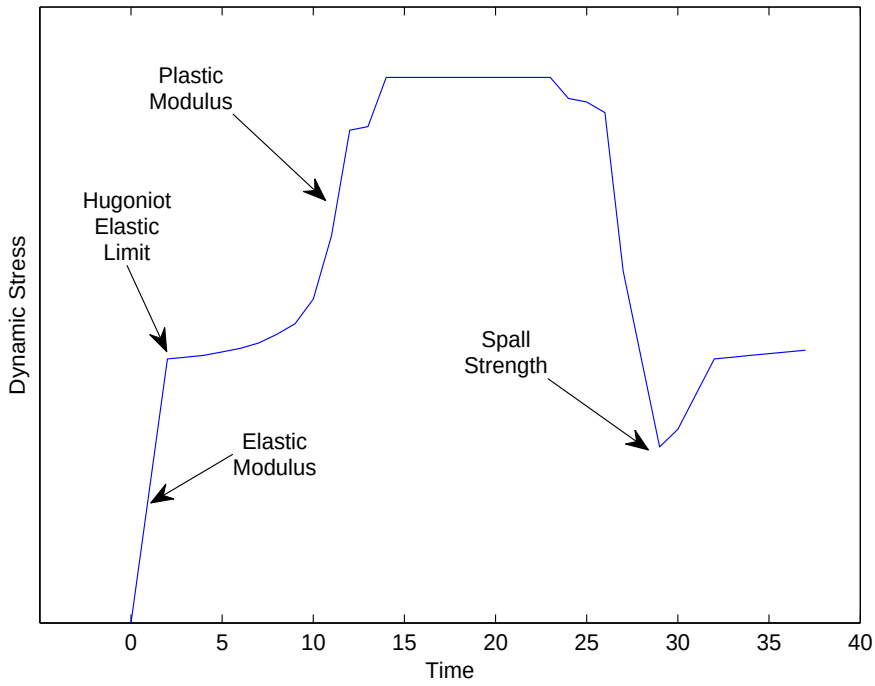

Figure 1.4: Shock wave in a material

In general, the study of stress propagation in a non-linear medium is extremely difficult. This section describes the physical behavior of the material under LP loading. Material behaves differently under different strain-rates. In the case of LP loading, a typical strain-rate is up to $10^6/s$, which is extremely higher than conventional strain-rates of $10^{-6}/s$. This higher strain-rate is referred to as shock wave or impact loading. Material behaves differently under static (or low strain-rate) and dynamic (high strain-rate or shock wave, $> 10^3/s$) loadings because higher stress is necessary to reach the yield limit in an impact loading than in case of slow loading.

The dynamic yield strength of a material is a function of strain, strain-rate, and temperature. When a shock wave of a magnitude above the dynamic yield

strength limit travels through a material, it takes a certain shape (Figure 1.4) based on the pressure magnitude and material properties [25,26]. An important parameter for this shape is the Hugoniot Elastic Limit (HEL), which is defined as the axial stress required for plastic deformation in a uniaxial strain state. The relationship between the HEL (σ_{HEL}) and the dynamic yield stress (σ_{yd}) is

$$\sigma_{yd} = \sigma_{HEL}\left(\frac{1-2\nu}{1-\nu}\right) \tag{1.1}$$

where ν is Poission's ratio.

LP pressure, when applied, generates two stress waves, elastic and plastic, in the material [25, 26]. According to stress wave propagation theory, the speed of the elastic (V_e) and plastic (V_p) waves are given in Eqs. 1.2 and 1.3, respectively.

$$V_e = \left[\frac{E(1-\nu)}{(1+\nu)(1-2\nu)\rho}\right]^{1/2} \tag{1.2}$$

$$V_p = \left[\frac{E}{3(1-2\nu)\rho}\right]^{1/2} \tag{1.3}$$

where ρ denotes mass density and E denotes Young's modulus. The speed of the elastic wave (Eq. 1.2) is faster than the plastic wave (Eq. 1.3). When the applied pressure is removed, an unloading (release) wave travels in the same direction. If the loading is compressive, then the release wave is always tensile.

The LP-generated elastic wave travels until it reaches the boundary of the material and then reflects back. The speed of the release wave is greater than a plastic wave, so depending upon the loading time, it is possible for the waves to

meet. The release wave reduces the amplitude of the plastic wave and reflects back toward the starting surface. In the meantime, the first elastic wave, which reflected back from the boundary of the component, also meets the plastic wave. There is a complicated wave interaction that takes place between these waves. The timing of the interactions between these waves can be different depending upon many factors such as the material properties, the relative speed of the elastic and plastic waves, and the total length of the component. This results in a complex distribution of elastic and plastic strains and stresses, ensuring complex dynamic response in the laser-peened material. Therefore, the dynamic responses of the laser peened material are complex. To understand the above phenomenon and predict the final residual stress profile, an effective simulation methodology is required.

Residual Stress Generation

The complicated interactions between different waves inside the material produce compressive and tensile stress regions. The compressive stress dominates in the top region of the component. Below this compressive stress region, there is a tensile stress region. The magnitude of the tensile stress is less than that of the compressive stress. However, the volume of the tensile stress region is higher than the volume of the compressive region. Depending upon component geometry, material properties, and pressure pulse properties, the tensile region may be in between the two compressive regions. Depending upon the

material properties and the component dimensions, the compressive region at the bottom may or may not be present. The presence of compressive stress tends to reduce the chances of crack initiation and growth. The tensile stress region is generated to balance the compressive stress for equilibrium in the absence of external force.

The physics behind this complex formation of stress is explained below. Figure 1.5 shows a schematic of the residual stress generation and distribution. Above the elastic limit, pressure causes the surface layer of the target to

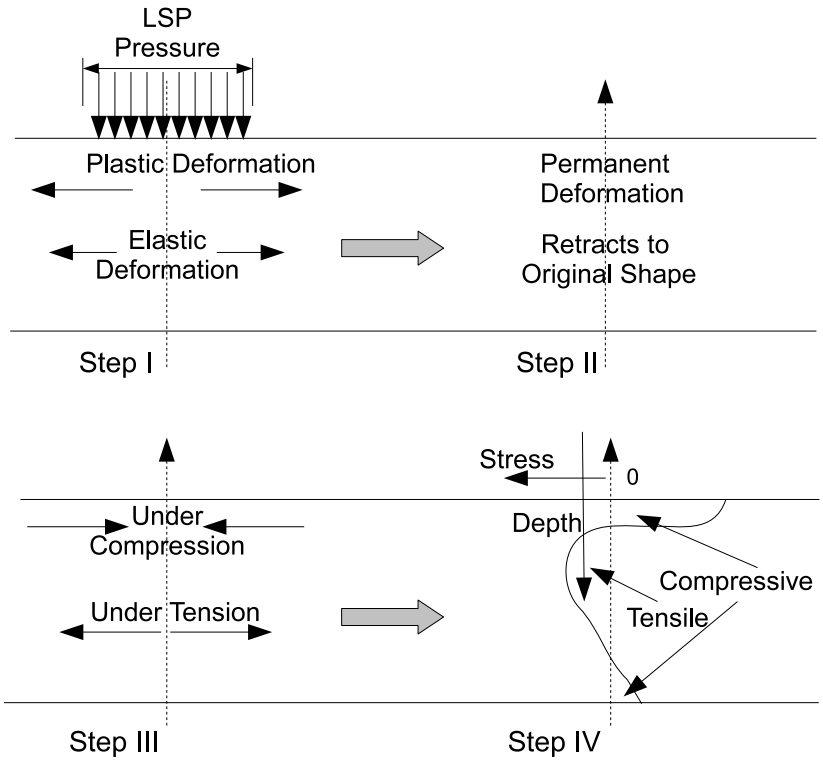

Figure 1.5: Schematic of residual stress generation

expand beyond the elastic limit. Depending upon the magnitude of the pres-

sure, the layer below the surface layer also expands, but within the elastic limit. This expansion is in the normal direction to the applied pressure. According to the attenuation rate, the expansion reduces along the depth in the target. After a certain depth, the expansion is elastic.

The elastically deformed part of the component attempts to return back to its original shape, but plastic deformation is permanent. Therefore, as shown in Figure 1.5, the top layer of the target is subjected to compressive stress, and the area below this layer is subjected to tensile stress, maintaining equilibrium in the target without external force. An increase in the compressive stress volume or magnitude will always come with an increase in the tensile stress volume or magnitude. An advantage of the LP process is a higher depth of compressive stress as compare to other peening processes. The depth of compressive stress is directly related to the depth of plastically affected zone. Ballard et al. [27, 28] provided an empirical expression for plastically affected depth (D_p) and surface residual stress (σ_{surf}).

$$D_p = \left(\frac{V_p V_e \tau}{V_e - V_p}\right)\left(\frac{P - \sigma_{HEL}}{2\sigma_{HEL}}\right) \tag{1.4}$$

$$\sigma_{surf} = \mu\varepsilon_p \left(\frac{1+\nu}{1-\nu}\right)\left(1 - \frac{4\sqrt{2}}{\pi}(1+\nu)\frac{D_p}{a}\right) \tag{1.5}$$

Here, V_e, V_p, τ, P, and σ_{HEL} indicate the elastic wave speed, plastic wave speed, shear stress, shock wave pressure, and Hugoniot Elastic Limit of the material. And μ, ε_p, a indicate pulse duration, plastic surface strain, and the

side of square impact. Equations 1.4 and 1.5 indicate plastically affected depth and surface residual stress, respectively. The LP process parameters can be optimized to generate a higher volume of compressive stress with constraints on depth of compressive stress and on magnitude of tensile stress.

1.2.4 LP Advantages and Disadvantages

This section lists the advantages and disadvantages of the LP process.

- It is well known that the cyclic behavior of mechanical components depends on the metallurgical, mechanical, and geometrical surface states of the material involved. Many experimental and practical results have proved that fatigue properties are improved by LP.
- A critical drawback of SP is that residual stresses are induced by the contact between the bombarding ball and surface; hence residual stresses tend to relax quickly under repeated loading. Since there is no contact during the LP treatment, residual stresses tend to relax more slowly than SP.
- In the case of SP or LPB, the surface of the ball or the roller tends to degrade with prolonged usage. This degradation leads to a rough surface finish on the target component. The LP process does not use any physical tool to induce residual stress.
- As mentioned in Section 1.2, the applicability of LP to complicated geometries is a unique advantage, made possible because a laser is a collec-

tion of rays that can reach any intricate location within a bulky apparatus.

- The cost of LP is relatively high; however, the cost should decrease as the advances in laser technology continue.
- For a successful surface enhancement technique, complete control of the process is essential to generate the required residual stress field. Otherwise, a technique may carry some risk. In the application of SP, many probabilistic parameters, such as area of contact, angle of contact, and speed of strike, are involved. These make the process difficult to control. LP is a comparatively controllable and repeatable process.
- Although LP is a controllable process, it tends to produce non-uniform residual stress across the laser spot. This non-uniformity depends upon the metallurgical properties of the peened component.

1.3 Dissertation Organization

This dissertation is organized in the following order:

- Chapter 1 describes the step-by-step LP process in detail. This includes brief description of laser generation, overlay application, shock wave propagation, and residual stress generation. The physics behind the generation of residual stress is also discussed.
- Chapter 2 presents a literature review, starting from the initial inventions of the laser-induced pressure pulse to the current status of LP and finite

element (FE) simulation of the process. This chapter also covers experimental and empirical work. The literature review is followed by a discussion of the current needs of LP research. The motivations of this research are listed at the end of the chapter.

- Chapter 3 shows the different modeling parameters of the LP process, and available simulation methodology from the literature. A modified methodology is presented, which is then used model a sequential, multiple-location LP treatment, a parametric plate model, and a coupon model. Once developed, this methodology can be used to perform LP simulations of a representative realistic component.

- Chapter 4 presents the background of optimization and the issues faced when solving the mixed-variable design optimization problem of the LP process. Gradient- and non-gradient-based optimization methods are introduced. The simulation developed in Chapter 3 is employed to perform parametric studies of the LP parameters.

- Chapter 5 discuss the idea that one location laser peening is a multimodal mixed-variable optimization problem. To effectively solve the problem a multimodal mixed-variable optimization method is proposed. This method is tested on multimodal problems and successfully implemented to solve the LP problem.

- Chapter 6 presents a strategy to optimize multi-location laser peening. The

proposed strategy employs multi-fidelity and surrogate models to address the issue of computational cost.

- Chapter 7 concludes the dissertation with the list of contributions, summary, and future work.

1.4 Chapter Summary

This chapter presents surface enhancement techniques, justification of LP, and a brief overview of LP. LP process details are discussed, such as the opaque and transparent overlays, laser generation, shock wave propagation, and residual stress generation. In the overall research, this chapter serves to demonstrate a comprehensive understanding of the process and of the physics involved.

Chapter 2

Literature Survey

The introduction and theoretical background presented in Chapter 1 make it clear that LP is a complex and intricate process. An extensive amount of work has been done to bring the LP process to its current level of industrial applications. However, little has been done to develop an effective simulation procedure, using FE analysis, that relates the LP parameters to material properties (fatigue and fretting strength). Neither has there been any effort toward process optimization and reliable design. FE simulations help in understanding the process. An overall history of the process development is presented in this chapter. There are two major aspects of the LP development to the current stage. The first aspect is the initial inventions of the technology. The second aspect is the improvements so far and challenges ahead for the LP process. There are three sections in this chapter: initial discoveries, developments that have led to the current stage, and challenges and motivation for this research.

2.1 Initial Developments

Initially, White [29] identified the shock wave generation ability of high-energy pulsed lasers. This discovery led to investigations of laser-generated applications [30]. This ability was explored in many aspects [31, 32] including altering material properties [33], producing vacancies in thin vanadium and nickel foils [34], and detonating explosives [35]. In one of the investigations by Fairand [36], it was discovered that a laser-generated pressure pulse can alter in-depth material properties in metals. It was observed that the yield strength of Aluminum was improved by laser-induced shocks, without significantly affecting the ultimate tensile strength [36]. In 1974, a patent was issued to Malozzi and Fairland [33] for LP's use in modification of material properties. Upon observing that a higher pressure pulse produces a higher shock wave, Anderhlom [37] established that higher pressure can be achieved by applying confined ablation.

After these inventions, Clauer et al. [1, 2, 38, 39] and Fairand et al. [3–5, 36] performed a number of investigations at Battelle Columbus Laboratories, Ohio (USA) between 1968 and 1991, exploring the potential of this technology. Many researchers, such as Fox [40], Ford et al. [41], Ortiz and Penny [42], and Forget [43], also contributed to the development of the process. Fairand and Clauer [4, 5] delved into the characteristic of the laser–material interaction and the material response to the induced shock waves. In this research, the

peak pressure was investigated for different ablative overlays and the effects of LP on welded joints was reported. After these investigations, LP was applied to improve the fatigue life of fastener holes [6]. Fairand and Clauer also performed systematic investigations of the parameters that significantly affect the LP process. These works led to the first well-known successful industrial use of LP in aircraft gas turbine blades [44] for increased foreign-object damage resistance. Fox [40] investigated the effects of coating on the target surface. Ford et al. [41] showed that a decrease in crack growth rate can be achieved by careful selection of the process parameters under specific conditions. Ortiz and Penny [42] obtained a patent for developing an LP system that includes a foil aligned with a surface of the workpiece to be peened and lasing the aligned foil surface. This system improved the speed of peening and accuracy of peening control. Forget et al. [43] studied the laser beam optical phenomena and deformation mechanisms and proposed an analytical model for predicting residual stresses.

2.2 Growth Challenges

The success of initial results generated interest in further investigations [38, 39, 41, 45], followed by industrial applications [42, 46] of the technology. Many researches showed the benefits of the technology and produced extensive literature. After the initial demonstration of the technology proved it to be beneficial for intended material properties, the number of LP applications grew

rapidly [47]. At this stage, this enabling technology faced many challenges. The first challenge was to develop a mechanism that could deliver a powerful, controllable, and repeatable pressure pulse at a high frequency. The second challenge was to develop a comprehensive knowledge of the process and a numerical tool to predict the generated residual stress field. The understanding of the process can guide the research in the field and could assist in developing a numerical tool. The third challenge was to accurately predict and document the benefits of the LP process on material strength. Overcoming these challenges could take the technology to the next level, allow an optimal use of the technology, and facilitate reduction in the cost of industrial applications.

This section presents the research work performed to overcome the first challenge. The pressure generated by a laser pulse provides a controllable and reproducible tool for practical material shock processing applications. Research in the confinement regime [37, 40, 43, 48–51] and laser systems [52] provided a potential solution to obtain compatible pressure pulse properties. Anderhlom [37] observed that plasma pressure was significantly increased by the presence of confinement (as compared to no confinement). Fox [40] further developed the idea of confinement regime and studied the effects of the coating used for confinement. The investigations of confined interaction mode by Clauer et al. [48] and Sano et al. [50] indicated improvement in the pressure pulse magnitude by a factor of 5 (for the peak pressure level) and in the pressure pulse duration by a factor of 3 compared to a direct ablation mode.

Hong et al. [51] also investigated the same problem by researching five different kinds of confinement overlays. The limitations of confinement regime were observed in the form of dielectric breakdown phenomena by Foret et al. [43, 49]. The breakdown seems to be due to internal breakdown of the transparent material such that the energy is absorbed primarily inside the transparent material before reaching the black paint - target interface. Thus dielectric breakdown of the confining medium limits the maximum peak pressure obtained by increasing laser energy density. Development in the field of confinement regime, along with inventions in laser technology [23, 24], helped in generating an increased pressure pulse. The laser systems that meet the process requirements are not readily available in the market, but they can be custom built. Further developments in the area of laser systems could reduce the setup cost for the LP processing facility.

The second challenge LP faces is the development of a comprehensive understanding of the process. The knowledge required is described in three aspects: pressure pulse generation, shock wave propagation in materials, and numerical simulation of the process. Within pressure generation, Fabbro et al. [53] described the confined ablation mode with a three-step process. Using this model and considering the plasma to be a perfect gas, the scaling law of the pressure generation (P) can be estimated by the following relationship:

$$P = 0.01\sqrt{\frac{\alpha}{\alpha+3}}\sqrt{Z}\sqrt{I_0} \tag{2.1}$$

where I_0 is the incident laser power density in ($Giga\ Watt/cm^2$), P is the pressure in (GPa), Z is the reduced shock impedance between the target and the confining medium in *ohm*, and α is the efficiency of the interaction. The values of α range from 0.1 to 0.2. More recently, Wu and Shin [54, 55] developed a mathematical model to predict pressure pulse properties (magnitude, duration, and shape).

For shock wave propagation in materials, Love [56] discussed the historical developments in the field of stress propagation in elastic solids. The propagation theory of shock and plastic waves in material are found in Kolsky [25]. The experimental data [9, 10] available in the literature for the material under investigation is up to $10^3/s$ strain-rate, whereas during the LP process, strain-rate goes up to $10^6/s$. Further advances in material data creation will assist modeling and simulation activity.

The goal of performing LP is to improve the material properties, such as fatigue and fretting strength. Therefore, a formulation is needed that can evaluate the influence of LP parameters in terms of resulting material properties. This evaluation can be performed in two steps. In the first step, the residual stress field is determined from the LP parameters. In the second step, material properties are assessed from the obtained residual stress field. This evaluation is the third challenge.

In the literature, the analysis and simulations are limited to the first part of the process. In order to achieve an effective residual stress field, an appropri-

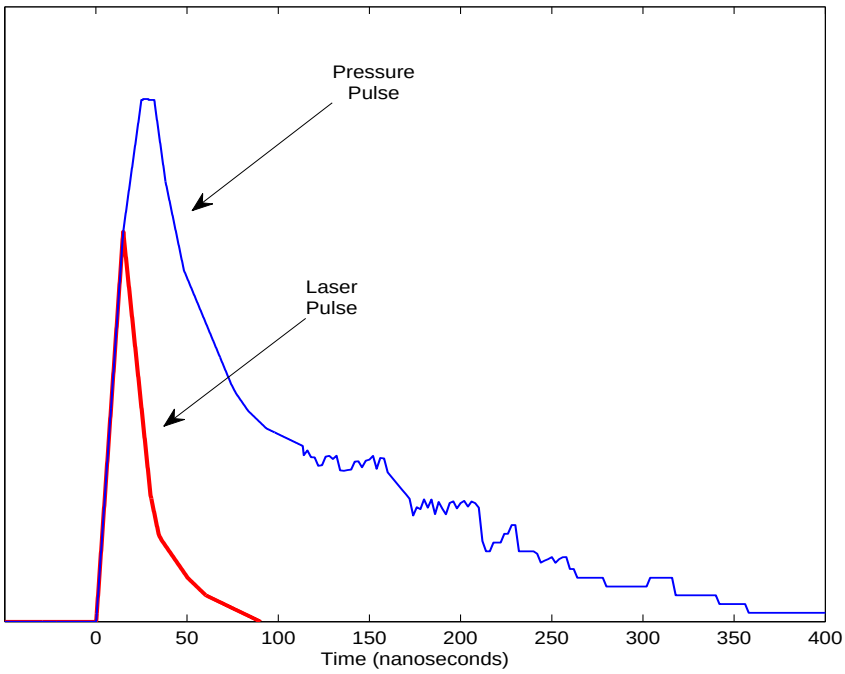

Figure 2.1: Laser pulse and resulting pressure pulse on a target (Peyre et. al. 1996)

ate selection of the process parameters is required. To select a set of optimal parameters, an accurate residual stress prediction methodology is essential. Clauer et al. [1,57], Peyre et al. [6,7], and Fabbro et al. [53] performed numerous experiments to determine residual stress fields for different LP parameters and materials, and showed the advantages of LP in improving the fatigue life. In his research, Peyre et. al. obtained a pressure pulse shape shown in Figure 2.1. Peyre et al. also performed experiments for repeated shots, for comparing residual stress field induced by shot-peening and LP, and finally for comparing fatigue life improvements by shot-peening and LP. The results showed that fatigue life improvement through laser peening is higher as compare to shot peening. Clauer et al. [1] obtained the pressure pulse properties by placing

pressure gauges behind the surface of a thin specimen. Peyre et al. [58, 59] and Ballard [27] obtained the pressure pulse properties from the VISAR (velocity interferometer system for any reflector) pressure determination system.

Experiments alone are not sufficient to demonstrate, expand, and advance the needs of the industry because LP experiments are complicated, potentially tedious, and expensive. The experimental procedure becomes more difficult because of the use of destructive stress measurement techniques such as X-ray diffraction. These reasons provide a motivation to develop analytical and simulation capabilities of the process. Clauer et al. [57] also noted that having a comprehensive model of the process would save significant time and cost when developing new applications. A model could provide guidance and what-if studies in modification and further development of the process. In addition, a model would be invaluable in enabling close process control in production use of laser peening. The ideal scenario would be to have a system that needs a geometric model, material properties, and laser system configuration and provides the engineer with optimal process parameters to achieve the desired residual stress field.

In modeling the LP process, the prediction of the resultant residual stress field is similar to the analysis of shock waves in materials. An analytical model of LP was first developed by Ballard et al. [28]. This was a one-dimensional model which calculated plastic deformation and residual stress levels as a function of impact pressure. A second analytical model was developed by Forget

et. al. [43, 49], which focused on the surface effects induced by shock waves. This model applies to circular impacts where shear waves create interference phenomena. These models were further investigated by Peyre et al. [6] and Fabbro et al. [53]. Peyre at al. proposed a relation between the peak pressure pulse magnitude and laser power density (I_0). Fabbro et al. [53] discussed the effects of laser intensity, target materials properties, laser pulse duration, and laser wavelength in the confinement regime.

These analytical efforts are based on elastic-perfectly plastic material model assuming uniaxial strain conditions. This assumption is fairly accurate for the initial shock wave response. However, under many conditions, this assumption may not hold true because of the presence of non-uniaxial strain affecting the resultant residual stress field. These analytical models are important steps in the development of the overall LP process, however not sufficient to provide the understanding of the process and practical applications.

To overcome the short comings of analytical modeling, multiple efforts were involved in developing FE simulation for the process. After extensive experiments, Nam [9] and Noll [10] developed their own FE code for the LP simulations, which they successfully implemented for a two-dimensional process. Braisted and Brockman [8] performed FE analysis of one-sided and two-sided LP for an axi-symmetric 2-D case using ABAQUS for a single LP treatment. Ding and Ye [11, 60] made initial attempts in the 3-Dimensional simulation; however, they performed only single and multiple treatments of LP at the same

location on simple geometries.

In the process of developing an appropriate simulation methodology, various researchers have used different parameters depending upon the experimental setup at hand. The key differences in these simulation models are the pressure pulse shape and the material model. Ding and Ye [11, 60] used a perfectly elasto-plastic material model using dynamic yield strength (HEL). Zhang et al. [61] investigated the simulation for small impacts with the Steinberg model, taking pressure effect into account for the material model. However Peyre et al. [58, 59] found constant shock yield strength HEL at different LP pressures. As a result, they used the Johnson-Cook model with isotropic hardening which is a strain, strain-rate, and temperature dependent model. In this research, they also presented a limited investigation of the influence of process parameters such as pressure pulse amplitude and duration, laser spot size, and sacrificial overlay. Recently, Wu and Shin [54, 55] developed a model, this includes analytical modeling of the pressure pulse from a laser beam, and limited FE simulations for residual stress prediction.

The numerical work discussed so far concentrated on developing a methodology for FE simulation of the process for a limited number of the LP parameters and simple geometries. However, to determine the usefulness of the generated residual stress field, a numerical process is needed that can assess material properties with or without the presence of residual stresses. The development of this simulation research can relate the process parameters to the

fatigue life. Therefore, it is necessary to determine the improvements in the fatigue life from a set of LP parameters.

2.3 Motivation

In the past, researchers have experimentally investigated the effects of LP parameters on fatigue [1–4, 6, 7] and performed a limited number of simulations on simple geometries [8–10, 54, 55, 59, 60]. However, experimentally monitoring the dynamic, intricate relationship of peened material is challenging. With an increasing number of applications [62, 63] to complex geometries in the nuclear industry, to aircraft turbine blades, and to medical implants, these limited experimental and simulations capabilities are not sufficient for effective LP process design. A comprehensive procedure is required that can perform simulations of multiple treatments of LP at the same location and sequential LP at multiple locations, different overlapping configurations of LP locations, and application on complex geometries. With increased computer speed as well as increased sophistication in non-linear finite element analysis (FEA) softwares, it is now possible to develop a model-based design optimization approach for an effective LP application.

For a typical job, the component is peened using a few (usually 4) parameter settings. These parameter settings for the experiments are selected based on experience. After peening, all the components are subject to service loads to which components are subject to during their intended application. Based

on the improvement achieved in different components, the actual process parameters are selected for the job. Depending upon the resources available, the above process can be repeated after refining the parameters.

For the LP industry to move forward with applications, it is necessary to take the simulation to the next level from simple simulation case studies. There are several parameters that demand exploration of the design space to optimize the residual stress field. For example, the spot size, spot shape, pulse duration, pulse shape, pulse intensity, number of treatments, sequence of locations, amount of overlap, and overall LP location layout can each make a significant difference in component life. Some of these variables are discrete and others are continuous, creating a mixed variable problem for optimization. Along with achieving the desired residual stress field, reduction in unfavorable tensile region (beneath compressive region) is also a goal. Although it is not possible to eliminate the entire tensile region, it can be constrained to be less troubling. Solving a practical mixed design variable optimization problem will be a challenge. The problem formulation is complicated by the time-dependent nature of plastic deformation during the LP process. In addition, the computational effort needed with LP simulations is significant because of the elastic and plastic analysis involved with small time increments. Therefore, an efficient simulation-based methodology is needed to effectively design the LP process. Once the methodology is fully developed, it can be used to optimize complicated applications for direct cost savings.

2.4 Chapter Summary

This chapter starts with reviews of the initial inventions of a high-energy laser to generate shock waves and proceeds to the early developments of shock wave applications in modifying material properties. This is followed by various experimental, analytical, and simulation research done so far. The chapter concludes by presenting a case for effective modeling procedure and challenges ahead in the process. Overall, this chapter provides information on the current status of research and future research goals.

Chapter 3

Finite Element Simulation

Utilization of the promising surface enhancement technology will be difficult with only the knowledge gained through experiments. An increasing number of applications as well as a quest to understand the process, demand a computational exploration of the process. The physical and historical information from Chapters 1 and 2 will help in developing a well-organized simulation methodology.

Before beginning the simulation process, it is vital to research the different parameters required for FE simulation. Apart from the simulation procedure, there are four major modeling parameters. These are the laser spot size and shape, pressure pulse shape and duration, geometric model and meshing, and material model. These parameters are determined based on published experimental and simulation results. This chapter is divided into three major sections. In the first section, a brief description of the simulation parameters and criteria for determining them are presented. The second section provides an

explanation of the simulation procedure used. In the third section, the simulation results of single treatment and multiple treatments of LP at the same location are compared with published experimental results. Once the simulation process is validated with published experimental results, geometric shapes such as a rectangular box are analyzed for sequential LP at multiple locations. Simulation results for two configurations (0% and 50% overlap) of LP at multiple locations are compared with each other.

This is followed by a development of a cylindrical model, parametric plate, and rectangular bending coupon models. The cylindrical model is employed to study the effect of peening sequence. This is also used to investigate effects of a peening shot on near-by, previously peened area. The parametric plate is employed to optimally design a residual stress field for a flat surface. The rectangular coupon model can be used not only for peening simulations, but also to perform fatigue life calculations.

3.1 Simulation Parameters

There are four major modeling parameters in LP FE analysis. These are the laser spot shape and size, the pressure pulse shape and duration, geometric modeling and meshing, and the material model. Apart from the mesh convergence study, these parameters are selected-based on the literature. Details of these parameters are discussed in the following sections.

3.1.1 Laser Spot Shape & Size

Laser spot shape and size are vital simulation parameters. These shapes affect the magnitude and depth of residual stress and can determine the total cost. Two commonly used spot shapes are circular and rectangular. Other shapes, such as elliptical (and its variations) and rectangular can be generated from circular and square laser system by changing the striking angle of laser beam. The accurate effects of spot shape changes are not known and further explorations of the parameter are needed. As far as the size of the spot is concerned, the shock wave attenuation rate for small diameter (0.5-1 mm) spots is higher compared to large diameter (4-5 mm) spots. This is due to two-dimensional attenuation of the shock wave in the case of small impacts that reduce the depth of the plastically affected region and of the compressive residual stress field.

The selection of the parameter is dependent on the laser generation mechanism, material behavior, component geometry, and job requirements. Although it is possible to change the spot shape and size during the process, one size and shape is used for the entire component, due to the effort and time involved in changing these parameters. At the same time further numerical exploration of various shapes is necessary to estimate their benefits before they can be used in practical applications.

3.1.2 Pressure Pulse Magnitude and Shape

Residual stress magnitude and depth are the most sensitive to pressure pulse magnitude and shape parameters. The magnitude of the pressure pulse can be controlled by the intensity of the laser beam. The relation between laser intensity and the peak pressure magnitude in confined ablation mode, as estimated by Fabbro et al. [53] and Peyre et al. [6, 58] with certain assumptions, is given in Equation 2.1. The pressure pulse intensity, shape, and duration depend upon the properties of the laser beam. In the past, experiments have been performed to determine laser beam and pressure pulse properties. Figure 2.1 shows typical shapes of the laser beam pulse and pressure pulse. Depending upon various parameters, the laser beam midspan varies from 5-30 nanoseconds (ns), and the pressure pulse midspan is approximately three times that of the laser beam midspan.

The temporal distribution of the pressure pulse on the surface of the target material can be experimentally measured by multiple methods. Clauer et al. [1] obtained the pressure pulse properties by placing pressure gauges behind the surface of a thin specimen. Peyre et al. [58, 59] and Ballard [27] obtained the pressure pulse properties from the VISAR pressure determination system. VISAR developed by Barker and Hollanbach [64] is an optical-based system that utilizes Doppler interferometry technique to measure the time-history of the motion of a surface. The laser light is focused to a point on a target of interest and the reflected light is collected, routed through an unequal leg in-

terferometer, and converted to electronic information. This information is then analyzed for the amount of Doppler shift during a given time [65]. VISAR can be applied to a wide range of experimental conditions and provides accurate measurement with 1 to 2 ns time resolution.

Recently, Wu and Shin [54, 55] developed an analytical relation between the laser parameters and the LP pressure pulse. Ding and Ye [60] assume that shape of the pressure pulse is like a Gaussian distribution and approximate it using a triangular pressure pulse. During various experiments, it was observed that a steep rise in pressure tends to generate a better residual stress field in terms of magnitude and depth as compared to a Gaussian pulse. Nam [9] and Noll [10] use a shape as shown in Figure 3.1. The figure shows the ratio of pressure at time *t* to peak pressure of the pulse. This pressure pulse is used for experimental validation purpose. The pressure pulse used in this research for various parametric studies and optimization is little different than this shape. Overall pressure pulse features are kept similar. But minor modifications are made after investigating the pressure pulse shapes available in the literature. The difference between the selected shape and this shape is the the selected shape is little smoother profile than this pulse.

3.1.3 Geometric Modeling and Meshing

Normally, the LP-affected zone is small in size compared to the component size. At the same time, LP is a high speed dynamic process, so a fine mesh

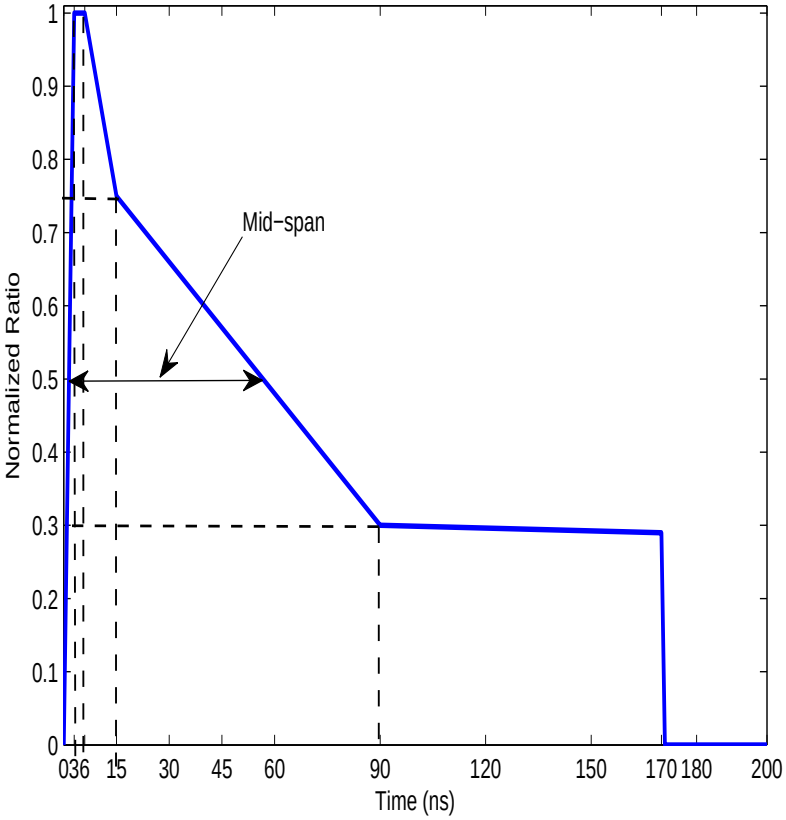

Figure 3.1: Temporal loading profile of pressure pulse (Nam, 2002)

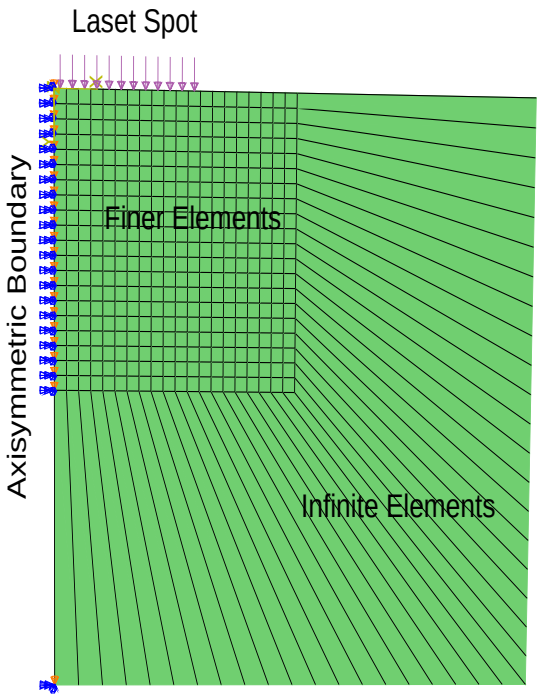

Figure 3.2: Schematic of 2-D axi-symmetric FE model

is required to model stress waves and the interactions between them. A small area of the component that is affected by LP, called the control volume, is modeled using finer elements, and the area surrounding this control volume is modeled using infinite elements. Infinite elements are normally used to define unbounded domain and to provide a model with a 'quiet' boundary. Infinite elements are used in a model in which the region of interest is small in size compared to its surroundings, such as in LP modeling. Figures 3.2 and 3.3 show a two- and three-dimensional representative models of a component. In both cases, the laser spot is a circle of 5 mm in diameter. The experimental results [9] show spatial variation of the pressure across a peening spot. To incorporate spatial variation, as shown in Figure 3.4, the spot is divided into

Table 3.1: Basic material data for Ti-6Al-4V ((Nam, 2002))

Material properties, units	Value
Young's modulus, E [GPa]	113.8
Poisson's ratio, ν	0.342
Density, ρ $[kg/m^3]$	4500
Initial yield stress, Y_0 [MPa]	924
Hugoniot Elastic Limit [MPa]	2800

five sections. The first section is a small circle, (blue in Figure 3.4) from which the remaining sections or bands (yellow, light green, red, and brown), radiate outward in concentric circles. The center most region has minimum pressure (0.8 time the peak pressure) and the outer most has maximum pressure (1.0 time of the peak pressure).

3.1.4 Material Modeling

LP generates strain-rates exceeding 10^6 s^{-1} within the target material. The material model plays a crucial role in accurately simulating a process with such a high strain-rate. In the literature, researchers [11, 58, 59, 61] have used many material models. In this research, two material models were explored for use in LP simulation. The first model uses perfectly elastic-plastic material [11] properties. In this model, Young's modulus and dynamic yield strength are used to define material properties. The dynamic yield strength depends upon the Hugoniot Elastic Limit of the material, and is calculated using Equation 1.1. The material properties of Ti-6Al-4V used for all simulations are shown in Table 3.1 [10]. In the second model, to model the stress-strain dependence at

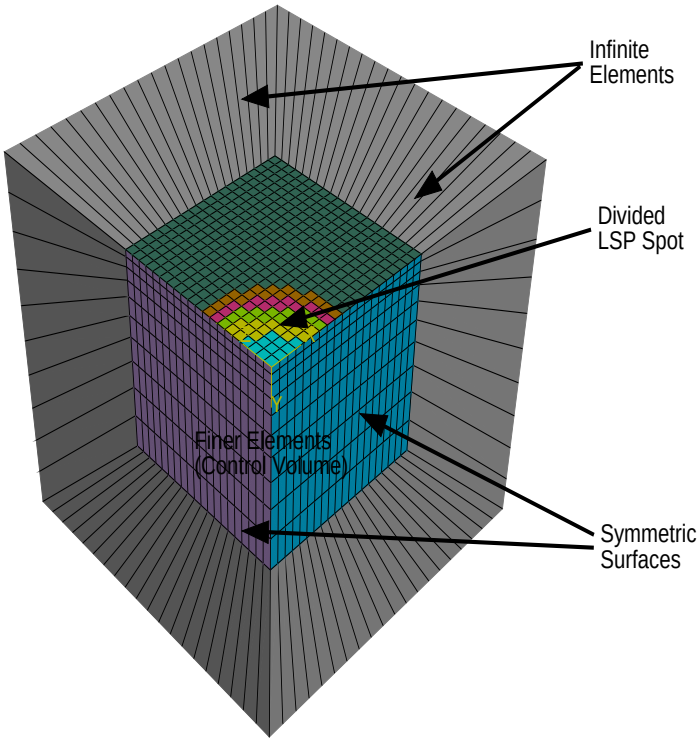

Figure 3.3: Schematic FEA model of a quarter section

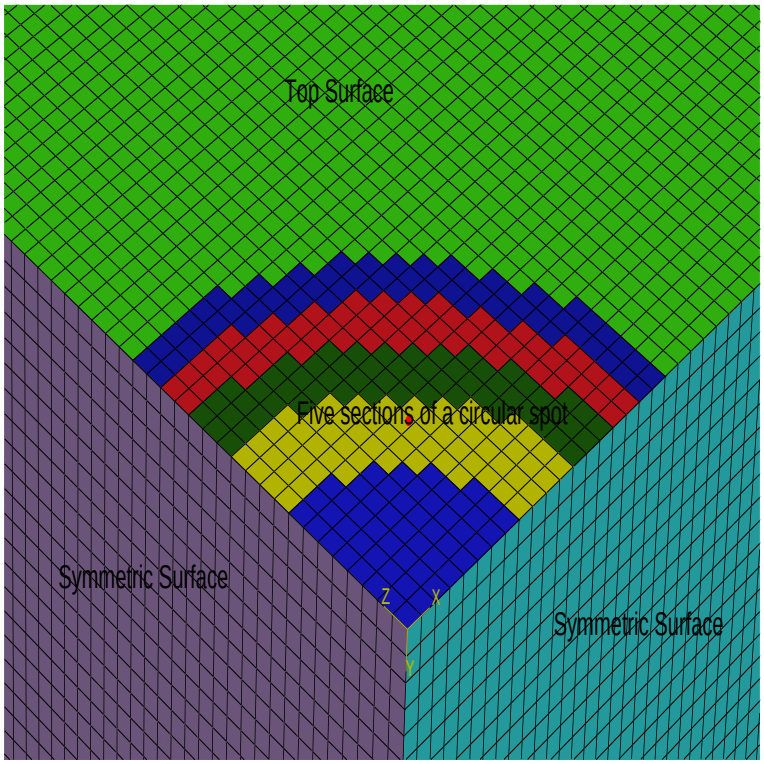

Figure 3.4: Schematic of discretized spot for spatial pressure variation

Table 3.2: Parameters for Johnson-Cook material model of Ti-6Al-4V (Lesuer, 2000)

	A (MPa)	B (MPa)	n	C	m
Ti-6Al-4V	1098	1092	0.93	0.014	1.1

high strain rates, the Johnson-Cook model [59, 66–68] is used. In the Johnson-Cook model, σ_{eq} is expressed as

$$\sigma_{eq} = (A + B\varepsilon_{eq}^{n}) \left[1 + C.Ln\left(\frac{\dot{\varepsilon}}{\dot{\varepsilon}_0}\right)\right].[1 - T^{*m}] \tag{3.1}$$

where σ_{eq} is the effective stress, A, B, C and m are material constants, n is the work hardening exponent, $\frac{\dot{\varepsilon}}{\dot{\varepsilon}_0}$ is the normalized effective plastic strain rate, and the quantity T^* is defined as

$$T^* = \left(\frac{T - T_0}{T_{melt} - T_0}\right) \tag{3.2}$$

where T_{melt} is the melting temperature. The strength of the material is a function of strain, strain-rate, and temperature. The values of A, B, C, n, and m are determined from an empirical fit of experimental flow-stress data. The opaque overlay prevents the material from generating high temperatures during the peening process. Due to this coating, the effect of temperature during peening is limited. Therefore, the effects of temperature are not considered in the material model.

3.2 Simulation Procedure

Because of the complexity of elastic and plastic deformation and shock wave propagation, it is necessary to employ an accurate procedure with manageable computational requirements. As discussed in Chapter 1, very high magnitude pressure pulse of the LP process lasts for very small period of time. However, it takes a much longer time for the material reach an equilibrium. The time scale of pressure duration is in nano second (ns). The time scale to reach equilibrium is in milliseconds (ms). In cases of shock loading such as in LP, equilibrium can not be achieved quickly because of the propagation and interaction of stress waves. The residual stresses are caused by the plastic deformation, and the plastic process last for a very short time. It is essential to obtain the equilibrium state for accurate results.

An appropriate simulation procedure is needed. The explicit algorithm is suitable for high speed process [69] such as initial phase of the LP process, but if this algorithm is used for the entire process till equilibrium, it is not computationally efficient. The reason for the inefficiency is that this algorithm is not designed for use in slow processes such as later part of the LP process and it also integrates over time in small time steps for algorithm stability. The implicit algorithm [69] of FE analysis is suitable for the later part, but not the initial part, of the process. Therefore, a simulation procedure is used that takes advantage of both processes and obtains the equilibrium state within a

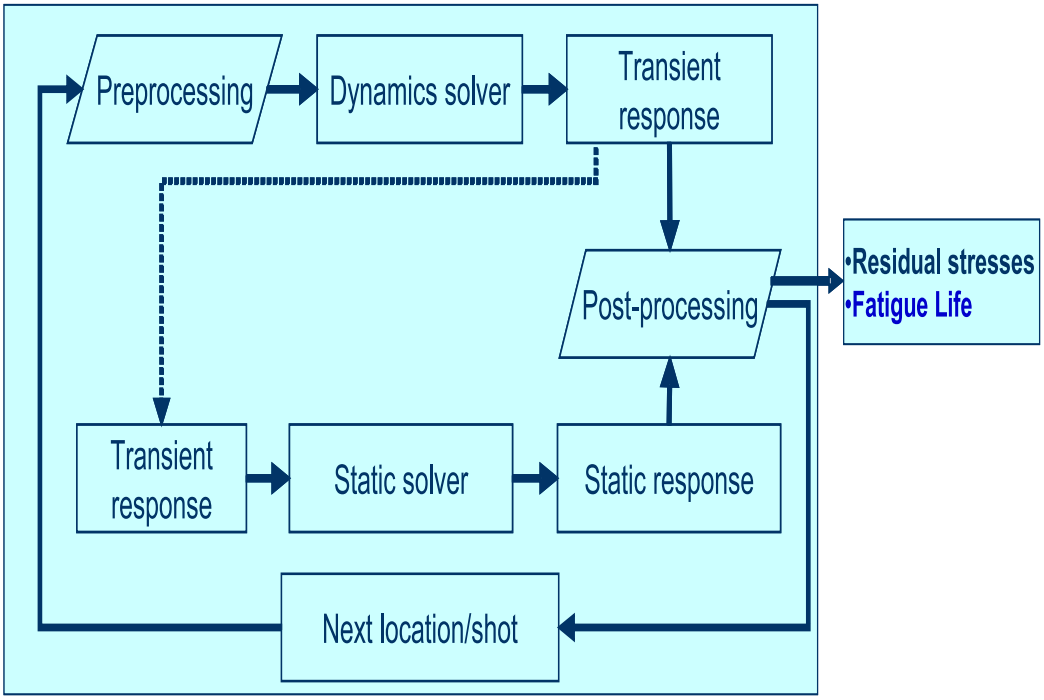

Figure 3.5: Flow-chart of simulation process

manageable computational time.

FE simulation of the LP process is divided into two phases [8]. The flow chart of the process is shown in Figure 3.5. The first is modeling the initial high speed transient high pressure loading in ABAQUS/ Explicit, which is specifically designed for such processes. The second phase, which is a comparatively slower physical process, is to determine the final equilibrium residual stress field. This phase of the analysis is performed in ABAQUS/Standard (implicit algorithm).

3.2.1 Explicit and Implicit Algorithms

To analyze the dynamic response of a material, caused by high speed and high intensity laser shock, the explicit FE method is used. The governing equations for general explicit algorithms can be derived by requiring the work of external forces to be absorbed by the work of internal and inertia forces for any small, kinematically admissible motion, which satisfies both compatibility and essential boundary conditions [70, 71]:

$$\int_{\Omega} \rho \ddot{u}_i \delta u_i d\Omega + \int_{\Omega} \upsilon \rho \dot{u}_i \delta u_i d\Omega = \int_{\Omega} f_i \delta u_i d\Omega + \int_{\Gamma} T_{\Gamma} \delta u_i d\Gamma - \int_{\Omega} \sigma_{ij} \delta D_{ij} d\Omega \tag{3.3}$$

where ρ is the mass density, $\ddot{u}$ and $\dot{u}$ are the nodal acceleration and velocity, respectively, υ is the damping coefficient, δu is the virtual displacement, f_i is the body force density, T_{Γ} is the boundary force applied on the boundary Γ, σ_{ij} is the Cauchy stress tensors, and $D_{ij} = \frac{1}{2}(\delta u_{i,j} + \delta u_{j,i})$ is the deformation-rate tensor. In Eq. 3.3, the five terms represent inertia, damping, body forces, boundary forces, and strain energy of the system under consideration, respectively. The standard FE procedure can be used to obtain a discretized equation:

$$[\mathbf{M}]\{\ddot{\mathbf{U}}\} + [\mathbf{C}]\{\dot{\mathbf{U}}\} + [\mathbf{K}]\{\mathbf{U}\} = \{\mathbf{F}^{ext}\} \tag{3.4}$$

where $[\mathbf{M}]$ is the diagonal mass matrix, $\{\ddot{\mathbf{U}}\}$ is the nodal acceleration vector, $\{\dot{\mathbf{U}}\}$ is the velocity vector, $[\mathbf{C}]$ is the diagonal damping matrix, $\{\mathbf{F}^{int}\}$ is the

internal element force vector, and $\{\mathbf{F}^{ext}\}$ is the external and body force vectors. In the integration methods, response history is calculated using step-by-step integration in time. The response is evaluated at time instants Δt, $2\Delta t$, ..., $n\Delta t$ and so on. At the n^{th} time step, the equation of motion is [71]

$$[\mathbf{M}]\{\ddot{\mathbf{U}}\}_n + [\mathbf{C}]\{\dot{\mathbf{U}}\}_n + [\mathbf{K}]\{\mathbf{U}\}_n = \{\mathbf{F}^{ext}\}_n \tag{3.5}$$

Discretization in time is achieved by finite difference approximation of time derivatives. There are many ways to perform the discretization and solve the equation. In this discussion, $[\mathbf{M}]$ is assumed positive definite and $[\mathbf{K}]$ is positive semidefinite. Structure is allowed to have rigid-body motion as part of its response.

In the time integration conditions at time step $(t+1)$ are calculated from the equation of motion, a difference expression, and known conditions at one or more preceding time steps. Algorithms can be classified as *explicit* and *implicit* depending upon the information used in calculating conditions at $(t+1)$. An explicit algorithm uses an expression of the general form [71]

$$\{\mathbf{U}\}_{n+1} = f(\{\mathbf{U}\}_n, \{\dot{\mathbf{U}}\}_n, \{\ddot{\mathbf{U}}\}_n, \{\mathbf{U}\}_{n-1}, \ldots) \tag{3.6}$$

that contains only historical information on its right hand side. This equation is combined with the governing Eq. 3.5 at step n to solve the problem. An

implicit algorithm uses the following general form

$$\{\mathbf{U}\}_{n+1} = f(\{\dot{\mathbf{U}}\}_{n+1}, \{\ddot{\mathbf{U}}\}_{n+1}, \{\mathbf{U}\}_n, \{\dot{\mathbf{U}}\}_n, \{\ddot{\mathbf{U}}\}_n, \{\mathbf{U}\}_{n-1}, \ldots) \tag{3.7}$$

that is combined with the governing Eq. 3.5 at step $(n+1)$ to solve the problem. In the explicit algorithm, only the historical information is used to calculate dynamic quantities at $(t+\Delta t)$. The central difference method is used in the explicit algorithm. By manipulating the Taylor series expansion of $\{\dot{\mathbf{U}}\}_{n+1}$ and $\{\dot{\mathbf{U}}\}_{n-1}$ about time $n\Delta t$:

$$\{\dot{\mathbf{U}}\}_n = \frac{1}{2\Delta t}(\{\mathbf{U}\}_{n+1} - \{\mathbf{U}\}_{n-1}) \tag{3.8}$$

It can be written as:

$$\{\mathbf{U}\}_{n+1} = \{\mathbf{U}\}_{n-1} + 2\Delta t\{\dot{\mathbf{U}}\}_n \tag{3.9}$$

The $\{\mathbf{U}\}_{n+1}$ can be used to calculate $\{\ddot{\mathbf{U}}\}_n$:

$$\{\ddot{\mathbf{U}}_n\} = \frac{1}{\Delta t^2}(\{\mathbf{U}\}_{n+1} - 2\{\mathbf{U}\}_n + \{\mathbf{U}\}_{n-1}) \tag{3.10}$$

The integration rule in the explicit algorithm is simple, this is a reason behind the computational efficiency of the explicit dynamics procedure. The equation derived from the central difference scheme used in the algorithm is conditionally stable [71]. As a result stable time step is an important factor and the explicit FEA integrates through time by using many small time increments.

The stability limit for the time step operator depends upon the highest natural frequency. Since it is hard to find the highest natural frequency, a conservative estimate of the stable time increment is given in Equation 3.11 [69, 71] in terms of minimum element size (L_e) and the current effective dilatational wave speed of the material (C_d). The point to note is that if the minimum element size is reduced, then Δt_{stable} decreases while the time required to perform the integration, and ultimately analysis time, increases.

$$\Delta t_{stable} = min(L_e/C_d) \tag{3.11}$$

Due to this limit (3.11), a very small time step for integration is used for accurate results, which leads to large computational cost. However, the implicit algorithm removes this upper bound on the time step for integration by solving for the dynamic quantities at $(t+\Delta t)$ based not only on values at t, but also on these same quantities at $(t+\Delta t)$. Based on the special case of Newmark method [72] the relations for implicit algorithm as give by [71] are

$$\{\dot{\mathbf{U}}\}_{n+1} = \{\dot{\mathbf{U}}\}_n + \Delta t\left(\gamma\{\ddot{\mathbf{U}}\}_{n+1} + (1-\gamma)\{\ddot{\mathbf{U}}\}_n\right) \tag{3.12}$$

$$\{\mathbf{U}\}_{n+1} = \{\mathbf{U}\}_n + \Delta t\{\dot{\mathbf{U}}\}_n + \frac{1}{2}\Delta t^2\left[2\beta\{\ddot{\mathbf{U}}\}_{n+1} + (1-2\beta)\{\ddot{\mathbf{U}}\}_n\right] \tag{3.13}$$

where γ and β control characteristics of the algorithm such as accuracy, numerical stability, and the amount of algorithm damping. Respectively, the average acceleration and linear acceleration methods [71] are given by γ=$\frac{1}{2}$, β = $\frac{1}{4}$ and

by $\gamma=\frac{1}{2}$, $\beta = \frac{1}{6}$. By solving Eqs. 3.12 and 3.13 for $\{\ddot{\mathbf{U}}_{n+1}\}$, then further substitution [71] can provide the implicit solution.

It is difficult to solve implicit equation in the algorithms, but the time step can be two orders of magnitude larger than the explicit algorithm. Thus, the relative computational cost of the two algorithms depends on the stability limit of the explicit scheme, the ease with which the nonlinear equations can be solved for the implicit operator, the relative size of time increments that can provide acceptable accuracy with the implicit scheme compared to the stability limit of the explicit scheme, and the size of the model. The equilibrium equation for the implicit algorithm can be obtained from Refs. [69, 71]. A brief description is provided in this section. The description is for academic purpose only. These algorithms are in-built in the FEA software. The user only need to selected the appropriate option to use implicit or explicit algorithm.

Because of the two steps involved in the simulation procedure, it is necessary for accuracy and efficiency to determine the analysis duration of each step. The simulation duration would be much longer than the pressure pulse duration. Ding and Ye [60] suggested that the solution time should be two orders of magnitude higher (3000) than the pressure pulse duration (30). In this work, a large number of analyses is performed to select the duration, and an analysis time of 2500 to 3000 ns for the first phase and $10-50$ millisecond (ms) for the second phase is used.

3.2.2 Ohio Supercomputing Center for Simulations

Due to the computational cost involved in a LP simulation, most of the finite element simulations are performed on the Glenn cluster at the Ohio Supercomputing Center (OSC). The OSC is located in Columbus, Ohio. The details of the Glenn and other clusters at OSC can be found at the institute website (www.osc.edu). In brief [73], there are more than 7000 nodes, each node with dual or quad core, 2.6 GHz speed, and 8GB or higher (more than 6000 nodes with 8GB, 70 nodes with 16GB, 16 nodes with 32GB, 2 nodes with 64GB, 76 nodes with 218GB, and 10 nodes with 1.8TB RAM) RAM. The total CPU computational time at OSC involves two parts. The first part is the waiting period and the second part is the computation part. The waiting time is a of function many parameters such as load on server, requested CPU time, requested RAM, and cluster maintenance activities. The CPU time mentioned in the dissertation does not include the waiting time.

3.3 Two-Dimensional Simulation

The $2D$ simulation is an efficient way to simulate one shot with the circular spot at the same location because of less computational requirements. Figure 3.2 shows an axisyymmetric FE model of a component. The model consists of a 5×5 (mm^2) rectangular area of finer elements surrounded by 5 mm of infinite elements on each of the two sides. The FE model represents a cylindrical part

of 10 *mm* diameter with a laser spot of 5 *mm* diameter. Based on the mesh convergence a 200×200 mesh is used for the 5 *mm* square. This model contains 40000 finer elements (four-noded CAX4R elements in ABAQUS) and 400 infinite elements (four-noded CINAX4 elements). This model is developed for use in solving the optimization problem of designing a required residual stress field.

3.4 Three-Dimensional Simulation

Using 2*D* FE simulations is a computationally efficient way to predict the residual stress field for one shot of LP at the same location. However, variations such as sequential shots at multiple locations or rectangular or elliptical spot shapes are not possible to simulate in 2*D*. These variations require three-dimensional FE simulation of the process. Figure 3.3 shows a quarter FEA model of a component. The quarter model consists of a 5-*mm* cube of finer elements surrounded by 5 *mm* of infinite elements on each of the three sides. The laser spot is a circle, 5 *mm* in diameter.

3.4.1 Mesh Convergence

To determine a suitable mesh size for the simulation, a mesh size convergence study is performed on a quarter model (Figure 3.3). The mesh convergence study is divided into two parts. In the first part, four uniform meshes are investigated. In the second part, based on the results of the first part, three biased

meshes are investigated. The first part is to determine the converged mesh, and the second part is to bring the computational cost within acceptable limits for the research purpose. In all the models, control volume is modeled using eight-noded C3D8R elements and the surrounding region is modeled using CIN3D8 infinite elements. In mesh convergence, 40, 80, and 160 elements are used to mesh a 5-mm-long side of the control volume. The element size for each mesh is 0.125 *mm*, 0.0625 *mm*, and 0.03125 *mm*, respectively.

The mesh size with 320 elements (0.015625 *mm*) was also attempted. It is infeasible to use this mesh due to the computational space and memory requirements. Deu to this, mesh size with 200 element was attempted. Even this mesh will take approximately 10 days of CPU time. This time does not include waiting time of around 3-20 days. The waiting time is high because of a limited number of high memory nodes at OSC.

A comparison of the residual stress profile from various mesh sizes is shown in Figure 3.6. The results show residual stress magnitude along Y-axis and depth along X-axis. The figure compares the results from uniform and nonuniform mesh models. The residual stress profile can be divided into two regions; 0.0 to 0.2 *mm* and 0.2 *mm* to 5 *mm*. The residual stress profiles between the depth of 0.2 to 5 *mm* are matching with each other for most of the mesh sizes. In fact, all uniform mesh model results are on top of each other. The residual stress profiles between the depth of 0.0 to 0.2 *mm* are different from each other for the considered mesh sizes. The maximum difference between mesh

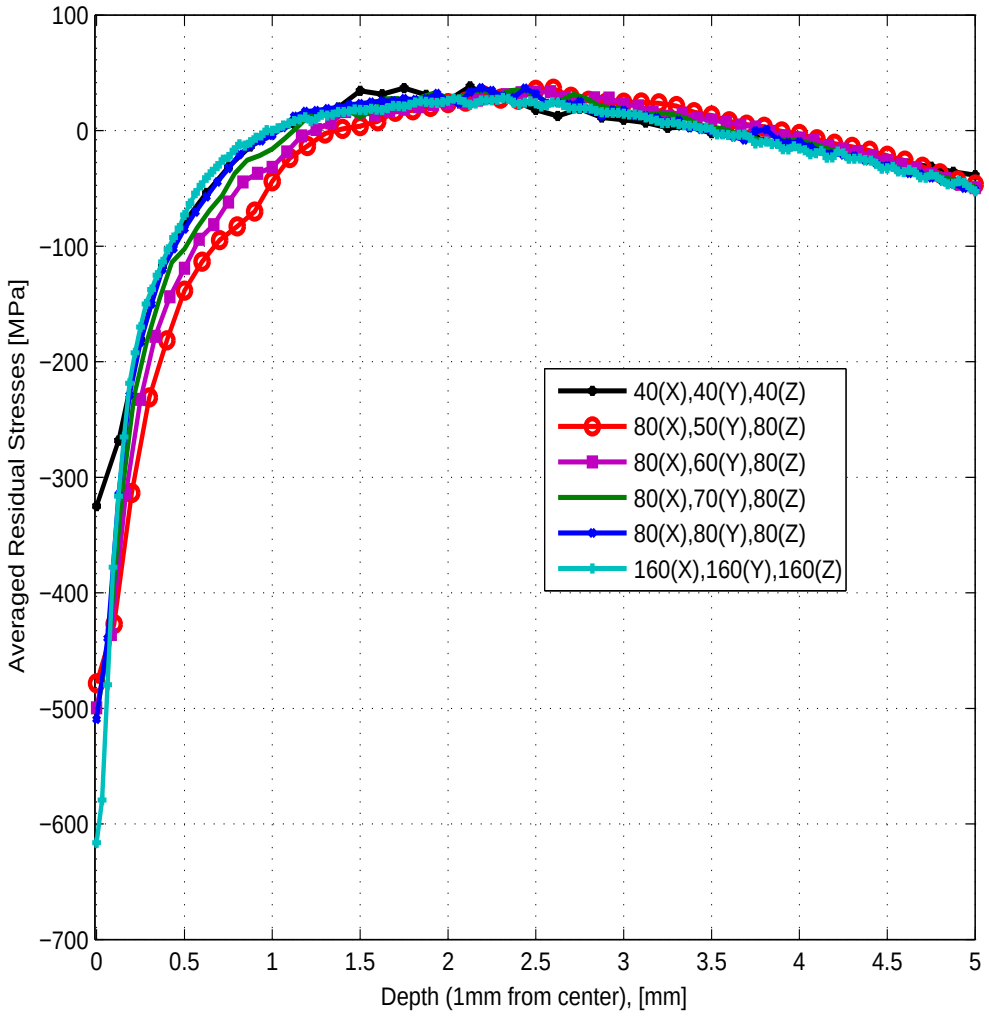

Figure 3.6: Mesh convergence results

sizes 80 ($80 \times 80 \times 80$) and 160 is 16%. This is the maximum difference and is large but it is only in very small region. The results are matching with each other in most of the depth. Therefore, the 160 mesh can be assumed to be a converged mesh, CPU time required for this simulation is prohibitively expensive (7.5 days). The use of this mesh will make it difficult to perform full $3D$ simulations for multiple peening locations.

Based on the time taken by the finest mesh, biased mesh convergence study is also performed. In the quarter symmetric $3D$ models (Figure 3.3), X- and Z-axes are along the peened surface and Y-axis is represent depth of the component (in the direction of the LP pressure). In the biased mesh study, the element size along X- and Z-axes is kept constant. The element size is biased along the Y-axis. In this direction, the finest element is at the top surface. The biased mesh is decided using two parameters: the size of the first element on the surface and the total number of elements. In this study, the size of the top element is fixed at 0.0625 *mm*, which is equivalent to having 80 elements per 5 *mm* along Y-axis. The number of elements used is 50, 60, or 70. The mesh in the other two directions is uniform (80 elements).

The time taken by each of these analyses is shown in Table 3.3. The CPU time shown in the table is in minutes on the Glenn cluster at OSC. This time does not include the waiting time. Typical waiting time for $40 \times 40 \times 40$ and $160 \times 160 \times 160$ meshes is around 15 and 2000 minutes, respectively. This time is not the exact time. The time in minutes is rounded to the nearest 10.

Table 3.3: Mesh convergence study

Number of Elements			Mesh	CPU Time
X-axis	Y-axis	Z-axis	Type	in minutes
40	40	40	Uniform	60
80	50	80	Biased	720
80	60	80	Biased	1,260
80	70	80	Biased	1,680
80	80	80	Uniform	1,950
160	160	160	Uniform	10,800

Table 3.4: Mesh Convergence Study with Respect Compressive Volume

Number of Elements			Compressive
X-axis	Y-axis	Z-axis	Volume (mm^3)
40	40	40	4.17
80	50	80	4.48
80	60	80	4.51
80	70	80	4.53
80	80	80	4.63
160	160	160	4.67

The extensive mesh convergence study provides the following results, indicating that it is possible to achieve convergence in 3D but it is not computationally feasible. Comparison of the results shows that the biased mesh is able to produce similar results without having to use a finer mesh for the entire depth. A biased mesh of $80 \times 60 \times 80$ would be an acceptable mesh for research purposes. The above convergence study is performed on the residual stress profile. In the design optimization of the LP process four performance metrics are used. These metrics are calculated form the residual stress profile. The objective of all optimization formulations is to compressive stress volume.

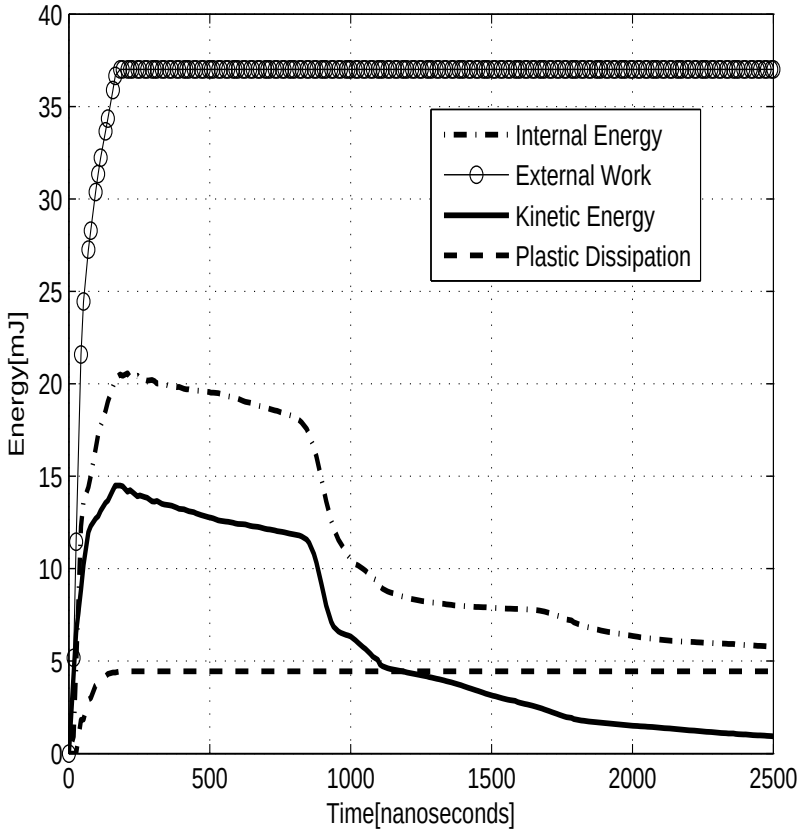

Figure 3.7: History of internal energy, artificial strain energy, kinetic energy, plastic dissipation and external work

A convergence study is also be performed with respect to the compressive volume. The results of the study are shown in table 3.4. The table shows that compressive volume values are comparable to each other. This study shows that the selected biased mesh can be assumed as converged mesh for the research purposes.

3.4.2 Preliminary results

The LP pressure pulse inputs energy into the material, and the energy is divided into different types of energies. Part of the energy is used in plastic

deformation, and part of it is converted into kinetic, internal, and heat energies. Figure 3.7 shows the history of the total energy, the kinetic energy, the internal energy, and the plastic dissipation energy for a 3 GPa peak pressure pulse. The time duration of 2500 ns for dynamic analysis is selected based on the variation in the plastic deformation and the internal and kinetic energies. When these three quantities become approximately stable at 2500 ns, the next step of the analysis begins.

The explicit, implicit, and total analysis times for each model are different. These depend upon the geometry, number of elements, analysis duration, and type of elements. For example, a model with infinite elements requires less time compared to a model without infinite elements. The reason behind this is that infinite elements/region tend to absorb the peening energy and allows the model to reach equilibrium state faster. In the absence of infinite elements the energy reflects back from the geometric boundaries. In such cases, the equilibrium is achieved more slowly. Figure3.7 shows that the plastic deformation lasts for only a small duration when the applied pressure is above the elastic limit. The figure shows that the external work and the plastic dissipation energy change occur for the duration of the pressure pulse, which is 170 ns. After that, the plastic dissipation energy is constant at approximately 4.5 mJ. The kinetic energy increases to 13.5 mJ pressure is applied, then drops to 6.5 mJ at 1000 ns, and goes to almost zero after 1500 ns. There are many activities going on during the initial 1000 ns, and all energies reach an approx-

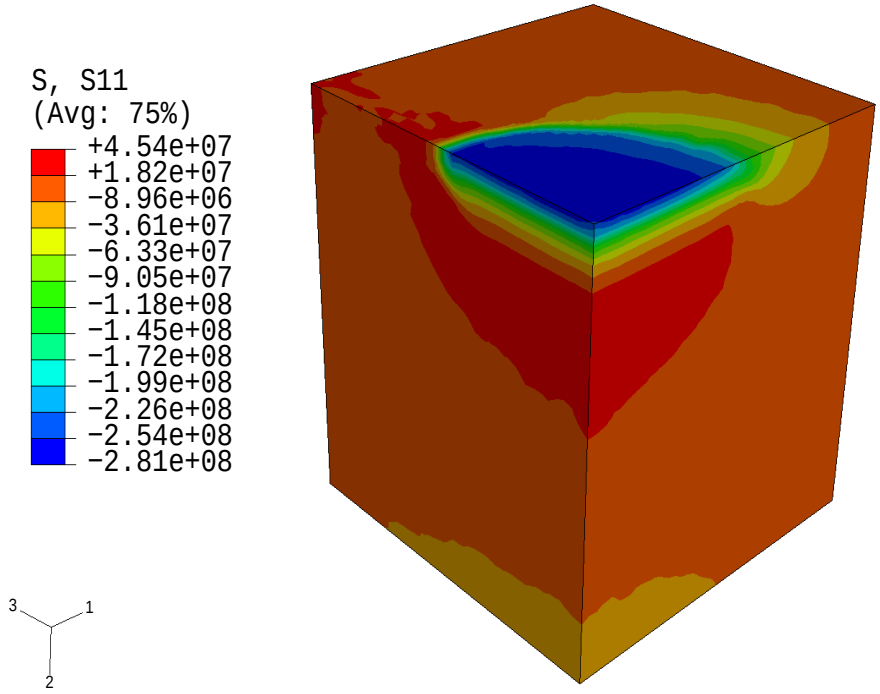

Figure 3.8: Resultant residual stress distribution plot for 3 GPa peak pressure pulse

imately stable level from 1000 ns to 2000 ns. It can be inferred that there is no interaction between various stress waves inside the component after 2500 ns.

Figure 3.8 shows the residual stress distribution of a 3 *GPa* pulse of duration 170 *ns*. The maximum compressive stresses are at the surface. On the surface, the location of the maximum stress is not at the center of the spot. For 3 *GPa* location of maximum compressive stress is 0.05 away from the center. The maximum compressive stress location is not independent of the LP parameters. For example the location changes with the pressure pulse magnitude. For higher pressure magnitudes the location moves away from the center and below the top surface. The volume of the compressive stress is less as compare to the volume of tensile stress. The maximum tensile stress are below

the compressive stress at the center of the model. The depth of the compressive stress is approximately same in the entire spot. The maximum depth of tensile stress is at the center of the spot. This figure shows that LP is able to generate compressive stress in the component, but there are two causes for concern. With the current set of parameters, a part of the component has tensile stresses. Tensile stresses are generated to balance the compressive stress for equilibrium in the absence of external force. These tensile stresses cannot be eliminated; however, these can be constrained in optimization to avoid adverse consequences. Another cause for concern is a small, shallow, reduced compressive or tensile stress region in the center of the laser spot for higher peak pressures; however, it is not representative of most of the laser spot.

3.4.3 Experimental Validation

In this section, finite element results are compared with the experimental results from the literature. Multiple analyses are performed for this purpose. The computed residual stresses are compared with the residual stress field from the available experimental results. Two types of residual stresses are reported in the dissertation: maximum principal and uni-directional stress (σ_{11} or σ_{33}). As in the LP literature, most calculations in the dissertation are use the uni-directional stresses.

Residual Stress Averaging

All the experimental residual stresses reported here are taken from a PhD dissertation by Nam [9] at the Ohio State University. These experimental results are obtained using the X-ray diffraction technique. This is a destructive residual stress measurement technique in which a thin layer of material is removed using electro-polishing. The residual stresses obtained using X-ray diffraction are averaged over a rectangular area. This rectangular area's size and shape are dependent on the size and shape of the X-ray diffraction spot. For a direct comparison between FE simulation results of residual stress distributions, the same averaging should be used. For simulation results, the averaging is done for 1 *mm* square. For a node, residual stress values at all the nodes in 0.5 mm distance in all four direction are added. This value is divided by the total number of nodes. The resulting value is the residual stress value for the selected node. Figure 3.9 can be used to understand the process averaging process. The figure shows a layer of nodes in a model. The red node shown in the figure is selected to show the averaging process. The residual stress values of the nodes in the 1 *mm* square are added. This value is divided by total number of nodes (25 in this figure). The resulting value is the residual stress value at the selected red node. Similar can be used to calculate a averaged residual stress profile for a entire model.

This is necessary to add that the same averaging process is used for all the calculation in this research. This process is independent of the LP parame-

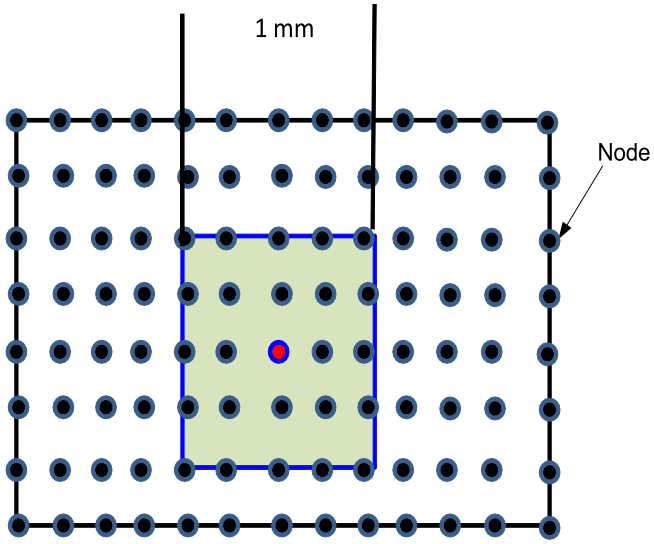

Figure 3.9: Averaging Schematic

ters. If there are high stress concentration location (compressive or tensile), these values will reduce or may even disappear due to averaging. For a research that is interested in the local effects of LP, averaging may not be a good option. Averaging is a necessary for comparison between experimental (with XRD measurements) and simulation results. The same averaging process is used in this research for consistency purposes. Depending upon the research requirements this averaging process can be changed.

Result Comparison

In each case, residual stress, strain, and deformation properties of the control volume are transfered to the next phase, and the infinite element section is

remodeled. The symmetric 3D model is analyzed for 5.5 *GPa* and 8.3 *GPa* pressure pulses. Results obtained for 5.5 *GPa* and 8.3 *GPa* are compared with published experimental [9] results. The comparison of the simulation and ex-

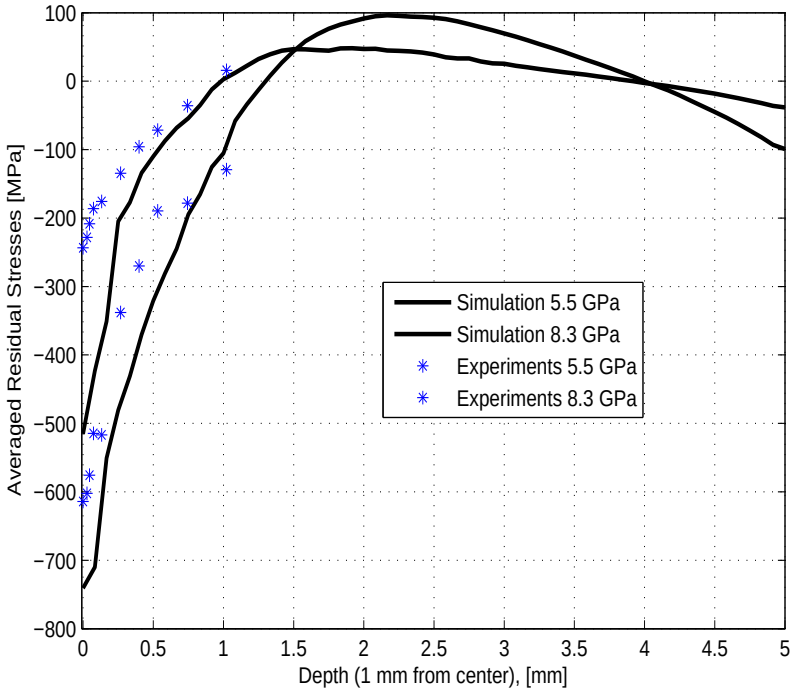

Figure 3.10: Comparison of experimental results with simulation at 1 mm from spot center line

perimental results shows agreement between the two in majority of the component depth. The simulations are able to estimate the depth of compressive stress and major portion of compressive stress magnitude. The simulation estimate of residual stress at the surface show difference in magnitude. The difference in the results can be due to the material model, variation in pressure pulse properties, and uncertainties in the experimental measurements. Although improvement is necessary and possible, it may be difficult to exactly match the experimental results.

3.4.4 Residual Stress Profile

Figure 3.10 compares the experimental and simulation results for the average residual stresses of the two peak pressure pulses, 5.5 *GPa* and 8.3 *GPa*, for one-sided single LP. These comparisons are made along a line offset 1 *mm* from the centerline of the laser spot. Comparisons are made at this location because the highly localized effect of the release waves focuses at the center of the spot, causing reduction in the compressive stress.

3.5 Two Shots Sequence Model

To investigate the effect of sequential peening and overlap, a simple extension of quarter symmetric 3*D* model is developed. As shown in Figure 3.11, this model is half symmetric. The finite element properties and the LP properties for this model are same as that of the quarter symmetric 3*D* model. The simulation of sequential LP at multiple locations is performed for two configurations. In the first configuration, two LP locations that contact each other without overlap are considered. In the second configuration, there is a 50% overlap between the two LP locations. Figure 3.11 shows a schematic of sequential LP at multiple locations with 50% overlap between the two locations. In the figure, the control volume has two overlaping spots and infinite elements all around. In the case of 0% overlap, the control volume dimensions are 5 *mm* $\times$ 5 *mm* $\times$ 15 *mm*, and in the case of 50% overlap, the dimensions are 5 *mm*

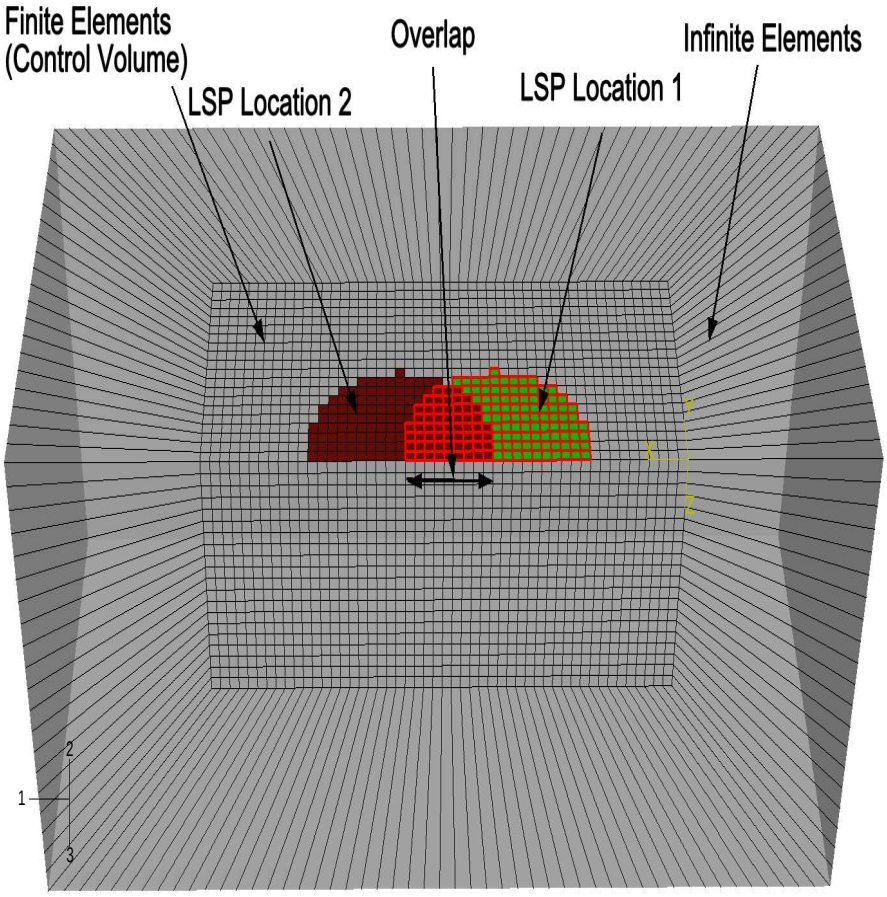

Figure 3.11: Schematic of sequential LP at multiple locations on a FEA model

$\times$ 5 *mm* $\times$ 12.5 *mm*. Different sizes of control volumes are used to minimize computational expenses.

The computational time for analysis is huge. Using a Pentium(R) 4 CPU, 3.40 *GHz* personal computer with 2.00 *GB* of RAM, it takes approximately 48 Hours of CPU time to finish one analysis. Typically, depending upon the size and requirements of a component, it may need from 20 to 100 LP shots. Therefore, the time taken for the above case is an indication that FE simulation for a practical component will be a computational challenge.

3.6 Seven Shots Sequence at Multiple Locations Model

In this section, a cylindrical model is developed that can be employed to investigate seven shot sequence. The model is shown in Figure 3.12. The cylindrical shape is selected to minimize the computational requirements of a seven shot sequence. The cylindrical shape is better suited to the investigation compared to a rectangular component. This model requires a lower number of elements compared to a rectangular model. The control volume of the model has finer mesh. The rest of model has coarser mesh. The model can also be employed to investigate the effect of multiple shots in partial overlapping conditions.

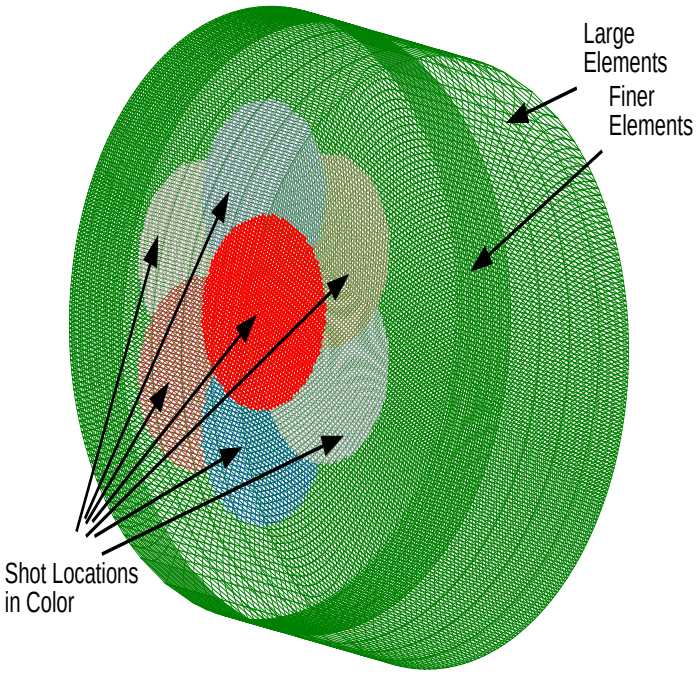

Figure 3.12: Cylindrical model for sequence investigation

3.7 Parametric Plate Model

The parameters of validated symmetric 3*D* simulation methodology are used to develop the parametric plate model. Figure 3.13 shows the FE model of the plate with a control volume size of $10 \times 10 \times 5$ (mm^3). The model is a infinite slab because of the presence of infinite elements. In this dissertation, it is called a parametric plate because it can consider most of the LP parameters. As shown in the figure, infinite elements extend from the plate by 5 *mm* on four sides and on the bottom of the plate. In this model, up to five different locations can be selected for peening. The figure shows four spot locations; a fifth one is located at the center of the plate. These locations are variables to generate the desired overlapping configurations or totally separate spots. Apart from the

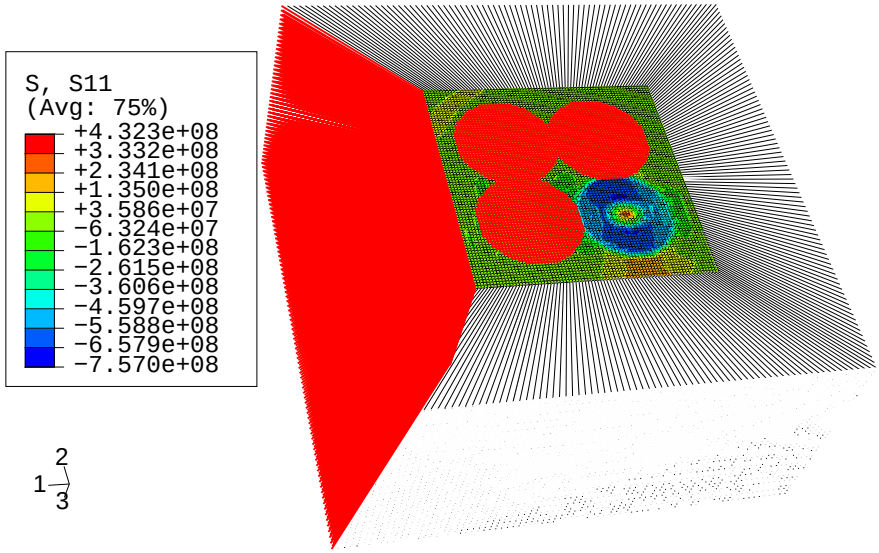

Figure 3.13: FEA model of a plate with five shots

parametric locations (or overlap), the model allows the designer to specify the spot size and shape, pressure pulse magnitudes, shapes and duration, number of shots at the same location, and the sequence of shots. This model provides many advantages, but introduces the issue of computational resources. For the above-mentioned methodology, a five shot simulation (at the same location or different) takes 4 days on the Glenn cluster at OSC. Design optimization is an iterative process and the use of metamodels is advised to avoid prohibitively large computational expense.

3.8 Rectangular Coupon Model

A rectangular coupon is selected for modeling because it can be employed in future work for experimental validation of residual stress profiles and fatigue life estimation. The basic framework, mesh convergence, and material model

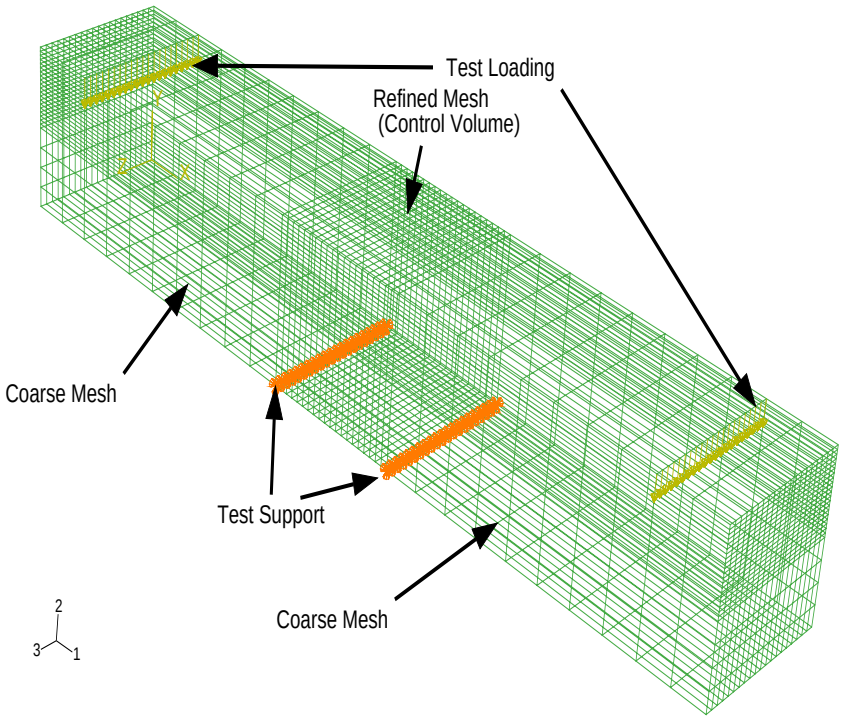

Figure 3.14: FE model of the four point bend specimen

for the coupon are taken from the validated 3D model. The region of interest is called the control region. The controlled region is uses a very fine mesh. The region surrounding the control region is meshed using coarse mesh. These region can be clearly seen in Figure 3.14. The coupon model can be used to perform laser peening simulations to estimate induced residual stresses. The same coupon with residual stresses can be employed to apply fatigue loading. This setup will allow the calculation of the fatigue life of the peened coupon, and the ability to compare it with the fatigue life of the unpeened coupon. For the coupon model, a three shot simulation takes 8 CPU hours on a processor at OSC.

3.9 Chapter Summary

This chapter began with an explanation of the simulation-based methodology. The methodology is adopted to predict residual stresses generated by the LP pressure pulse. Based on the literature, a range of LP parameters is determined and used for simulation. Initially, this methodology is successfully verified by comparing the simulation results with the available experimental results. Then the methodology and model are used to develop models to investigate two overlapping shots, a seven shot sequence, and parametric design optimization of a laser peening process. In summary, this work added to the understanding of the physical process of laser peening and developed a simulation-based methodology, which can be used for analysis of complex geometries representing practical applications. Parametric investigations, residual stress field optimization, and residual stress estimation for fatigue life calculation can be performed by using the simulation methodology and the finite element models presented in this chapter.

Chapter 4

LP Optimization: Introduction and Parametric Investigations

Mathematical optimization is a process of identifying the best suitable design from a collection of alternatives without having to experiment all possible alternatives. There are many simple problems in which optimal parameters can be obtained through experience and experiments. However, for a nonlinear time-dependent mixed-variable process such as LP, it is difficult determine optimal parameters using this approach. It is necessary to perform a systematic optimization of the LP process.

The LP process has many variables, such as the pressure pulse magnitude and mid-span, spot shape and size, the location and layout of the spots, and the number of shots at the same location. For a comprehensive optimization, parametric investigations are needed to determine the performance function sensitivities with respect to optimization variables. The optimization of the LP process is a mixed-variable optimization problem because pressure pulse

magnitude and duration, spot shape and size, and amount of overlap are continuous, while the number of shots and spot layout are discrete. The time dependent nature of the process increases the complexity because each shot is a nonlinear plastic process. This process creates residual stresses and properties of these stresses affects the selection of the parameters of the subsequent shots.

Overall, the main objectives of this chapter are (1) to present the mathematical formulation of a mixed-variable optimization problem, (2) to introduce gradient- and non-gradient-based optimization methods and surrogate models, and (3) to perform parametric investigations.

4.1 Mathematical Formulation of Mixed-variable Optimization

Sometimes, an optimization problem has input variables that are continuous, integer, and discrete. Such problems are called mixed-variable optimization (MVO) problems. A typical mathematical formulation of an MVO problem is defined as

$$
\begin{aligned}
&\text{Maximize:} && f(X) \\
&Subject\ to: && \\
&Equality\ constraints: && h_i(X) = 0, \quad i = 1,2,...,m, \\
&Inequality\ constraints: && g_i(X) \leq 0, \quad i = m+1, m+2, ..., p,
\end{aligned}
$$

The input vector is

$$X = \begin{pmatrix} x_1^c, x_2^c, \ldots, x_{n_c}^c \\ x_1^i, x_2^i, \ldots, x_{n_i}^i \\ x_1^d, x_2^d, \ldots, x_{n_d}^d \\ x_1^b, x_2^b, \ldots, x_{n_b}^b \end{pmatrix}$$

The variable bounds on each input variable are given by

$$x_i^{cl} \leq x_i^c \leq x_i^{cu}, \quad i = 1, 2, \ldots, n_c,$$

$$x_i^{il} \leq x_i^i \leq x_i^{iu}, \quad i = 1, 2, \ldots, n_i,$$

$$x_i^{dl} \leq x_i^d \leq x_i^{du}, \quad i = 1, 2, \ldots, n_d.$$

$$x_i^{db} \leq x_i^b \leq x_i^{bu}, \quad i = 1, 2, \ldots, n_b.$$

where $f(X)$ is the objective function, $x_i^c \in R^c$, $x_i^i \in R^i$, $x_i^d \in R^d$, and $x_i^b \in R^b$ denote sets of continuous, integer, discrete, and binary (zero-one) variables, respectively, and x_i^{*l} and x_i^{*u} denote the lower and upper bounds of the respective variables (replace $(*)$ with $c, i, d,$ or b). The total number of variables is $n = n_c + n_i + n_d + n_b$, and the total number of constraints is p. Here $n_c, n_i, n_d,$ and n_b are the number of continuous, integer, discrete, and binary variables.

4.2 Optimization Methods

Optimization algorithms are broadly divided into two categories: (i) Gradient-based algorithms, and (ii) Non-gradient-based algorithms. All the optimization algorithms are iterative in nature. The gradient-based algorithms move from the current point to the next point based on gradients/sensitivities. In this process of moving points, the objective function and constraint values tend to improve. In a population-based approach, in each iteration, based on a set of rules, a new population is generated from the previous population. Population based methods may not use gradient information.

There are many algorithms (both gradient and non-gradient) that treat all kinds of variables as continuous variables and round-off the values of integer and/or discrete variables. Some methods also use the penalty function approach to handle integer and discrete variables. Most gradient-based algorithms are designed for optimization problems with only continuous variables because of their need for gradients. An algorithms to solve such problems is branch and bound [74]. Recently, many evolutionary techniques (genetic algorithm and particle-swarm optimization) have been used to solve mixed-variable optimization problems.

4.2.1 Gradient-Based Methods

Gradient-based optimization methods use the objective function, constraints functions, and gradient information to guide the search strategy. The gradient

information can be obtained from the first- and/or second-order derivatives of the objective function and constraints. The formulation of gradient-based optimization is given by Equation 4.1:

$$\vec{x}^{(k+1)} = \vec{x}^{(k)} + \alpha^{(k)}\ \vec{d}^{(k)} \tag{4.1}$$

where $\vec{x}^{(k+1)}$ is the next point, $\vec{x}^{(k)}$ is the current point, $\alpha^{(k)}$ is the step-length parameter or distance to travel to reach the $(k+1)^{th}$ point from $(k)^{th}$, and $\vec{d}^{(k)}$ is the unit direction vector. Most gradient based-optimization algorithms are about finding the direction vector ($\vec{d}^{(k)}$) and distance ($\alpha^{(k)}$) to travel in that direction.

Popular methods to find the appropriate direction are Newton's method, the Marquardt modification of Newton's method, the steepest descent method, the gradient projection, the reduced gradient method, the conjugate gradient method, the Davidon-Fletcher-Powell method, the feasible direction method, and the penalty function methods. Many of the direction finding algorithms mentioned above also have approaches to find $\alpha^{(k)}$, and other popular methods use simple differentiation, the equal interval search, the bisection method, and the golden section search.

4.2.2 Non-gradient Based Optimization

Generally, non-gradient based optimization algorithms are population-based probabilistic methods, also called Evolutionary Algorithms (EA). These al-

gorithms may not use gradient information. Simulated Annealing (SA), Genetic Algorithms (GA) [75, 76], Ant Colony Optimization (ACO), and Particle Swarm Optimization (PSO) are a few examples. Two of these methods, the Genetic Algorithm and Particle Swarm Optimization are briefly presented in the following sections.

Genetic Algorithm

GA belongs to the class of natural adaptive optimization algorithms that mimic the process of natural evolution. Since the pioneering work of John Holland, who proposed the possibility of a genetics-based search to solve optimization problems, genetic algorithms have emerged as a robust, stochastic search method in complex problem domains ranging from process optimization, controls, scheduling, motion planning, pattern recognition, and structural optimization. However, since GA is a population-based approach, it requires a large number of function evaluations.

Particle Swarm Optimization

PSO is an algorithm proposed by Kennedy and Eberhart [77], motivated by social behavior of organisms such as bird flocking and fish schooling. Like evolutionary algorithms, PSO is a population based approach. This population is modified from the current iteration to the next iteration based on a set of rules. This set of rules tends to mimic the problem solving, social behavior of group of birds. In this set of rules each individual (particle) has its fitness, and

a communication structure, assigning neighbors for each individual to interact with. These individuals iteratively calculate their fitness solutions and remember the location of their best fitness so far. The information of the best locations of each neighboring individuals is available to all neighboring individuals and the best of all the individuals is also available to every individual. Based on this information, movement parameters of each individual particle are evaluated. These movement parameters change over the course of iterations and the particles tends to converge and provide an optimum solution. Although PSO is a powerful algorithm, it tends to be converge slowly on some problems, and as a result takes a large number of function evaluations.

4.2.3 Advantages and Disadvantages

This section discusses the advantages and disadvantages of gradient- and non-gradient-based methods. The gradient-based methods tend to need a large number of function evaluations for gradient evaluation. EAs tend to be robust, but also require a large number of function evaluations. This is a major issue for problems like LP because of the humongous computational time and space required to perform a large number of simulations. The disadvantage of gradient methods is that the final solution may depend on the starting point of the algorithm and tends to converge on local optima. Nevertheless, these methods clearly improve next point and termination for an optimal solution. EAs have a disadvantage: a solution in the population is always compared to other solu-

tions in the selection, not in absolute terms, and these methods do not have the concept of optimal solution.

EAs can approach a near optimal solution quickly, but can take a large number of iterations to find an exact optimum. EAs are suitable for parallel processing environment because of the population-based approach, but gradient approaches are not because the calculation of the next point depends on the previous point (Equation 4.1). However, parallel computing can be utilized to calculate derivatives/gradients for gradient-based methods. Gradient-based methods are not suitable for handling discrete variables without adjustment, but evolutionary algorithms can easily be adjusted to handle discrete variables.

PSO is selected to solve the LP optimization problems. Along with all the advantages of EAs, PSO is selected because of its ease of implementation, lower number of user parameters, and the use of historical information.

4.3 Automated Data Transfer Procedure

Due to computing and licensing limitations, the computing is done in two parts. The simulation-based design/ optimization process generates the input FEA files on a personal computer (Windows PC). The LP finite element analyses are performed at OSC (Unix). To perform analysis, data must be transfered between these to computers. A manual data transfer method is not the most efficient option. An automated procedure is developed that does not require login and password for each transfer from PC to supercomputer. Although the

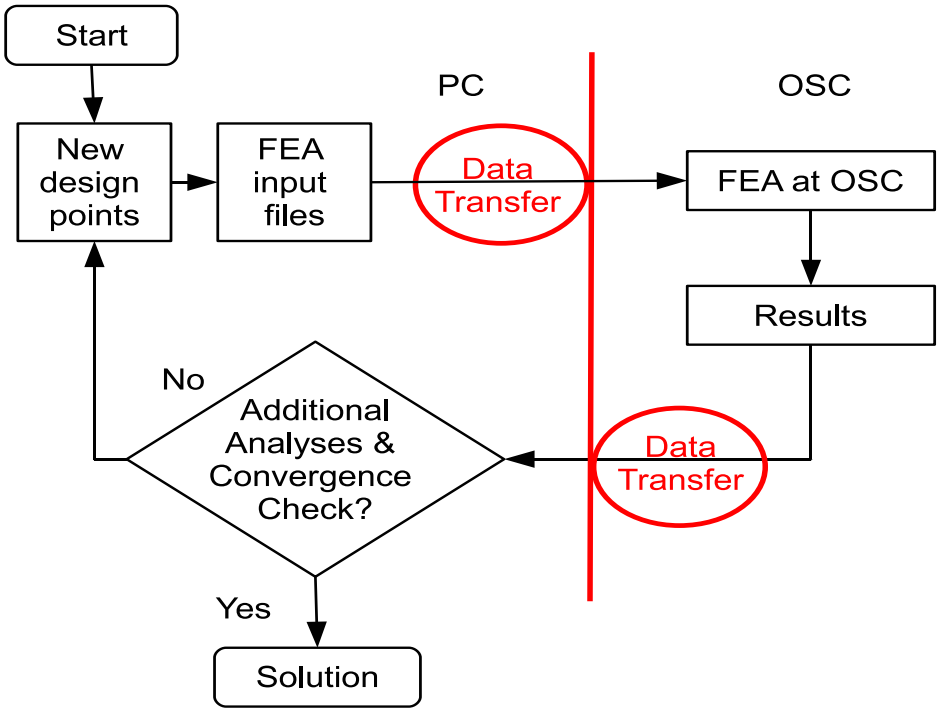

Figure 4.1: Flow-chart of the simulation-based optimization process

process does not require password, it is secure as per current security standards. A one time paraphrase is used for security. A modern programming language, PuTTy, is used for automated data transfer. A successful transfer depends upon the reliability of the connecting network between computers. However, the procedure is independent of minor network issues. This independence is achieved by iterative attempts. Many attempts are made to transfer data. The time between two attempts increases exponentially with the number of failed attempts. An optimization loop will not crash if a PC is not able to connect to the server for few minutes or few attempts.

Access to OSC, knowledge of basic Unix and batch processing, and experience in a programming language are a few requirements that must be met to successfully implement the procedure. The software packages MATLAB and PuTTY are employed to develop the procedure (Figure 4.1). The activities on the left hand side of the vertical line in the figure are performed on a PC. The activities on the right hand side of the line are performed at the OSC. These software packages provide a set-up that generates input files on a PC, transfers the files to OSC, performs the analyses at OSC, and brings result files to the PC. A brief descrption of the procedure is given in the following sections. Further details can be seen in Ref. [78].

4.3.1 One-time Setup

There is a one-time setup needed to use the process. The setup includes two steps, installing PuTTy and setting up a password-less SSH connection. In the first step, PuTTy software is installed. The software is a legally free to download. This software is to implement Telent and SSH for Win32 and Unix platform. In the second step, a password less paraphrase protected process is installed. The details of the process installation are available at the OSC website (http://www.osc.edu/supercomputing/software/apps/mdcs.shtml). Only the step 2.1 is needed from the web-page. The remaining steps on the web-page are for Parallel Computing Toolbox (PCT) of MATLAB software. For assistant and any issue, OSC user can contact OSC help at oschelp@osc.edu. After one-time setup is complete, the procedure is verified as given by at the end of the same step 2.1.

4.3.2 Procedure Steps

In this research, the main organizing tool of the procedure is MATLAB. Any programming language such as C, C++, C#, fortran, python, or VB can be used for the same purpose. The optimization code (PSO), finite element analysis input files generation codes (for ABAQUS), the PuTTY management, and fatigue analysis files generation code (for fe-Safe) are written in MATLAB. As shown in Figure 4.1, the procedure involves following steps.

(a) Generate finite element input files at the PC. The number of files depend upon the number of particles in the optimization.

(b) Employ PuTTy to transfer all files to the OSC cluster.

(c) Perform FEA at OSC using ABAQUS. The request to start all analyses is given at the same time.

(d) Generate the required result files.

(e) Transfer the results files from the OSC cluster to the PC using PuTTy.

(f) Perform additional analysis at PC, if required.

(g) Check for the convergence. Stop, if converged. If not converged, create new points from the previous points and the results. Repeat the process.

4.3.3 Advantages of the Procedure

This procedure overcomes the licensing limitations and optimally utilizes the computing facility of OSC. This procedure is ideally suited for the research groups that do not have supercomputers available at hand and depend upon OSC. Overall, the automation procedure has many advantages:

(i) This procedure is suitable for a population-based optimization methods (PSO). The procedure assists in performing many analyses (equal to population size) at the same time at OSC.

(ii) Many design processes involve more than one software packages to compute the performance function (ABAQUS and fe-Safe for fatigue life optimization using laser peening). The developed procedure removes the

limitations that all the licenses must be available on a particular PC/cluster. This is due to the automated data transfer between computers.

(iii) This procedure allows an optimal utilization of the OSC computing and licensing resources.

4.4 Surrogate Models

A surrogate model or function approximation is a mathematical model that represents the relations between dependent variables or responses and independent variables. Surrogate models play an important role in the design of experiments as models for prediction, in process optimization, and in uncertainty quantification, especially for large-scale analysis. There are many techniques of approximation, such as one-point, two-point, and multi-point models. Among one-point surrogate models, linear, reciprocal, and conservative metamodels are the most commonly used in structural optimization. Two-point Adaptive Nonlinear Approximation (TANA), Improved Two-point Adaptive Nonlinear Approximation (TANA2), and the Response Surface Method (RSM) are a few examples of two-point and multi-point metamodels.

The use of surrogate models in general as well as in this research is not to replace the full scale simulation with approximations. Surrogate models are employed during intermediate steps in an optimization process with the aim of reducing the computational time. The full-scale simulations are performed after each iteration. The goal is to employ an effective surrogate model, and

a minor difference in a surrogate model prediction tends not to affect the final solution. The effectiveness of the surrogate model does affect the number of iterations and computational time required to reach a converged solution in an iterative algorithm.

4.5 Parametric Investigations

The work discussed in Chapter 3 provides a validated simulation procedure for the LP process. At the validation stage for comparison between the experimental and simulation results, the parameter selection for the simulations was constrained by the available experimental results. In parametric investigations, different practically possible parameter variations are explored to determine their effect on the residual stress field. The parametric studies employ models presented in Chapter 3. These models include symmetric 3*D* (Figure 3.3), a modified version of symmetric 3*D*, sequential LP simulation model (Figure 3.11), and Cylindrical model (Figure 3.12). There are multiple objectives and multiple constraints [79] in the LP process. Out of those, four performance metrics- depth of compressive stress (CD), maximum compressive (MC) stress, maximum tensile stress (MT), and total compressive volume (CV)-are selected for comparison.

These performance metrics are calculated after the averaged residual stress profile is calculated for the entire model. The CD is calculated at a selected location. The number of nodes (along the depth) in compression at the selected

location are determined. The number of elements are one less than the number of nodes. The number of elements multiplied by element thickness provides the compressive stress depth at the selected location. The maximum compression and tensile stresses are determined using maximum and minimum finding algorithm. These algorithms find the values from the entire profile. The compressive volume is calculated by determining the number of nodes in compression. The nodes near the surface are checked for compressive stresses. The compressive stress region that is generated at the bottom of the component (below tensile region) is not considered in the volume. The number of nodes in compression are divided by the total number of nodes. The resulting quantity is then multiplied by the total volume in compression.

4.5.1 Temporal Variation of Pressure

This parameter is defined by the variation of pressure with time, also known as pressure pulse shape. The pressure pulse shape is dependent upon the temporal variations of the laser beam. For LP applications, two types of laser shapes are typically used. The first type of shape is similar to a Gaussian distribution curve. It has a gradual rise and similar decay. This shape takes 74.5 ns to reach its peak value, stays at maximum for the next 3 ns, and then drops to zero in the next 74.5 ns. In the second shape, the pressure increases to the peak within 3 ns, stays at maximum for the next 3 ns, and then reduces slowly to zero in 152 ns. The areas under both curves are the same, and the duration is 152 ns.

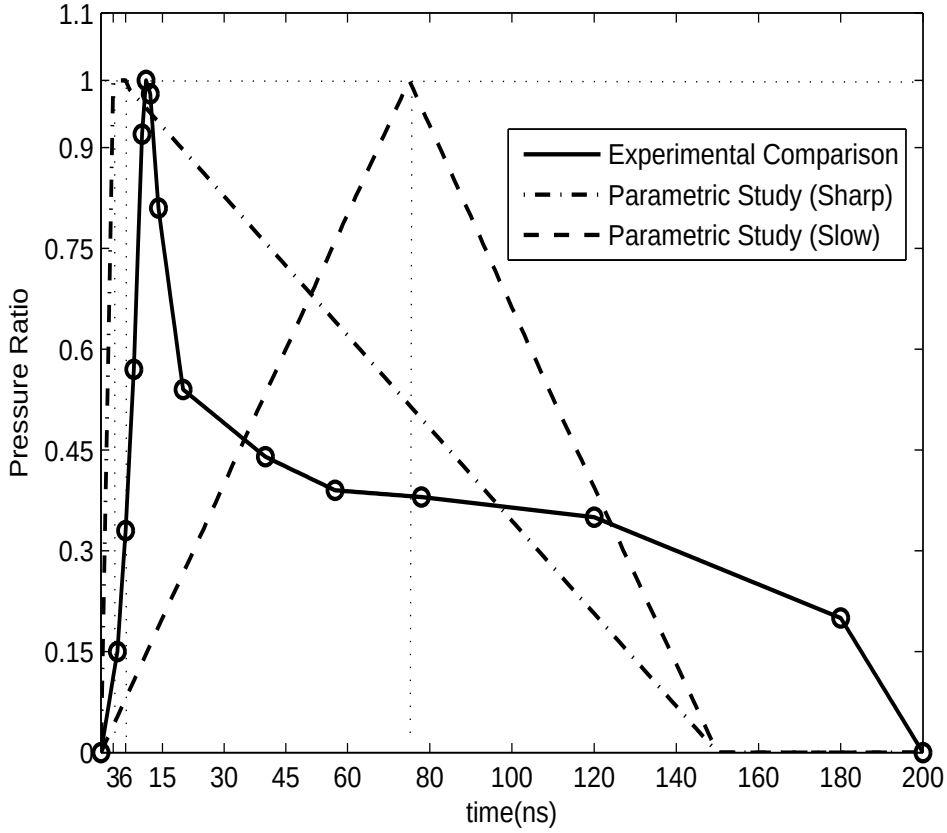

Figure 4.2: Temporal loading profile of pressure pulse

Both shapes are shown by dashed lines in Figure 4.2. It should be mentioned here that the total pulse duration is 152 ns for this part of the research; otherwise, pulse duration is 200 ns (used in experimental validation) for the rest of the dissertation. The peak magnitude in this study is 5.5 *GPa*. The total duration can be decreased or increased depending upon the laser generation mechanism. The sharp and slow shapes generate compressive depth (mm) of 1.46 and 1.21, maximum compression (MPa) of -478.6 and -489.5, maximum tension (MPa) of 139.0 and 127.8, and compressive volume (mm^3) of 7.14 and 6.84, respectively. These results show that both generate approxi-

mately similar results.

The magnitude of the peak pressure depends upon the laser beam intensity. In addition, the use of a confining mechanism increases the peak pressure by 4 to 10 times. Increasing the pressure by increasing the laser beam intensity is ultimately limited by the onset of dielectric breakdown in the confinement water layer at higher laser beam intensities. When this breakdown occurs, the laser energy no longer couples into the expanding plasma underlying the water, and the pressure increase ceases. Although simulations show that both temporal profiles generate similar results, to avoid the effects of the breakdown phenomenon a sharp-rise pulse is preferred over a Gaussian pulse. In the case of a sharp rise, peak pressure is built in the very beginning, before the breakdown happens.

4.5.2 Pressure Pulse Magnitude

The magnitude of the pressure pulse, which is dependent on laser beam intensity, is the most important parameter in the LP process. Three peak pressure pulses of 4.0 GPa, 6.0 GPa, and 8.3 GPa, are used to compare the effects. The pressure pulse shape and duration are shown using a solid line in Figure 4.2. The results are shown in Table 4.1. The results show that higher pressure produces higher depth, magnitude, and volume of compressive stress, and an increase in the tensile magnitude.

Table 4.1: Results of pressure magnitude and spot radius comparison

	Pressure Magnitude (GPa)			Spot Radius (mm)		
	4.0	6.0	8.3	1.00	1.75	2.50
CD (mm)	0.61	0.98	1.6	0.86	0.97	0.96
CV (mm)	3.38	5.87	8.12	1.42	3.34	5.17
MC (MPa)	-282.2	-487.3	-831.3	-212.4	-362.2	-374.6
MT (MPa)	39.8	79.94	199.1	36.04	46.2	60.4

4.5.3 Spot Size

As mentioned in Section 3.1.1, a bigger spot size tends to produce a higher magnitude and volume of compressive residual stress for the same peak pressure. This fact is verified in this parametric research, in which three spot radii- 1.0, 1.75, and 2.5 *mm*-are used for comparison without changing any other parameters. The pressure pulse magnitude is 5.0 *GPa*. The four performance metrics are shown in Table 4.1. The simulation results show that the bigger spot size produces higher magnitude, depth, and volume of compressive stress. In these comparisons, location is not considered. The value of maximum compression can be different in the three cases. The increase in volume can be attributed to the increase in the size of the spot shape.

4.5.4 Spot Shape

As noted in Section 3.1.1, rectangular and circular shapes are used most often. This section investigates only small variations of circular shapes. These variations are generated by changing the ratio of the small diameter to the large

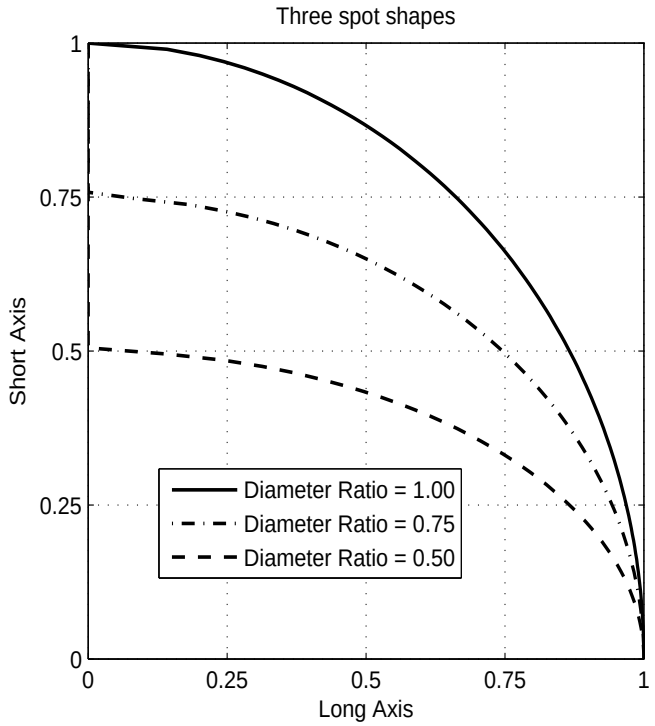

Figure 4.3: Three spot shapes investigated

diameter of an ellipse. The three spot shapes used in this study are shown in Figure 4.3. This figure shows a quarter of each spot shape. The three spot shapes are generated by considering three diameter ratios (1.0, 0.75, and 0.50). The pressure pulse magnitude is 5.0 *GPa*. The radius of the circle (diameter ratio 1.0) is 2.50 *mm*. The highest diameter of remaining elliptical shapes (diameter ratio 0.75 and 0.50) is 2.50 mm. The smallest diameters are 1.875 *mm* (for diameter ratio 0.75, $0.75 * 2.50 = 1.875$) and 1.25 *mm* (for diameter ratio 0.50, $0.50 * 2.50 = 1.25$). As shown by the solid lines in the figure for the diameter ratio 1.0, the spot takes a circular shape. The residual stress fields at the center, shown in Figure 4.4, are compared to the three cases. The figure shows a reduction in the compressive stresses at the surface, with in-

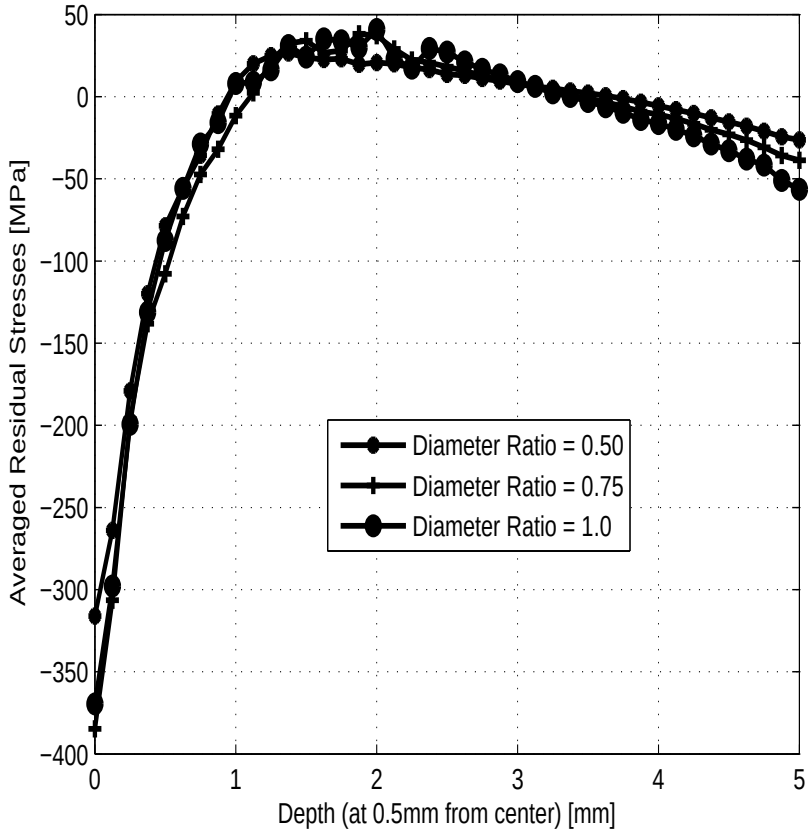

Figure 4.4: Residual stress field for three spot shapes

Table 4.2: Results of spot shape comparison

	Diameter ratio		
	1.00	0.75	0.50
Depth (mm)	0.96	1.1	1.0
Volume (mm)	5.17	3.97	2.56
Maximum Compression (MPa)	-374.6	-387.4	-405.71
Maximum Tension (MPa)	60.4	48.7	35.31

crease in the diameter ratio. For the ratios 1.0, 0.75, and 0.50, the maximum compressive stresses are -374.6, -387.4, and -405.71, respectively. These represent 3.6% and 8.5% increase from the baseline values. The maximum tensile stresses are 60.4, 48.7,and 35.31, respectively. These represent 19.4% and 41.5% decrease from the baseline values. These results indicate that spot shaoe change can significantly reduce the maximum tensile stresses with minimal change in the maximum compressive stresses. The four performance metrics (depth of compressive stress, maximum compressive stress, maximum tensile stress, and total compressive volume) for each case are shown in Table 4.2. The table shows that variation in compressive and tensile magnitude are not similar. The reduction in tensile stress is higher as compare to compressive stress. This parameter should be employed to comtrol the tensile stress.

4.5.5 Thickness of Component

The components to be peened come in various shapes and sizes, and these boundary conditions can significantly affect the peening process. Therefore,

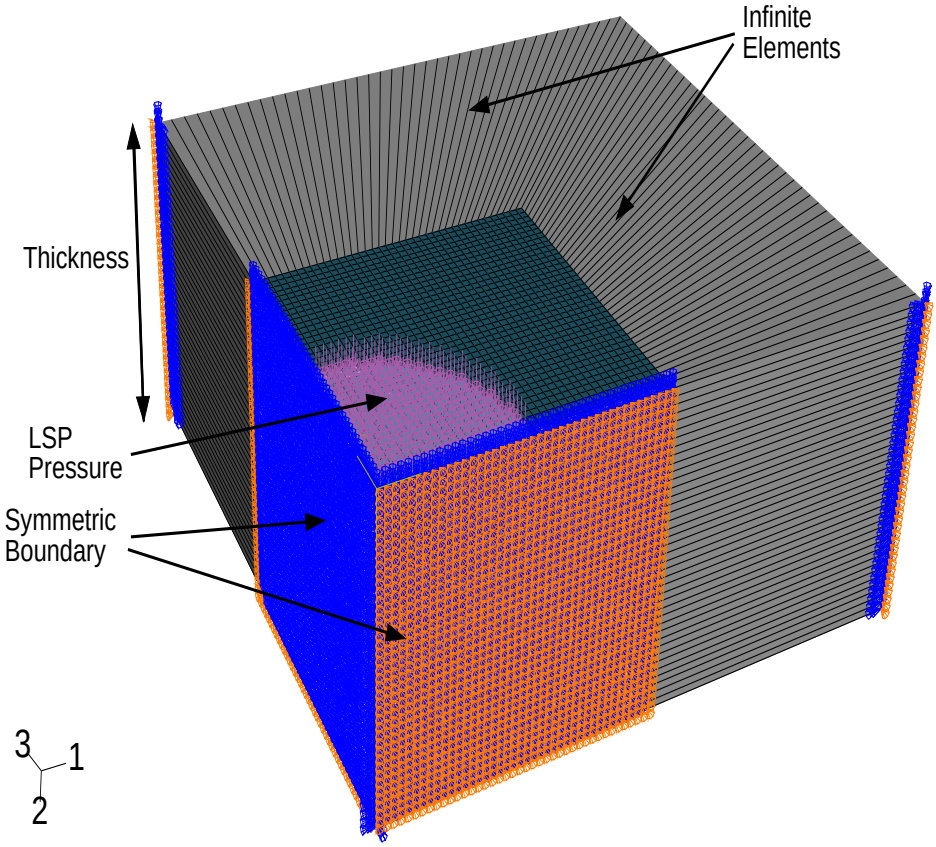

Figure 4.5: Residual stress field comparison for depth from 3 mm to 10 mm

component thickness is a parameter that requires close examination. Since the thickness of a component is the distance traveled by the shock waves in one direction, it can have considerable effect on shock wave propagations and the resulting residual stress profile. In this section, the effect of the component thickness is investigated for cases when the peening surface and the surface on the opposite side are parallel to each other. The FE model for thickness investigations is shown in Figure 4.5. The model is a modified version of the quarter symmetric $3D$ model shown in Figure 3.3. The model is modified by removing the infinite elements in the bottom of the model and replacing them

with finite elements. The total thickness of the component varies from 3 *mm* to 10 *mm* in increments of 1 *mm*. Normally components less than 3 *mm* in thickness tend not to have parallel surfaces. The element size changes in the direction marked by thickness in Figure 4.5. Using the thickness and mesh convergence study, an appropriate unbiased mesh is selected. A finer mesh is used for smaller thicknesses (< 5 *mm*) and a comparatively coarser mesh is used for larger thicknesses. In both cases the mesh is equal to or finer than the converged mesh. The residual stress σ_{11} along the thickness at 1 *mm* from the center is plotted for all the cases.

A comparison of residual stress profiles for various thicknesses is shown in Figure 4.6. These results show that the component thickness affects the residual stress at the surface when the thickness is less than 4 *mm*. The residual stress profile in the area of interest is not affected significantly by the thickness when the thickness is more than 4 *mm*. The figure shows that residual stress variations are much higher for components of 3 *mm* compared to higher thickness components. The plots in Figure 4.6 show the presence of residual compressive stress at the surface opposite to the peened surface. The magnitude of these stresses is significant (> 50 *MPa*) when the thickness is in the range of 3 to 7 *mm*. A comparison of four performance measures is shown in Table 4.3. The results indicate that initially (3 to 5 *mm*) the depth of compressive stress increases with the thickness and then saturates upon further increases in thickness. A potential explanation for these results is that from

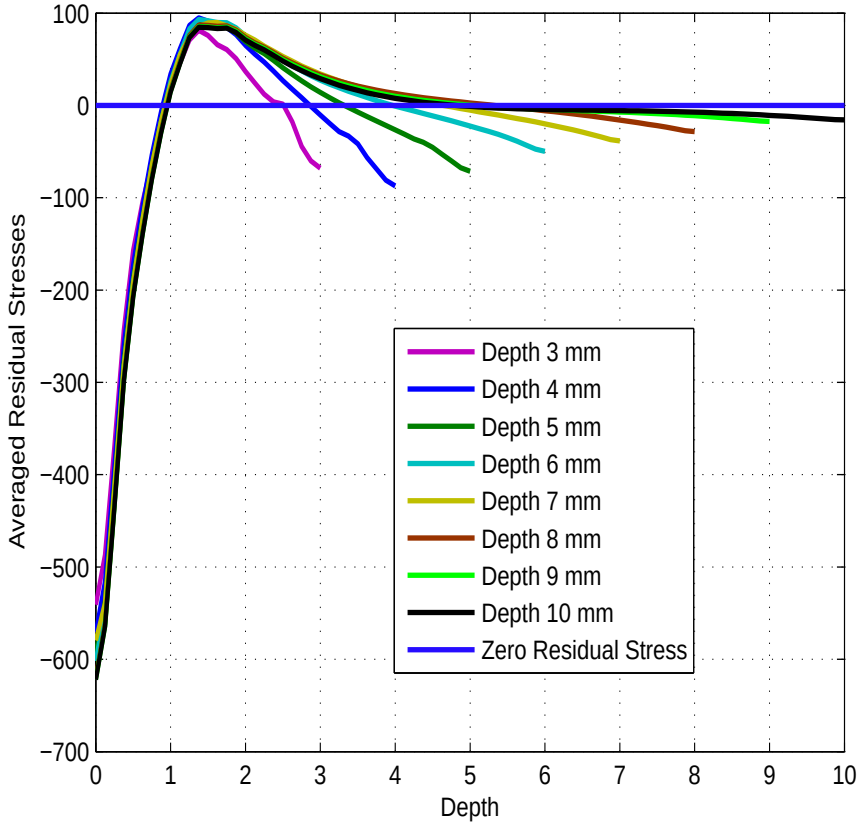

Figure 4.6: Residual stress field comparison for depth from 3 mm to 10 mm

Table 4.3: Comparison of LP performance for various component thicknesses

Thickness (mm)	Volume (mm^3)	Depth (mm)	Maximum Compression (MPa)	Maximum Tension (MPa)
3	8.8	0.72	-555.9	97.1
4	7.3	0.85	-576.6	154.7
5	8.1	0.85	-596.1	120.4
6	7.2	0.86	-604.0	104.9
7	8.8	0.86	-587.2	98.0
8	9.1	0.86	-620.9	98.1
9	9.8	0.86	-623.6	96.6
10	10.1	0.86	-623.6	95.9

3 to 5 *mm*, the plastically affected depth is constrained by component thickness. From 5 to 10 *mm*, the plastically affected depth is limited by pressure pulse magnitude and material properties. Table 4.3 shows that the magnitude of maximum compressive stress increases with the component thickness.

The maximum tensile stress tends to increase up to 4 *mm* and then starts to decrease with increase in the thickness. Initially, tensile stresses increase with compressive stresses; this is not true after 5 *mm* in thickness. One reason could be that the initial increase maintains equilibrium between the tensile and compressive regions. Later, the volume of the tensile region increases to maintain equilibrium instead of the magnitude.

Further investigations into the results indicate that the location of maximum compressive and tensile stress do not change significantly with thickness. The location of maximum compressive stress is always on the surface of the component. The location of maximum tensile stress is also similar in all cases and is always below the compressive region. The trends of compressive volume do not seem to follow any particular direction. The compressive volume increases when thickness varies from 5 *mm* to 10 *mm*; however, it does not follow any specific trend in the remaining range of thickness. Although the results obtained from the simulation indicate some trends and point toward potential explanations, further investigation will be required.

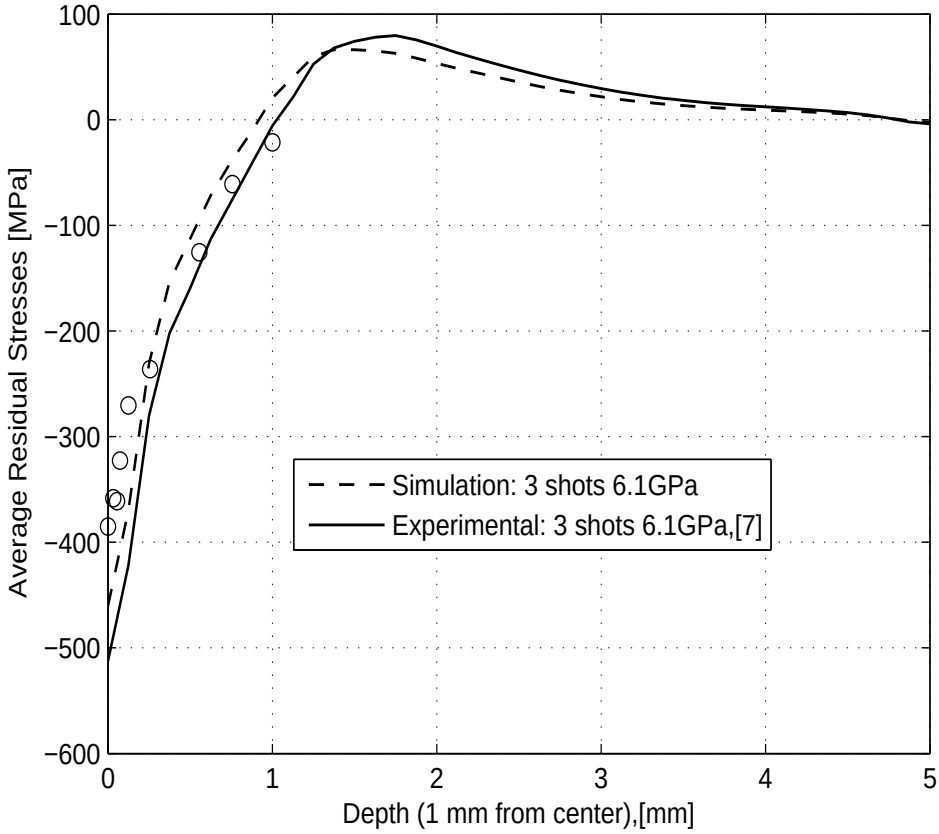

Figure 4.7: Average residual stress field for multiple treatments of LP at the same location

4.5.6 Multiple LP Treatments at the Same Location

A single LP treatment may not be able to achieve the depth, magnitude, or volume of compressive residual stress required for an application. The depth of compressive residual stress can be increased by increasing the intensity of the laser beam, but for certain applications, increasing the intensity may not be the best choice because of two reasons. After a certain limit, saturation may occur, and the depth may no longer be increased by increasing the intensity. Also depending upon the material properties and the process parameters, higher intensity can cause a reduction in compressive stress at the center of the spot,

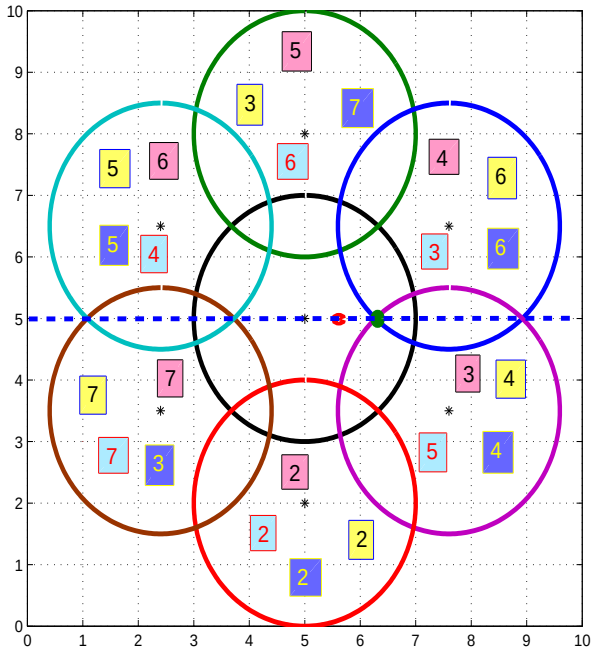

Figure 4.8: Investigated sequences

because of the release wave. In such cases, using multiple treatments of LP at the same location is an excellent option.

All simulation parameters in this study are taken from convergence study. It is believed that one LP shot has the potential to change the material properties at and around the first laser spot. This effect can be considered similar to a welding process behavior. In welding, the material properties change after one weld-pass. The physics of the phenomenon is approximated in the multi-pass welding simulations. However, in this research, for the simulation of multiple treatments of LP, it is assumed that the changes in material properties are not adversely affecting the residual stress field and therefore not considered.

In simulations, the time difference between two shots is equal to the total

simulation time. Here, the total simulation time is approximately 1 to 2 milliseconds. In real life the time difference is much higher and depends upon the frequency of the shots. The change in residual stresses is not significant after 1 millisecond. The provided time difference between two shots is assumed to be sufficient. The simulation for the second shot begins from the residual stress distribution of the first shot. The required properties of the model are transfered to the next simulation from the previous simulation. Figure 4.7 shows the distribution of residual stress at 1 mm from the center line of the spot after three 6.1 GPa applications of LP. These results are compared with published experimental [9] results. In the case of the three 6.1 GPa peak pressure pulses, the following results are obtained. The application of the second LP treatment at the same location increases the depth and the peak magnitude of the compressive residual stress by 19.18% (from 0.73 mm to 0.87 mm) and 42.56% (from 238.5 MPa to 340 MPa), respectively. The depth of the compressive residual stress increases by 17.24% (from 0.87 mm to 1.02 mm) and 20.9% (from 340 MPa to 409 MPa) after the third LP treatment. In summary, improvements obtained by using multiple treatments of LP at the same location are significant, but at the same time, the magnitude of the residual tensile stress also increases. Comparison of results for single and multiple treatments of LP at the same location also shows that the adopted methodology is reasonably good at predicting residual stress distribution.

4.5.7 Two Shots Sequence at Multiple Locations

This section performs simulation of sequential LP at multiple locations for two configurations. The first configuration considers two LP locations that contact each other without overlap. In the second configuration, there is a 50% overlap between the two LP locations. The model developed in Chapter 3 and shown in Figure 3.11 is employed for these investigations. The figure shows a schematic of sequential LP at multiple locations with 50% overlap between the two locations. In the figure, the control volume has two overlapping spots and infinite elements all around. In the case of 0% overlap, the control volume dimensions are 5 *mm*, 5 *mm*, and 15 *mm*, and in the case of 50% overlap, the dimensions are 5 *mm*, 5 *mm*, and 12.5 *mm*. Different sizes of control volumes are used to minimize computational expenses. Both configurations use the biased mesh properties from the mesh convergence study.

Using a Pentium(R) 4 CPU, 3.40 GHz personal computer with 2.00 GB of RAM, it takes approximately 48 Hours of CPU time to finish the two shots analysis. Typically, depending upon the size and requirements of a component, it may need anywhere from 20 to 100 LP treatments. Therefore, the time taken for two shots is an indication that the FE simulation for a practical component will be a computational challenge and a suitable application of surrogate models [80] is required.

For sequential LP at multiple locations, the peak pressure of the pulse is 5.5 GPa. Figure 4.13 shows the residual stress distribution at the top surface and

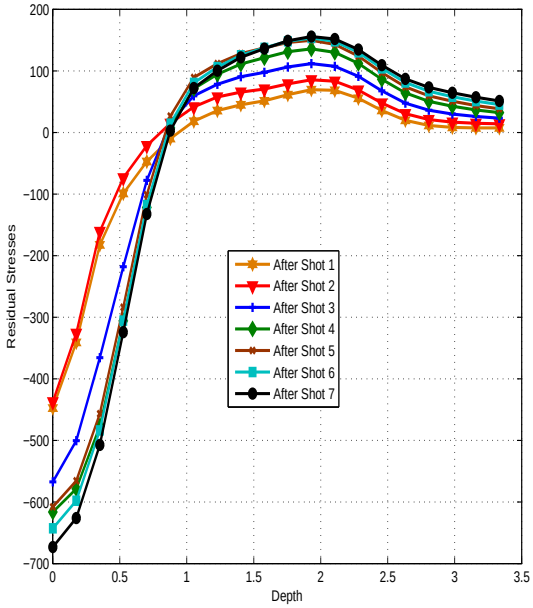

Figure 4.9: Sequence A along the line

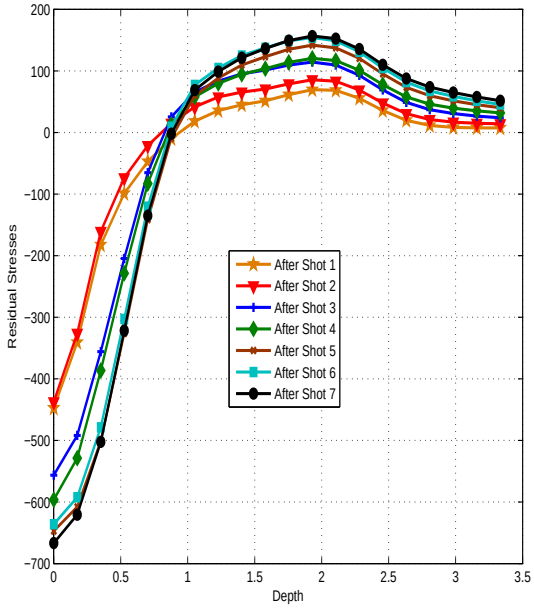

Figure 4.10: Sequence B along the line

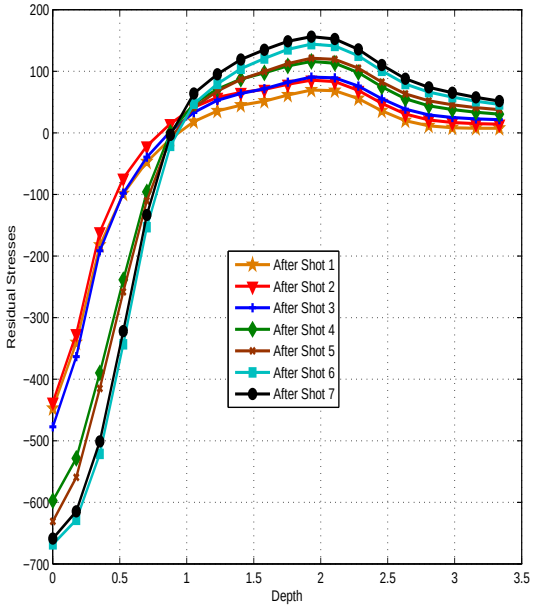

Figure 4.11: Sequence C along the line

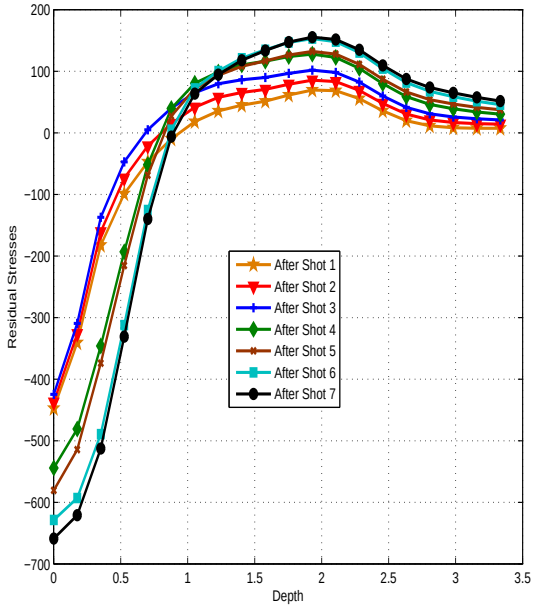

Figure 4.12: Sequence D along the line

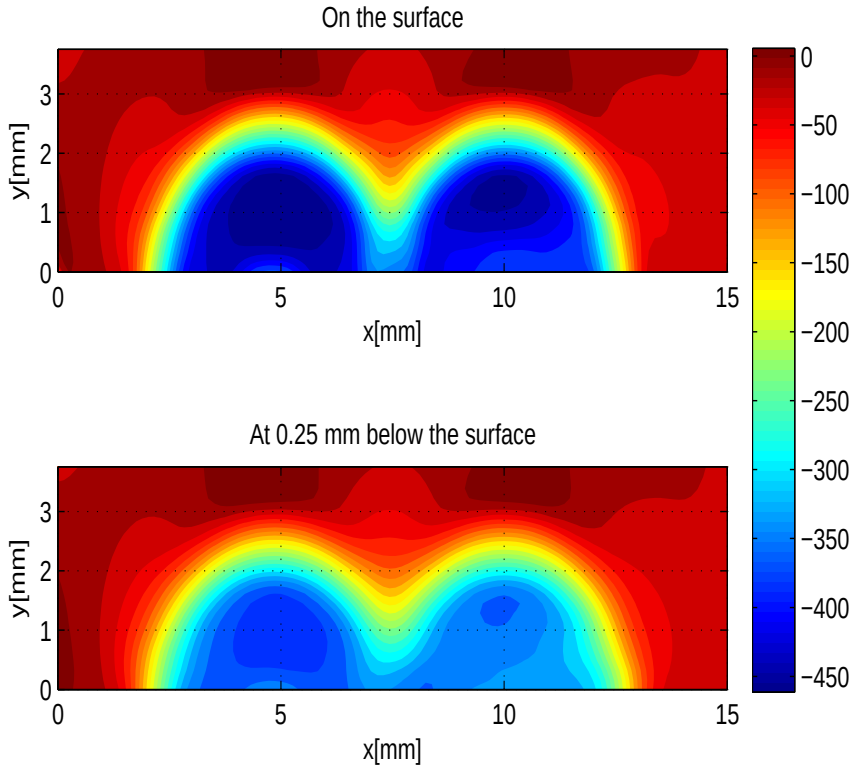

Figure 4.13: Residual stress profile on surface with 0% Overlap

at a depth of 0.5 *mm* from the surface of the component for zero overlap. The results shown in these figures are averaged. The averaging procedure is explained in Chapter 3. The figure shows that compressive stresses are reduced at 0.5 *mm*, compared to the top surface. The As the depth increases, the magnitude and area of the compressive stress magnitude decreases. This shows that the residual stress distribution tends to be uniform across the laser spot area. it is important to note is that although there is no overlap between the two LP locations, there seems to be some interaction between the two fields. The plot shows the merging of the stress fields generated by different shots.

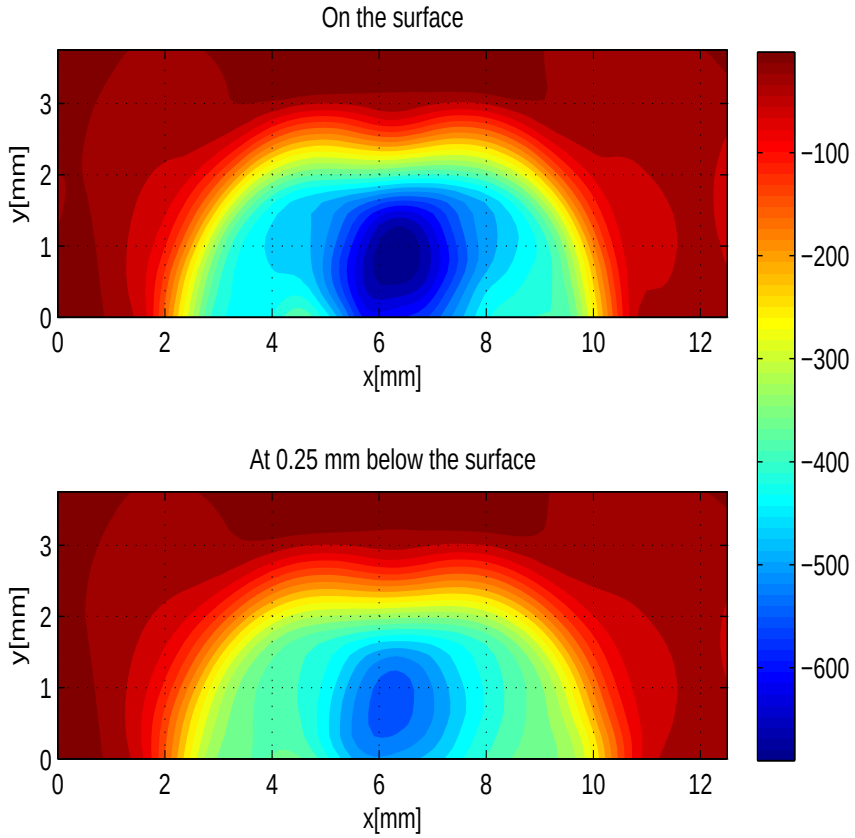

Figure 4.14: Residual stress profile on surface with 50% Overlap

Figure 4.14 shows the residual stress distribution at the surface and at 0.5 *mm* from the surface for 50% overlap. The simulation results show that the magnitude of the residual stress is greater in the area of overlap as compared to the non-overlapping area. Compared to 0% overlap, the magnitude of residual stress is higher. The results indicate significant interaction between the residual stress fields induced by both LP locations. It is interesting that the major effects of LP are limited to a small region and the minor effects are spread over the entire region. Investigation into the results reveal that overlap between two LP locations improves the magnitude and the depth of the resid-

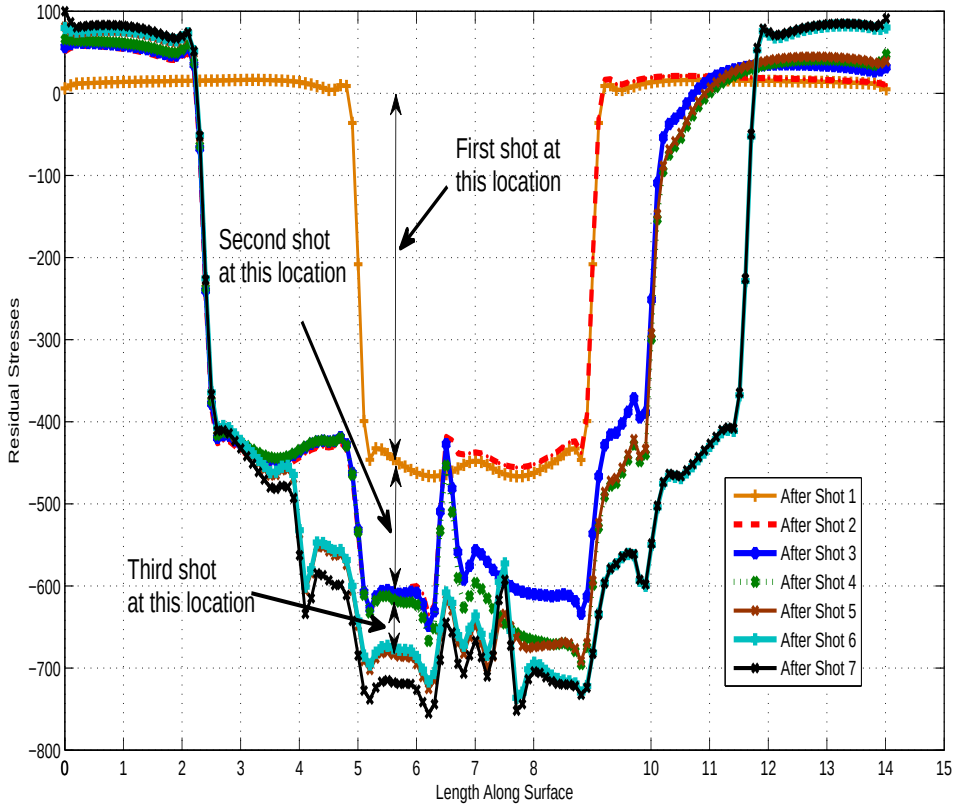

Figure 4.15: Change in residual stress profile at a line on surface by seven shots

ual stress. Along with this improvement, overlapping can eliminate the small, shallow region of reduced compressive stress at the center of the circular spot.

4.5.8 Seven Shot Sequence at Multiple Locations

In this section seven shots are performed in four different sequences to determine the effect of shot sequence. A cylindrical model developed in Chapter 3 and shown in Figure 3.12 is employed in these investigations. The figure shows the locations of seven shots. The four sequences investigated for comparison are shown in different colors in Figure 4.8. A line is selected that

starts on the surface and continuing into the depth, to compare the residual stress profile generated by each sequence. Figures 4.9 through 4.12 show the residual stress profile after each shot of sequences 1 (pink), 2 (light blue), 3 (blue), and 4(yellow). These plots show that the effect of a shot on the residual stress profile depends upon the distance between the point and the shot.

The shots can be divided into three categories. In the first category, the residual stress profile changes significantly when the point is in the peened area. These type of shots tend to increase the magnitude of compressive stress as well as tensile stress. In the second category, changes in the profile are minor but positive. Increases occur in the magnitude of both compressive and tensile stresses. In the third category, a shot tends to reduce the magnitude of compressive and tensile stresses. These reductions are very minor compared to the increases in the first and the second categories. Further investigation is required to determine the exact distances of each category.

The effect of multiple shots at the same location are investigated in Section 4.2. The configuration investigates only 100% overlap; however, partial overlap (20%, 43%, 75%, etc.) is common in many applications. The exploration performed in this section provides an oppurtunity to investigate the effects of number of shots and partial overlapping. Figure 4.15 plots the residual stress profile along a line on the peened surface after each shot. The selected line is shown by a dotted line in Figure 4.8. Figure 4.15 shows that the first shot at any location induces the maximum magnitude of compressive stress. In this

study, for the combination of pressure pulse magnitude (4.5 GPa) and material (Ti-6Al-4V) properties, the compressive stress is approximately -450 MPa. The second shot at this location increases the magnitude to -610 MPa. The third shot at the same location with partial overlap increases it to -700 MPa.

This results indicates that full or partial overlap at a location increases the compressive stress magnitude on the surface. The increase after the second shot is higher than the increase after third shot. Overall investigation in this section shows that the number of shots and the layout of the shots makes a significant difference in the residual stress profile. However, sequence of shots does not make a considerable difference for the selected geometry and the selected LP parameters.

4.6 Chapter Summary

The chapter begins with a standard formulation of a mixed variable optimization problem. This is followed by parametric investigations. The parameters investigated are temporal variation of pressure, pressure pulse magnitude, spot size and shape, component thickness, number of shots at the same location, overlap, and shot sequence. The parameters were investigated with respect to a set of selected performance functions. The functions are volume of compressive stresses, maximum magnitude of tensile and compressive stresses, and depth of compressive stresses. These parametric investigations indicate that our chosen performance functions have significant sensitivities with respect to

the LP parameters. These results motivate us to develop a simulation-based optimization strategy for obtaining maximum benefits of laser peening.

Chapter 5

LP Optimization: One Location

Optimization problems that result in shock, impact, and explosion type disciplines typically have mixed design variables and multiple optimal solutions. In the optimization literature, many researchers have solved problems involving mixed variables or multiple optima, but it is difficult to find multiple optimal solutions of a mixed-variable problem. Therefore, an optimization method is required that can find multiple solutions for a mixed-variable problem.

A mixed-variable niche particle swarm optimization (MNPSO) is developed to solve such problems. The four modifications made to the PSO are: Latin Hypercube sampling-based particle generation, a mixed-variable handling technique, a niching technique, and a surrogate model-based design space localization. The proposed method is developed for a single location laser peening optimization problem.

In many applications of LP, geometric configurations and dimensional integrity requirements of the component can constrain implementation of an op-

timal solution. In such cases, it is necessary to provide multiple alternatives to a designer so that a suitable one can be selected according to the requirements. The finite element analysis time of 24 to 72 CPU hours for each LP analysis makes it a computationally expensive optimization problem to solve.

5.1 Mixed-variable Niche Particle Swarm Optimization

Many engineering optimization problems, such as gearboxes, synchronous motors, and power system operations, involve finding more than one optimal solution. These optima can be local or global. The multi-modality of the design space can cause difficulties for any optimization algorithm being used to find optimal solutions. This is due to convergence toward local optima. In many applications [81, 82], it is beneficial to find multiple optimal solutions. The problem becomes difficult if the design variables are a combination of continuous and discrete variables, and the function evaluation is time consuming. The optimization method demanded by this research should be able solve a multimodal mixed-variable optimization (MMVO) problem without requiring a large number of function evaluations.

Based on advantages and disadvantages (Section 4.2 Chapter 4) [83] of population-based methods as compared to gradient-based methods, population-based methods are more suitable for the problem at hand. Among population-based approaches, particle swarm optimization (PSO) [77] is selected over the genetic algorithm (GA) approach [75, 84] because of its ease of implementa-

tion, lower number of user parameters, and use of historical information.

The first challenge is to incorporate niching ability into PSO, and the second is to introduce a modification to manage mixed variables [85]. Introduction of niching allows PSO to formulate and maintain subpopulations converging toward respective optimum. Thus, niching refers to different optima within the design space that a local subpopulation explores and converges upon. Therefore, an optimization method with niching capabilities is able to find and maintain multiple, diverse, and final solutions.

In the literature, many researchers have developed PSO-based methods [83, 86–90] to solve multimodal or mixed-variable optimization (MVO) problems; however, it is difficult to find multiple solutions of a mixed-variable problem. The GA-based modified clearing method [91] demonstrated niching using 25 variables and 50 peaks problems. However, this method can not be used in this research because it requires a large number of function evaluations. Parsopolos et al. [92] combined PSO, neural network approximation, and threshold value to incorporate niching abilities, but the success of this method depends on the threshold refinement and prior problem information. Brits at al. [93] modified this method, and used particle tracking and subswarm concept to find multiple optima. The performance of this approach also depends upon a threshold parameter and a subswarm radius.

Seo et al. [87, 90] developed the multigrouped particle swarm optimization (MGPSO) method. A traditional PSO has three terms to calculate particle ve-

locity, but MGPSO uses a fourth term to introduce niching properties. Since MGPSO is using an extra term to introduce niching abilities, its interference in convergence is not as much as in other methods. Apart from the interference with PSO convergence, these methods cannot be directly applied to mixed-variable optimization problems.

To manage mixed variables, [83] used the two-level approach. In the two-level approach, the mixed variable optimization (MVO) problem is divided into two problems: system level (mixed-variables) and sub-structural level (continuous-variables) problems. The continuous variable problem is a sub-set of the optimization problem. Similarly, [89] developed a hybrid PSO. The hybrid PSO combines Newton-Raphson and PSO; and solves an MVO problem by dividing it into a two-level problem. Although two-level approach shows that PSO can manage discrete variables, this approach cannot be implemented if the MVO problem cannot be easily divided into two problems. Many researchers [88,94] utilized a penalty function approach to handle mixed variables. This approach artificially modifies the design space, therefore, may require a large number of function evaluations for convergence. Many population based approaches simply round the continuous values to their closest discrete values to manage discrete variable. This approach can be effective for simple problems with wide range of discrete possibilities. A problem dependent systematic approach, employed in this research, can be more effective.

The literature survey shows that it is possible to incorporate niching or multimodal abilities into PSO. In this paper, PSO is modified to incorporate both abilities. An additional term [87, 90] is used in MGPSO to incorporate niching abilities. This concept is employed here because it brings niching ability without extensively interfering in PSO convergence. The interference is lower because the fourth term is not always active. PSO convergence is similar to typical PSO when additional term is not active. In the MGPSO addition term is not active when a particle is not intruding in a territory of other group's *gbest*. In the proposed method, the implementation of this term is different. The particles are not divided into groups, and additional term is active when a particle is in the region of influence of a global or local best ($mbest_i$) found so far. The mixed variables are managed by manipulating the random numbers in the velocity calculation for the integer variable. Apart from these two modifications, a third change is introduced: Latin Hypercube- and surrogate model-based initial population generation. This guarantees that the initial population has particles from all regions of the design space and preserves the random properties.

Population-based methods require many function evaluations. Multidisciplinary structural simulation can be computationally expensive [95, 96]. In the literature [97, 98] surrogate models are employed to mitigate these characteristics. In the proposed approach, a surrogate model is employed for an exhaus-

tive search of the design space. This exhaustive search indicates the location of the potential optima. This approach provides an effective starting population without many simulations to locate multiple optimal solutions. To construct the surrogate model and to perform multiple simulations for optimization, a parallel [99, 100] processing capability is developed. This capability employs MATLAB, PuTTy, and the Ohio Supercomputing facilities to generate the surrogate model and to run the optimization algorithm. The proposed method is first validated on multiple test functions from the literature. Once validated, the method is implemented to solve the laser peening (LP) [53, 101, 102] optimization problem.

The remainder of this chapter is organized as follows: Section 5.2 presents the MMVO problem formulation. The proposed MNPSO is discussed in Section 5.3. In Section 5.4, the modified PSO is demonstrated in test problems and results are compared with the MGPSO-based method. Section 5.5 presents a design of experiments based surrogate model and the solution of the LP optimization problem.

5.2 LP Multimodal Problem

Surface improvement by laser peening is a trade-off between two opposing effects: the creation of compressive residual stress on the surface, which tends to increase life, countered in part by the tensile stresses, which tend to decrease life. Despite these two considerations, in many applications, such as turbine

blades and gears, preserving dimensional integrity is essential. This issue becomes critical for thin (thickness$<$ 10 mm) components.

The literature so far does not apply to thin components or to components with sharp edges or smooth curved boundaries. A high LP pressure applied to a thin target can result in significant permanent deformation on the surface or spall failure on the back surface. A second concern is that the dimensional integrity of the component may be at risk due to high pressure magnitude. The use of two-sided peening to inhibit such losses is not an option because of the interaction of the two tensile waves at the center of the component. This interaction can initiate cracking and hinder the beneficial effects. In such cases multiple lower pressure shots are a potential solution. These conditions make it necessary to find multiple solutions so that multiple options can be provided to a designer. The designer can then select a cost-effective option from the solutions.

5.2.1 LP Design Space for Multimodal Optimization

Residual stress field properties (volume, depth, and magnitude) can be engineered by controlling LP parameters such as pressure pulse magnitude and shape, spot size and shape (continuous), and the number of shots (integer). The five parameters that are considered in optimization are pressure pulse magnitude (p) and midspan (t), shot radius (r) and shape (s), and number of shots (n). Figure 3.1 shows the pressure pulse magnitude and midspan. The pressure

pulse magnitude can vary between 2.8 to 8.8 *GPa*. The figure shows magnitude on a 0 to 1 scale. The pressure pulse shape is changed using the pressure pulse midspan. The midspan is defined by the full width at half the maximum of the pressure pulse. The lower and upper bounds of this variable (t) are 30 and 70 nanoseconds (ns), respectively. For pressure pulse shape, a sharp rise to peak in 3 *ns* is preselected, peak pressure is maintained for the next 3 *ns*, and the rate of drop is determined by the variable (t). The range of the variable is such that this can generate any type of pulse between sudden (lower limits) and slow (upper limits) pressure drops.

The size (r) and shape (s) of the spot are other parameters that can be controlled. The shape parameter defined by the diameter ratio can vary between 0.5 and 1.0. The range of radius is 2.0 to 3.0 *mm*. The combination of these two variables can generate many possible shapes and sizes. Figure 5.1 shows six possibilities of the quarter spot shape. The largest possible spot is shown using a black line and a yellow triangular marker. The radius (r) of this shape is 3 mm and shape parameter (s) is 1.0. The smallest possible spot is shown using black lines and red circles. In this case, radius is 2.0 *mm* and shape parameter is 0.5. The number of shots are indicated by *n* and can vary between 1 and 3. There are a total of five design variables (p,r,t,s,n). To evaluate possible designs for optimization, finite element analysis of LP (Figure 3.3) is employed. Due to the small time increments required to simulate the elastic and plastic deformation, the computational cost of LP simulation is high.

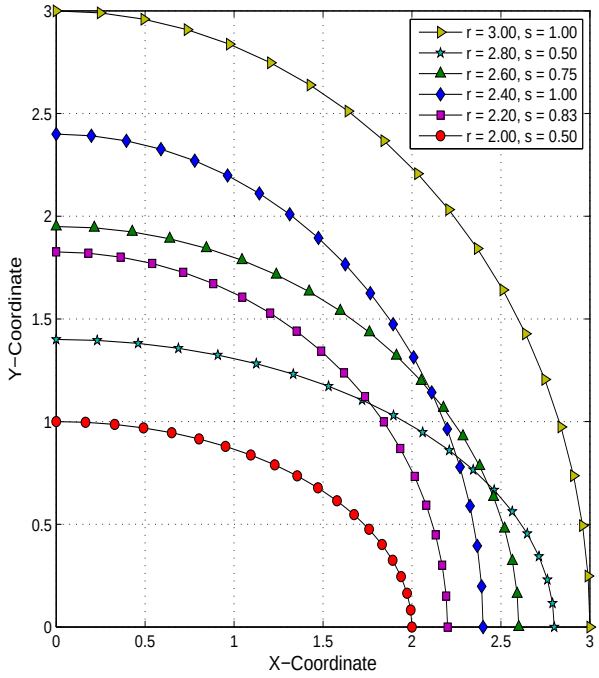

Figure 5.1: Spot shape variables

5.2.2 Multimodal Problem Formulation

The goal of LP is to generate as much compressive stress as possible in the component to improve its surface properties; therefore, the objective of optimization is to maximize the volume of compressive stress. It is possible that higher compressive magnitude may not be beneficial in all cases, but it is almost always certain that the maximum magnitude should be on the surface. To enforce this requirement, the compressive stresses on the surface are constrained to be at or within a certain range of the maximum.

This constraint also accounts for the nonlinear behavior of LP for a certain range of parameters, which can generate a reduced compressive region at the center of the spot. This reduction may hinder the objective of surface enhance-

ment techniques. In mathematical terms, compressive stresses at depth (d) are constrained to be higher or within a certain range at the depth ($d + \Delta d$), where (Δd) is always positive. This is a constraint on the profile of the compressive residual stresses.

The depth of compressive stress is also a performance metric that should be as high as possible. The constraint that compressive stress depth should be more than 1 *mm* at a critical location ensures this requirement. It is not possible to eliminate tensile stress, but it can be kept within a certain limit. The maximum magnitude of tensile stress induced by peening process is controlled by the third constraint. This constraint keeps the maximum magnitude of the tensile stresses below 75 *MPa*.

The optimization problem statement is given by:

$$
\begin{aligned}
&\textit{Maximize}: && \textit{Compressive Volume} \\
&\textit{Subjected to}: && \textit{Compressive Stress}(d) \geq \textit{Compressive Stress}(d + \Delta d) \\
& && \textit{Compressive Stress Depth} \geq 1.0 \ \textit{mm} \\
& && \textit{Maximum Tensile Stress} \leq 75 \ \textit{MPa}, \\
&\textit{Variable Bounds}: && 2.8 \leq p \leq 8.0 \, \textit{GPa}, \\
& && 30.0 \leq t \leq 70.0 \, \textit{ns}, \\
& && 0.5 \leq s \leq 1.0, \\
& && 2.0 \leq r \leq 3.0 \, \textit{mm}, \\
& && 1 \leq n \leq 3,
\end{aligned}
$$

This problem is solved by using the following optimization algorithm.

5.3 Proposed Method: Mixed-variable Niching PSO

It is difficult to find multiple optima by using typical PSO, because PSO has an intrinsic limitation that all particles converge to only one point at final step. Even if PSO is able to find a local optimum in the process of reaching a better one, the algorithm is likely to lose the local one. Therefore, PSO needs to be modified such that it can not only find multiple optima but also retain the ones it finds.

5.3.1 Initial Particle Generation

In the first modification, the initial population is generated using Latin Hypercube Sampling (LHS) [103] instead of random generation. LHS is a popular method for generating samples. This technique maintains the randomness in the population and guarantees the coverage and exploration of the entire design space. The covariance matrix required for LHS is obtained by assuming that all parameters are independent and normally distributed. The following is a brief LHS procedure to generate a sample of size p from q variables:

(i) Divide the design space into p non-overlapping intervals based on an equal probability of selection from each interval.

(ii) Randomly select one value from each interval.

(iii) Repeat Steps (i) and (ii) for each variable of q random variables $x_1, x_2, \ldots, x_q$.

(iv) Pair the p values for each x_i with the p values obtained for the other $x_{i \neq j}$ at random.

5.3.2 Niche Updating

The proposed method takes advantage of the PSO structure to incorporate niching properties, which provide multiple converged local optima. Two changes are introduced to develop the niching capabilities. The first change is a design of experiments-based study to determine PSO parameters and the second change is an additional term [90] to traditional particle velocity calculation equation.

Modified Fourth Term

The traditional PSO equation is:

$$v_i^{k+1} = w_i v_i^k + c_{i1} r_{i1} (pbest_i - s_i^k) + c_{i2} r_{i2} (gbest - s_i^k) \tag{5.1}$$

where v_i^k is the i^{th} particle velocity at iteration k, w_i is the i^{th} particle weight function, c_{ij} is the i^{th} particle weight coefficient of each term (j^{th}), r_{ij} is a random number between 0 and 1, s_i^k is the i^{th} particle position at iteration k, $pbest_i$ is the best value of the i^{th} particle, $gbest$ is the value of the group.

This Equation 5.1 is modified to Equation 5.2.

$$v_i^{k+1} = w_i v_i^k + c_{i1} r_{i1} (pbest_i - s_i^k) + c_{i2} r_{i2} (gbest - s_i^k) + c_{i3} r_{i3} (s_i^k - mbest_i) \tag{5.2}$$

where $mbest_i$ is the best within the specified region of influence. The new constant c_{i3} is calculated using Equation 5.3.

$$c_{i3} = \begin{cases} 1 & if \quad d_{i,mbest_i} \leq d^*; \\ 0 & otherwise. \end{cases} \tag{5.3}$$

where $d_{i,mbest_i}$ is the distance between the i^{th} particle and $mbest_i$, d^* is the user defined distance parameter that controls the region of influence.

To determine $mbest_i$, all the particles are sorted in descending order of their objective function values. In the sorted particles the first particle is the $mbest_1$. Any particles that is within d^* distance of $mbest_1$ can not be $mbest_i$. In the sorted particles, the next highest particles that is not in the region of influence of $mbest_1$ is the $mbest_2$. Similarly, other $mbest_i$ and their region of influence are determined.

The fourth term concept is taken from MGPSO paper but the implementation of the term is different. In MGPSO the term is active when a particles intrudes the territory of the other group's *gbest*. In the proposed method the term is active only when more than q particles are within the distance (d^*) of the $mbest_i$. The distance (d^*) and the number of particles q are parameters the user must provide at the beginning of the algorithm. These parameters can be easily calculated using the problem information. For example, for a two-dimensional, 50-peak function, the number of particles is 200, d^* is 0.05, and p is 4.

If the particle is in a region of influence, its velocity calculation includes the fourth term; otherwise it does not. A particles is considered to be in the region of influence of $mbest_i$, if the distance between the particle and $mbest_i$ is less than d^*. The particles that are moved based on this criterion are expected to improve exploration of the unexplored regions of the search space. Based on the generated random number r_{i3}, the particle is relocated outside the region. This strategy allows PSO particle to converge on the nearest optimum and preserve multiple optimal solutions. This relocation may try to send the particles out of the design space. To prevent this situation, particles are relocated inside the design space.

Cognitive and Social Coefficients

The two constants c_{i1} and c_{i2} play a significant role in preserving the optima already found. A design of experiments-based parametric study is performed to determine the combination of these two parameters that is best suited to preserve these optima. In the study, the constants c_{i1} and c_{i2} is changed from 0.0 to 2.5 in the step of 0.1. This is a full factorial design. There are two factors and 26 levels. The constant values are further refined. This study provides an effective parameter setting for a problem. This study provides a range for both constants instead of a value. Any value of the constants within this range can preserve the multiple optimal solutions. For a two-dimensional 10-peak function, approximately 1.2 (c_{i1}) and 0.01 (c_{i2}) are the best combination for

preserving the multiple optimal solutions.

For $1D$ and $2D$ problems the constants c_{i1} and c_{i2} have the same value through all iterations. For higher dimensional, the constant values are changed with the iteration number [104,]. The constants are changed linearly. The cognitive factor (c_{i1}) starts with a low value c_{i1}^s and linearly increases to c_{i1}^f. The social factor (c_{i2}) starts at a high value c_{i2}^s and linearly decreases to a low value c_{i2}^f. The parameters are updated according to

$$c_{ij}(k) = c_{ij}^f + \frac{k_{max} - k}{k_{max}}(c_{ij}^s - c_{ij}^f) \tag{5.4}$$

Here, k_{max} is the maximum number of iterations and k is the current iteration. The upper and lower bound of the two constants are adjusted for each function independently. For a $3D$, 50 peaks problem, the constants c_{i1}^s, c_{i1}^f, c_{i2}^s, and c_{i2}^f are 1.5, 2.0, 0.1, and 0.01.

The parameter setting provided by the study gives no or minimal importance to the social behavior of the particles (0.01 for $1D$ and between 0.1 and 0.01 for $3D$). Typically, the strength of the population-based approach comes from its social behavior. The purpose of the social behavior is to explore the design space. In case of multimodal optimization problems, it is necessary to explore the design space but it is also important to converge to local optima. The low value of the social constant reduces the exploration. This reduction does not affect the performance of the algorithm significantly because of the additional term in the PSO equation and the parameters q. The additional term and the

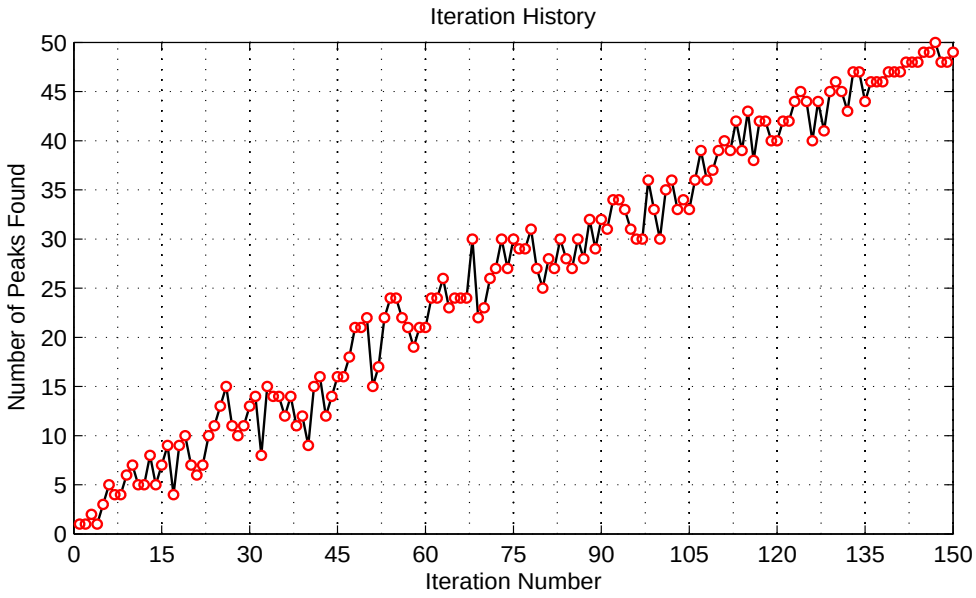

Figure 5.2: Number of Peaks Found w.r.t. Iteration Number

parameters q forces particles to unexplored design space. This argument can be verified by monitoring the number of peaks found at a iteration.

A $3D$ problem with 50 peaks is solved. The problem details and the PSO parameters are shown in Section 4.2. Figure 5.2 shows the number of peak found at each iteration. The figure shows that number of peaks found are increasing with the number of iterations. One of the reason for finding more peaks as iteration increases is that modified PSO is forcing particles to explore unexplored design space. This result shows that the modifications are bringing niche ability with minor effects on the exploration capabilities of the PSO.

Advantages and Disadvantages

This method has multiple advantages and disadvantages over the multigrouped particle swarm optimization (MGPSO) method. The first advantage over MG-

PSO [87] is that in the proposed method particles are not divided into groups. Therefore the group parameters and calculations required for to form are not needed. The second advantage is that there is a limit to the maximum number of particles (q) that can converge to an optimal solution. This forces more particles to explore the design space. In MGPSO, there is no limit on maximum number of particles in a group. A disadvantage is that the proposed method needs an additional parameter (maximum number of particles around a peak, q). The calculation of this parameter is very simple. This is approximated by dividing the total number of particles by expected number of optima. The third advantage is that the proposed method uses dynamic coefficients instead of constant. This approach modifies the particle behavior depending upon the iteration number. This modification of constants assist the particles to converge to multiple optima.

5.3.3 Integer Variable Technique

A minor alteration in the random numbers r_{ij} of the velocity calculation (Equation 5.2) can help manage the integer variables. Due to the spacing and range of the integer variable, there are only a limited number of possibilities. Based on the random numbers, one possibility is selected. For example, if there are two possibilities for a random number, below or equal 0.5 indicates to the first, and above 0.5 indicates to the second possibility. If there are three possibilities the threshold will be 0.33, if four possibilities then 0.25, instead of 0.5. This

modification allows both continuous and integer variables to be used in the procedure with no inconsistency.

$$
\begin{aligned}
v_i^{k+1} &= w_i v_i^k + c_{i1} r_{i1}(pbest_i - s_i^k) + c_{i2} r_{i2}(gbest - s_i^k) + c_{i3} r_{i3}(s_i^k - mbest_i) \\
&= 0.5 \times (1) + 1 \times r_{i1}(2-1) + 1 \times r_{i2}(3-1) + 1 \times r_{i3}(1-2) \\
&= 0.5 + 1 \times \{0.0, 0.5, 1.0\} \times (2-1) + 1 \times r_{i2}(3-1) + 1 \times r_{i3}(1-2) \\
&= 0.5 + 1 \times 0.5 \times (1) + 1 \times r_{i2}(2) + 1 \times r_{i3}(-1) \\
&= 0.5 + 0.5 + 1 \times \{0.0, 0.25, 0.50, 0.75, 1.0\} \times (2) + 1 \times r_{i3}(-1) \\
&= 0.5 + 0.5 + 1 \times 0.25 \times (2) + 1 \times r_{i3}(-1) \\
&= 0.5 + 0.5 + 0.5 + 0.5 \times (-1) \\
&= 0.5 + 0.5 + 0.5 - 0.5 \\
v_i^{k+1} &= 1
\end{aligned}
$$

The integer handling technique is explained using a example. It is assumed that at iteration k, $w_i = 0.5$, $v_i^k = 1$, $s_i^k = 1$, $pbest_i = 2$, $gbest = 3$, $mbest_i = 2$, $c_{i1} = 1$, $c_{i2} = 1$ and $c_{i3} = 1$. These values are substituted in equation 5.2 and the velocity at iteration $k+1$ is calculated. As shown in the example, three random numbers (r_{i1}, r_{i2}, and r_{i3}) are needed to calculate the velocity v_i^{k+1}. The random numbers are decided in the sequence of r_{i1}, r_{i2}, and then r_{i3}. There are three options 0.0, 0.5, and 1.0 for r_{i1}. These options will make the second term 0.0, 0.5, and 1.0, respectively. Let us assume that a random number

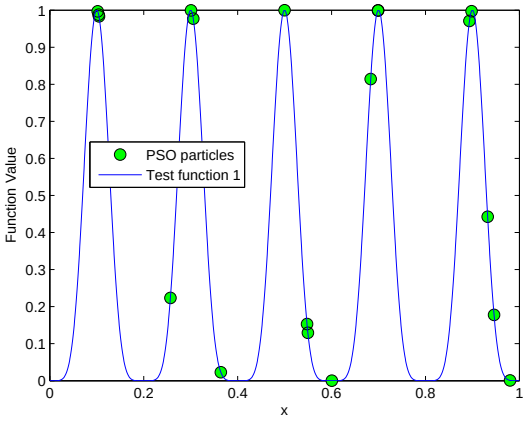

Figure 5.3: Multimodal Test Function 1

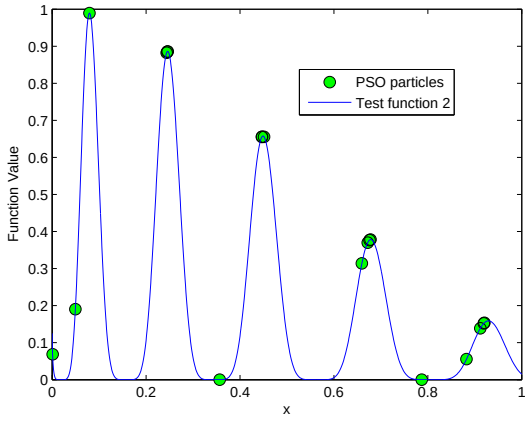

Figure 5.4: Multimodal Test Function 2

generation selected 0.5 out of three possibilities. Therefore, the second term is 0.5. Similarly, there are five options for r_{i2}. For r_{i2}, out of five possibilities random number generation selected 0.25. This makes the third term 0.5. In the fourth term, the random number r_{i3} has only one option. The option is 0.5. The velocity v_i^{k+1} is 1. Similar procedure is used to handle integer variables.

5.3.4 Parallel Processing

PSO and surrogate model development requires multiple finite element simulations of the system under consideration. For example, one simulation can take anywhere from 24 to 72 hours of CPU time using the Glenn cluster at OSC. To manage this cost, an algorithm is developed (using MATLAB and PuTTy) that can submit multiple simulations in parallel to OSC and the extract results. This insures that computational and licensing resources are optimally utilized. A detailed description of the process is given in Chapter 4 of the dissertation.

5.4 Multimodal Test Problems

Before solving the problems, it is important to keep in mind that all the proposed modifications are not required for each function considered in this research. Depending upon the function, one, two, or all three modifications can be incorporated.

5.4.1 A Periodic Function with Peaks of Equal Size and Interval

The first multimodal test function is a $1D$ problem with five peaks of equal height at equal interval. The mathematical formula for the function is shown in Equation 5.5 and the function is plotted in Figure 5.3. The variable range is 0 to 1 and peaks are at 0.1, 0.3, 0.5, 0.7, and 0.9.

$$P_1(x) = sin^6(5\pi x) \tag{5.5}$$

The modification to manage integer variable is not used here because the variable is a continuous one. The constants d^*, g, number of particles, and numbers of iterations used in solving this problem are 0.08, 3, 20, and 100, respectively. All the parameters are selected after investigating effects of each parameter. For example, the number of iterations is selected to be 100 because this makes sure that the algorithm is able to maintain the discovered optima for a large number of iterations. The number of particles is 20 which is sufficient to solve the problem. The circles in Figure 5.3 show the final population of the

modified PSO. The figure shows that the method is not only able to find, but also to maintain the optimal solutions.

5.4.2 A Periodic Function With Peaks of Unequal Size and Interval

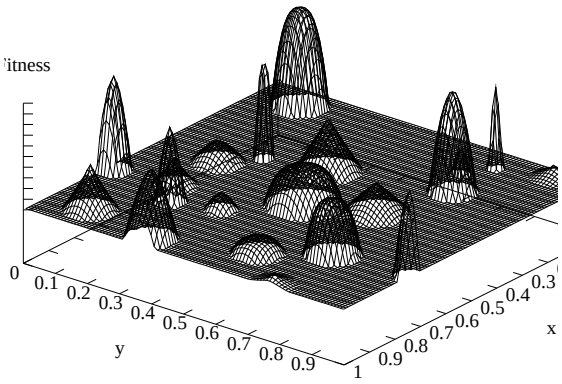

Figure 5.5: Multimodal Bump Function

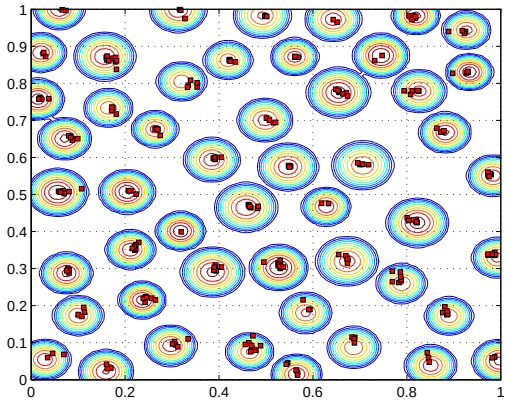

Figure 5.6: Particles for 50 Peak Function

This multimodal test function has five peaks of unequal height at unequal intervals. The function is shown in Figure 5.4. The mathematical formula of the function is given in Equation 5.6. The locations of the five peaks are 0.0796, 0.246, 0.4491, 0.6786, and 0.929 and the corresponding function values are 0.9895, 0.886, 0.6576, 0.3782, and 0.1585, respectively.

$$P_2(x) = e^{-2(\ln 2)(\frac{x-0.01}{0.8})^2} \sin^6(5\pi[x^{0.75} - 0.05]) \tag{5.6}$$

The constants d^*, g, number of particles, and number of iterations used in solving this problem are 0.08, 3, 20, and 100, respectively. The circles in Figure 5.4 show the particles after 100 iterations of modified PSO on the function. The proposed method can find and maintain all the optima for a specified number

of iterations. This problem is solved again after changing the number of iterations to 1000 and keeping all the other parameters same. The final distribution of the particles after 1000 iterations is similar to the distribution after 100 iterations. Similar tests have been performed on all numerical problems. These tests prove that the number of iterations does not matter for the algorithm in maintaining all the optimum solutions.

5.4.3 Multimodal Bump Function

The previous two test functions are one-dimensional functions with only five peaks. Bump function is a parametric multimodal function, in which the dimension, number of peaks, radius of peaks, curvature of peaks, height of peaks, and location of peaks are parametric. This variability allows us to generate many multimodal functions. The mathematical formula for the bump function is given as

$$f(x_i) = \begin{cases} h_k \left[1 - \left(\frac{d_{ik}}{r_k}\right)^{\alpha_k}\right] & if \quad d_{ik} \leq r_k; \\ 0 & otherwise. \end{cases} \tag{5.7}$$

where d_{ik} is the Euclidean distance of the i^{th} particle from the midpoint of k^{th} peak, r_k, h_k, and α_k are the radius, height and shape parameter, respectively of the k^{th} peak, and K is the number of peaks. With the bump function, multiple problems with different levels of difficulty can be generated. The difficulty of the multimodal problem can be changed using parameters K, h_k, r_k, and α_k.

Table 5.1: Radius Range for Bump Functions

	Radius ranges of peaks				
Dim.	10	20	30	40	50
2D	0.08 to 0.10	0.07 to 0.09	0.06 to 0.08	0.055 to 0.075	0.05 to 0.07
3D	0.27 to 0.30	0.19 to 0.21	0.16 to 0.18	0.14 to 0.15	0.13 to 0.15
5D	0.48 to 0.53	0.40 to 0.44	0.32 to 0.35	0.30 to 0.33	0.28 to 0.31

The top view of a two-dimensional bump function is shown in Figure 5.5. The number of peaks K is 20. The range of each variable is $[0,1]$. The center of each peak is randomly initialized, with only one constraint, the distance between the midpoints of any two l^{th} and m^{th} peaks is greater than or equal to $(r_l + r_m)$. The figure shows a function with random location x_k, height h_k, and shape parameter α_k.

The results of the presented method and the MGPSO method are compared [87]. For comparison, 2, 3, and 5 dimensional bump functions with 10, 20, 30, 40, and 50 peaks are generated. The height of the peak is a random number between 0.8 to 1.0 for all the functions. The peak curvatures range between 1.5 to 2.0 for all the functions. The radius is different for each function. Depending upon the number of peaks and dimension of the function, a radius range is selected. The selected ranges are shown in Table 5.1. The radius of a peak is a random number in the range.

These generated functions are solved using the proposed method and MGPSO-based algorithm. The multimodal functions and the PSO parameters are the same for both methods except the parameters that are not common

Table 5.2: Number of Particles to Solve the Function

	Number of Particles				
Dim.	10	20	30	40	50
2D	50	75	100	120	150
3D	60	80	250	500	600
5D	600	1000	1200	1500	2000

in both methods. In the case of the proposed method, the third term is applied to a selected group of particles, whereas in the case of the competing method it is applied to all the particles. The selection criteria are defined with the method description.

Parametric studies have been performed for each function to find the regions of influence (d^*) and p, and the number of particles. Table 5.2 shows the number of particles used in each of the functions. The number of particles for each function is selected using a manual parametric investigation. Figure 5.6 shows the final population of the modified PSO on the $2D$ test function with 50 peaks. The figure demonstrates that modified PSO particles are converging to all the optima, are able to find optima, and are able to maintain it for 100 iterations. To demonstrate the robustness of the algorithm, each problem is solved 10 times with a different initial population of PSO.

The results the of competing and proposed methods are shown in Tables 5.3 and 5.4, respectively. The shown results are the average success rate of the 10 runs. The average success rate and the standard deviation of the success rate is reported. In the tables, Dim., SR, and SD indicate the function dimen-

Table 5.3: Bump Function: Method with MGPSO third term

	Number of Peaks Found									
	10		20		30		40		50	
Dim.	SR	SD	SR	SD	SR	SD	SR	SD	SR	SD
2D	8.8	0.75	18.8	0.75	28.0	1.41	33.2	1.17	41.2	1.78
3D	7.6	1.11	13.0	1.18	25.9	1.45	34.5	1.96	40.4	1.63
5D	7.0	1.10	12.2	1.89	14.2	2.44	20.2	3.25	24.8	3.28

sion, success rate, and standard deviation in the success rate, respectively. The success rate is defined by the number of optima found by the optimizer. The SD is shown to demonstrate that the optimizer is consistent in its performance. An optimum is considered to be found if at least one particle is within a certain distance of the peak. This distance is selected to be 15% of the peak radius. These results demonstrate that the method is able to find multiple optima consistently.

A comparison of the results shows that both methods are able to solve the multimodal optimization problems. The performance of both methods is similar on two-dimensional problems. However, for three-dimensional problems, the proposed method performs slightly better than the MGPSO-based method. The results of the five-dimensional problem shows that the proposed method finds a higher number of optima compared to the other method. The comparison of standard deviation in the success rate shows that the proposed method is more consistent in finding multiple solutions.

Table 5.4: Bump Function: Modified PSO with boolean third term

	Number of Peaks Found									
	10		20		30		40		50	
Dim.	SR	SD	SR	SD	SR	SD	SR	SD	SR	SD
2D	9.6	0.66	19.6	0.66	29.9	0.30	39.6	0.66	49.9	0.30
3D	9.5	0.67	19.2	0.60	28.6	0.92	36.5	1.20	43.6	1.43
5D	9.1	0.70	18.5	0.92	25.3	0.78	33.2	1.25	39.4	1.11

5.5 Multimodal LP Optimization and Results

The LP parameters, mesh properties, material model, and geometric boundary conditions of the 3*D* model can be found in Chapter 3. In brief, the LP simulation employed in multimodal optimization is a symmetric 3*D* model shown in Figure 3.3. This simulation considers pressure pulse magnitude, duration, and shape, spot shape and size, and number shots at the same location as optimization variables. To manage the simulation time, a design of experiments (DOE)-based surrogate model is employed.

5.5.1 Design of Experiments-based Surrogate Model

In many traditional methods, approximation is constructed around a current design point to obtain the next point. However, in the case of LP, only a limited number of simulations can be performed; therefore, a surrogate model that covers the all of the move limits is required for each step. Traditionally, a model is required to predict objective functions and constraints. However, in the case of LP, the residual stress values at all the nodes need to compute the

volume and profile of the compressive stress, magnitude of the tensile stress, and depth of the compressive stress. Therefore, a surrogate model is needed for each node response. In the $3D$ model, there are $68,921$ (41 nodes per 5 *mm*) or $531,441$ (81 nodes per 5 *mm*) nodes, and constructing the response surface for residual stress at each node is necessary to calculate performance metrics (objective and constraints). This surrogate model combines DOE and a multi-point response surface.

To develop a surrogate model, a 3-level full factorial design is considered. Simulations are performed to calculate residual stress values at all the nodes in all designs of DOE. Since there are five variables, a total of $(3^5 =)$ 243 simulations are performed. This set up provides the matrix $[X]$ (Eq. 5.9) and the response vector $[Y]$ for each node to construct a response surface. For each node a surrogate model is assumed as shown in the following equation:

$$\hat{Y} = \hat{\beta}_0 + \hat{\beta}_1 f_1(x) + ... + \hat{\beta}_k f_k(x) + \varepsilon \tag{5.8}$$

where $\beta_i, i = 0,1,2,...,k$, are the unknown coefficients, ε is residue in the regression model, and $f_i(x_j)$ are the functions of individual or combined x_i. The least squares method is used to find unknown coefficients, and it yields

$$\hat{\beta} = (X^T X)^{-1} X^T Y \tag{5.9}$$

$$\hat{Y} = X\hat{\beta}, \qquad e = Y - \hat{Y} \tag{5.10}$$

The above computation (Eqs. 5.9 and 5.10) is performed for each node

response. These calculations provide unknown coefficients $\hat{\beta}$ and $\hat{Y}$ for all nodes.The first advantage of this surrogate model is that this provides the residual stress field of the entire model instead of an objective or constraint value. This field can be used to calculate any quantity needed and can also be used for the purpose of fatigue life calculation. The second advantage is that once the model is developed, it does not need updates at every point unless algorithm reaches a converged point and wish to change or reduce move limits. This is because the surrogate model covers the entire range of design variables.

5.5.2 Results and Discussion

All three modifications of PSO are employed to solve the LP optimization problem. The value of d^* is 1.0, and the value of p is 2. The value of p is 2 because the number of PSO particles is 20. The number of particles is limited to 20 based on available resources. The variable ranges of pressure magnitude and the number of shots drive the selection of d^*. To incorporate compressive stress depth and profile and tensile stress constraints, a penalty function approach is employed. The penalty is proportionate to the magnitude of the constraint violation. The penalty is such that a feasible solution has a better objective function compared to an infeasible solution. This is a modified version of exterior penalty function used in population-based optimization methods.

Two iterations of the modified PSO are used. The first iteration uses the surrogate model. This iteration is a type of exhaustive search of the design space,

Table 5.5: LP Optimization Results

Sol. #	p	n	r	t	s	Obj.	T_{max}	C_{max}	Depth	S
1	3.62	3	2.95	38.1	0.63	4.78	74.7	-612.0	1.50	100.9
2	5.35	2	2.22	46.8	0.69	4.93	74.5	-652.7	1.35	132.5
3	5.59	2	2.78	51.8	0.52	4.97	74.0	-703.7	1.25	148.3
4	6.00	1	2.76	65.5	0.93	5.56	74.9	-603.7	1.25	119.5

because a function evaluation does not require significant computational time. This iteration identifies the potential solutions/regions in the design space, which become part of the initial population for the second iteration. For the second iteration, these potential solutions (particles) are combined with the particles generated using an LHS technique. The second step begins with a population that has representatives of potential optimum solutions. Full-scale simulations are used in the second iteration. Table 5.5 shows the optimization results provided by the modified PSO algorithm.

In the table, Obj. indicates compressive volume, T_{max} indicates maximum uni-directional tensile stress, C_{max} indicates maximum uni-direction compressive stress, and S indicates the maximum principal stress. The algorithm is able to find multiple solutions. The first, second, third, and fourth solutions require 3, 2, 2, and 1 peening shots, respectively. The first solution uses 3.62 *GPa*, the second uses 5.35 *GPa*, the third uses 5.58 *GPa*, and the fourth uses 6.0 *GPa* pressure pulse magnitudes.

The pressure pulse magnitude and the number of shots are the major parameters that vary in the solutions. There is a direct relationship between the

pressure magnitude and the number of shots: higher pressure magnitudes require lower number of shots to produce similar effects. All the solutions satisfy the profile, tensile stress, and compressive stress depth constraints. The active constraints are the maximum tensile stress and the profile of the compressive stress. The maximum tensile stress constraint is active for all the solutions. The profile constraint is active for the second, third, and fourth solutions. A closer examination of the results provides the following information:

(i) There are multiple solutions for the formulated LP problem.

(ii) Multiple shots at lower pressure at the same location create a higher depth of compressive stresses compared to single shot of higher pressure.

(iii) One shot at higher pressure creates higher magnitude compressive stress compared to multiple shots at lower pressure.

(iv) An elliptical spot shape, when compared to a circular spot shape, induces a lower magnitude of tensile stress for the same compressive stress magnitude.

A non-niching optimization method will find only the last solution because it has the highest objective function value. The other solutions obtained using modified PSO can potentially be more useful for certain applications. The objective function value of these solutions is not the same. This shows that first three solutions are local optima. However with these solutions, a designer has multiple options to choose from. Depending upon the effects of the LP param-

eters on a component, an appropriate solution can be selected. For example, when peening leading edge of a turbine blade, where minor dimensional variations can affect its performance significantly, the first solution may have an advantage over the last solution. For an application where the LP parameters' effects are within the allowable tolerances, the last solution can be selected. If a high magnitude of compressive stress is required, then the third solution is better than other solutions. If both depth and magnitude of compressive stress are equally important, then the second solution is better than the other solutions.

Another advantage of multiple solutions is that different equipment can be used to accomplish a set goal. For example if a company has multiple machines with different capacities (laser intensity/pressure magnitude). One of the machine can be busy due its capabilities and not possible to use for all jobs. In such cases, a solution can be picked based on the available machine capabilities. This allows the company to optimally utilize the available resources due to the multiple solutions. Therefore, each of these solutions have advantages and disadvantages over the other solutions, and depending upon the requirements the designer can select the one that is appropriate.

5.6 Chapter Summary Remarks

A MNPSO is proposed to solve the multimodal mixed-variable optimization problem. The MNPSO employs LHS-based population generation, a niching

strategy, and a mixed-variable handling technique. LHS-based generation is used to obtain a diverse population, the niching strategy is used to find and preserve multiple optima, the mixed-variable technique and surrogate model design space localization is used to manage continuous and integer variables. An exhaustive search is performed using the surrogate model to localize potential multiple solutions. The method is demonstrated on multiple test problems and on laser peening optimization. The solution of the laser peening problem provides a designer with multiple options. The designer can select a suitable option depending upon dimensional integrity requirements. The successful demonstration on multiple problems shows that the proposed method can be employed to solve multimodal mixed-variable problems.

Chapter 6

LP Optimization: Multiple Locations

In this research, a progressive simulation-based design optimization strategy is developed that can be applied to highly nonlinear impulse-type processes such as shot peening, laser peening, and bullet impacts on aircraft structural components. The design problems entail the use of multiple fidelities in simulation, time-consuming elastic-plastic analysis, and mixed types of optimization variables. An optimization strategy based on progressively increasing the complexity and fidelity is developed, along with suitable surrogate models. Multi-level fidelity models include axi-symmetric, symmetric 3D, and full-scale simulations to enable design optimization. The first two models are used to perform parametric studies and to localize the potential design space. This creates a reduced design space and an effective starting point for the subsequent optimization iterations. All steps employ the modified particle swarm optimization for mixed variables.

The design methodology is demonstrated on LP of a structural component.

The LP parameters, pressure pulse and spot dimensions, impulse locations (all continuous), number of shots (integer), and the location of shots (discrete)-are the optimization variables with stress constraints.

6.1 Progressive Multifidelity Optimization Strategy (PMOS)

Multidisciplinary optimization of structures subjected to high-speed impact processes is complex due to the nonlinear and transient nature of the finite element analysis. The simulations consist of elastic-plastic analysis with small time steps and large-scale finite element models for practical aircraft structures. The experiments-based design approaches traditionally used are cost prohibitive for parameter optimization. Therefore, a simulation-based design methodology is required. In this research, a design methodology is developed for structures subjected to the shock-type loadings that occur in shot peening, laser peening, explosions, and bullet impacts. The optimization problem is also challenging due to the presence of the continuous and discrete design variables [85], a mixed-variable optimization (MVO) problem.

In the literature, depending upon the geometry, loads, and boundary conditions, multi-fidelity simulation and surrogate models are used to solve aircraft structural analysis problems. Livne et al. [105] used polynomial-based equivalent plate modeling techniques for wing structures analysis. This work demonstrates that 2D models can be used to approximate the nonlinear aeroelastic response of a wing-box subjected to in-plane compressive forces. Robin-

son et al. [106] used physics-based and finite element models with parameter mapping on a wing design problem. This research proved that low-fidelity and high-fidelity models connected with parameter mapping can assist an optimization approach and save computational time. Chen et al. [107] employed multiple objective-oriented surrogate models, each constructed for a local region and combined using a boolean operations. This approach updates the surrogate models based on the preexisting surrogate model and confidence interval on approximation.

Glaz et al. [108] compared a weighted average of multiple surrogate models (design of experiments, polynomial response, kriging, radial basis neural network) to each individual surrogate model and demonstrated the advantage of the weighted-average surrogate [109, 110]. Although these techniques are effective, they may not be the best options for impulse-type mixed-variable problems. In this research, a progressive multifidelity optimization strategy (PMOS) is developed. This strategy combines, low- and high-fidelity simulations [105, 106] and respective surrogate models [107, 108], as well as mixed-variable strategy [85] to solve impulse-type problems.

The basis of PMOS is that, depending upon the problem information and assumptions, multiple simulation models can be developed to approximate the impulse response. Multiple impulses may be required in a process, but the effects of a single impulse at a location can be determined using a single axisymmetric model to address a large-scale problem. However, assumptions in

the model limit the number of variables that can be considered in the model. Similarly, in a symmetric $3D$ model, the number of assumptions can be reduced, so this model can incorporate additional variables. Simulation of an arbitrary structural component with many impulses at multiple locations requires an analysis model without symmetric assumptions. Typically, such models are computationally expensive but can consider most of the variables in the problem. These qualities of the models are utilized in developing the optimization strategy. The uniqueness of the proposed method is that it localizes the design space using axi-symmetric $2D$ and symmetric $3D$ simulation and surrogate models, and determines the optimum solution.

As shown in Figure 6.1, the PMOS involves a three-step hierarchical procedure. The design space is localized by parametric studies and by solving optimization problems with low fidelity models, which also assist in eliminating insensitive optimization parameters. These steps provide an effective starting point and significantly reduce the search space for the third step of the optimization procedure. The reduced design space requires fewer function evaluations in the subsequent optimization step. When employed together these three steps reduce the number of the full $3D$ model simulations.

The developed method is for impulse-type problems. There will always be an integer variable in such problems, for representing the number of impulses. As shown in Chapter 5, the PSO [77, 83] is modified to generate diverse initial population and handle mixed variables. The modifications introduced are

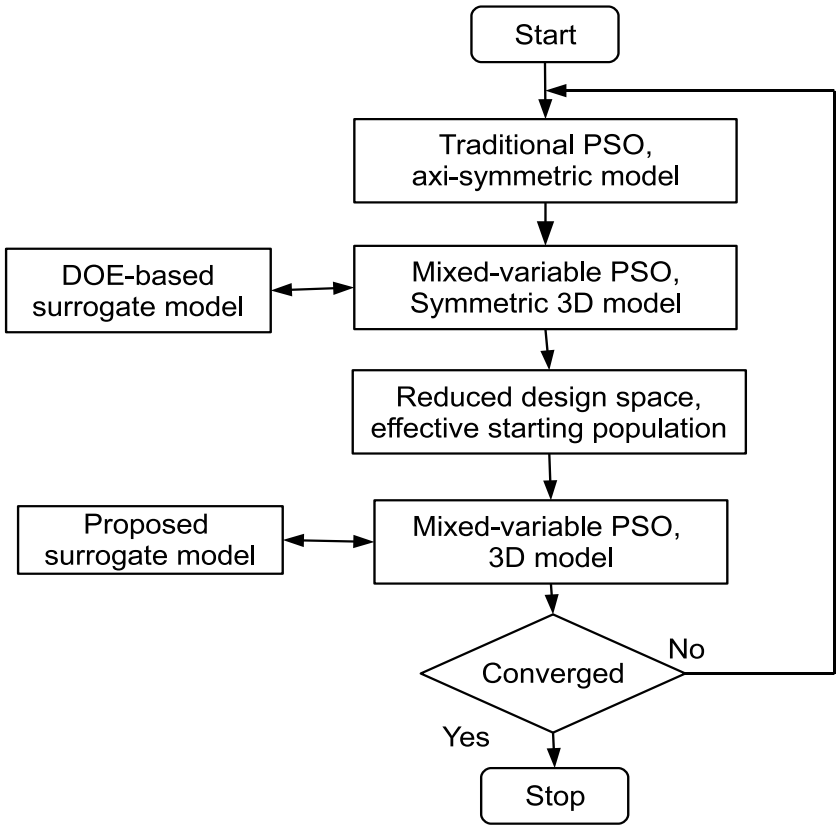

Figure 6.1: Multifidelity optimization strategy

Latin Hypercube Sampling-based initial particle generation and a discrete variable handling technique.

In the first modification, the initial population is generated Latin Hypercube Sampling (LHS) instead of random generation. This modification is explained in Section 5.3.1 of Chapter 5. The second modification is to handle integer variable. This modification is described in section 5.3.3 of Chapter 5. Since there is not an inbuilt termination criterion for PSO, depending upon the objective requirements and available resources, the maximum number of function evaluations terminates the optimization.

6.1.1 Sub-parametric Surrogate Model

An important property of impulse-type problems is the repetition of impulses. A surrogate model is developed for the $3D$ model that utilizes this repetitiveness. This surrogate model is based on the characteristic of an impulse-type problem that each impulse has certain set of parameters that define it. If two impulse locations on a structure are significantly apart from each other and the parameters defining these impulses are the same, then both impulses generate similar local effects. The proposed model exploits this quality of the impulse response. The major advantage of this idea is that it does not require simulation of all impulses at different locations to approximate the cumulative effect of all impulses.

For a traditional design of experiments-based surrogate model, a certain

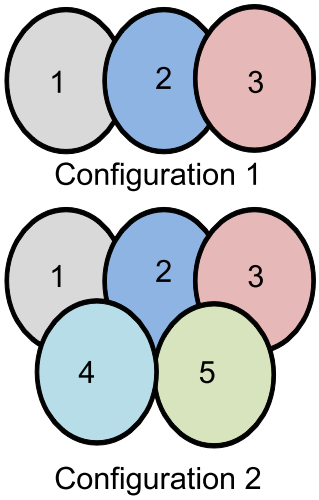

Figure 6.2: Two possible layouts

number of simulations are performed. The results of these simulations are used to construct an approximation. This is not the best approach for nonlinear impulse-type problems due to the computational cost of each simulation. In this surrogate model, instead of performing a complete simulation for each impulse, simulations for two or three impulses are performed to extract the effects of individual parameters. A three-impulse simulation requires less time than a five-impulse simulation while still providing the information required to build a database for the surrogate model. Once all the individual parameters and interaction effects are extracted, they can be combined to approximate the performance for most configurations.

The above concept is explained using two examples. The first configuration in Figure 6.2 shows a three-impulse layout. The effects for this layout can be approximated using simulation of only two impulses, because the third

impulse does not directly overlap the first impulse. Similarly, the second configuration in Figure 6.2 has a five-impulse layout. Since the maximum number of directly interacting impulses is three, multiple three-impulse simulations can be used to approximate the resulting performance. The surrogate models requires shots 1, 2, and 4 to be simulation using FEA. The residual stress profile for shot 3 can be approximated from FE simulation of shot 2. Similarly, the residual stress profile for shot 5 can be approximated from FE simulation of shot 4. After the database is generated, it can be used to approximate solution for the required layout.

Although this surrogate model reduces the computational cost, it has two disadvantages. The first disadvantage is that it partially ignores the effects of impulse sequence. The second disadvantage is that, irrespective of the distance between the two impulses unless they overlap, the interaction effect is neglected. These drawbacks are not significant when compared with the advantages of the surrogate model. Moreover, since full simulations are performed after each optimization iteration convergence, the surrogate model serves as an intermediary interactive tool and the final results are always reached without making any of the above approximations.

6.1.2 PMOS: Advantages and Disadvantages

The proposed strategies have certain advantages and disadvantages. The first advantage is that the proposed strategy utilizes axi-symmetric $2D$ and sym-

metric 3*D* models. The second advantage is that the computational cost is lower than the full 3*D* models. The third advantage is that the stepwise process identifies infeasible regions without performing full 3*D* simulation. A disadvantage is that it is possible to lose some interaction effects among some parameters. This disadvantage can be avoided by performing parametric investigations before attempting the design optimization. Based on these investigations, the optimization strategy can be modified to accommodate the interaction effects.

The fourth advantage is that mixed variables are managed effectively without inconsistency. The fifth advantage is that the proposed surrogate model does not require simulation of all the impulses. Overall, the strategy solves an MVO problem at a lower computational than a traditional approach, without sacrificing effectiveness. The strategy is demonstrated in the laser peening (LP) process.

6.2 Multiple Locations Peening Optimization

The pressure pulse magnitude and shape, spot size and shape, spot location, and number of shots are the optimization variables. There are multiple challenges in implementing the three-step strategy to optimize laser peening with these variable. The first challenge is to develop a simulation model that takes the required LP parameters into consideration. A parametric model is required that can not only consider the above variables but also the location of the

shots, the amount of overlap, and the sequence of the shots (mixed variables). The following sections present models available in the literature and develop a model to implement the optimization strategy.

6.2.1 Multiple Simulation Models

Finite element simulations of a structure experiencing impulses can be performed using multiple models with respective assumptions. Depending upon the geometry and boundary conditions, response to an impulse can be modeled using axi-symmetric, symmetric 3*D*, or full-scale 3D models. Typically, axi-symmetric and symmetric 3*D* models require lower computational times than full 3*D* models. The full-scale 3*D* model requires a higher computational time but can consider more optimization variables than the other two models. A detailed description of axi-symmetric 2*D* and symmetric 3*D* models can be found in Chapter 3.

3D Model

The 2*D* and symmetric 3*D* simulations have applications in one or multiple shots at the same location. Because a typical application may require 10 to 100 locations or shots on a large surface (50 to 500 *mm*), an FE model of such a system can be computationally prohibitive [102]. To investigate the effects of shots at more than one location, the different overlapping configurations, and different sequences of shots, further improvements are needed in the FE

model. A plate model is developed to investigate required parameters. The model is shown in Figure 3.13. The details of the model are in Section 3.7 of Chapter 3.

6.3 Problem Formulation, PMOS Implementation, Validation, and Results

6.3.1 Optimization Formulation: MVO

For impulse-type loading, the objective of an optimization problem can be to minimize cost of the process, minimize or maximize damage, or maximize a performance function. The objective for LP [6, 36, 101, 111, 112]. is to maximize the compressive stress volume in the peened component. The first constraint forces the compressive stresses on the surface to be at or within a certain range of the maximum. This constraint is included to mitigate the effects of the nonlinear behavior of the process, which within certain range of parameters can generate a reduced compressive region at the center of the spot. This reduction may hinder the objective of the surface enhancement techniques.

In mathematical terms, compressive stresses at depth (d) are constrained to be higher or within a certain range at the depth ($d + \Delta d$), where (Δd) is always positive. The second constraint requires that the depth of compressive stress is more than 1 *mm* at a selected location. The maximum magnitude of tensile stress induced by the peening process is controlled by the third constraint.

This constraint keeps the maximum magnitude of the tensile stresses below 150 *MPa*. The design variables are pressure pulse magnitude (p_i) and shape (t_{1i} and t_{1i}), spot shape (s_i) and size (r_i), location of shot (x_i and y_i), and number of shots at the same location(n_i). Here i indicates the i^{th} shot. The lower and upper bounds for each variable are shown in the formulation:

$$
\begin{aligned}
&\textit{Maximize}: && \textit{Compressive Stress Volume} \\
&\textit{Subjected to}: && \textit{Compressive Stress}(d) \geq \textit{Compressive Stress}(d+\Delta d) \\
& && \textit{Compressive Stress Depth} \geq 1.0 \ \textit{mm} \\
& && \textit{Maximum Tensile Stress} \leq 150 \ \textit{MPa}, \\
&\textit{Variable Bounds}: && 2.8 \leq p_i \leq 8.0 \ \textit{GPa}, \\
& && 15.0 \leq t_{1i} \leq 50.0 \ \textit{ns}, \\
& && 50.0 \leq t_{2i} \leq 150.0 \ \textit{ns}, \\
& && 0.5 \leq s_i \leq 1.0, \\
& && 2.0 \leq r_i \leq 3.0 \ \textit{mm}, \\
& && 2.5 \leq x_i \leq 7.5 \ \textit{mm}, \\
& && 2.5 \leq y_i \leq 7.5 \ \textit{mm}, \\
& && 1 \leq n_i \leq 3
\end{aligned}
$$

A traditional optimization can solve the problem formulated above. This will use full scale five shot plate simulations. A plate simulation requires 4 CPU days on the Glenn cluster at OSC. A simulation for three shots at each of the five locations requires 12 days of CPU time. Due to the computational time issues, finding an optimal solution using the proposed optimization strategy is more effective than traditional optimization.

6.3.2 Optimization Strategies Implementation

The three models of LP required for the PMOS, axi-symmetric, symmetric 3*D*, and the parametric plate-require approximately 20, 170, and 5760 CPU minutes, respectively. As a starting point for the three-step optimization strategy, parametric investigations [113] are performed to determine the effects of individual parameters. These investigations find a significant variation in parametric sensitivities with respect to performance metrics. In the first step of the strategy, four LP parameters are optimized using 2*D* simulation. The second step considers four LP parameters (pressure pulse magnitude and duration, spot shape, and number of shots) and uses symmetric 3*D* simulation. In the third step, four parameters (pressure pulse magnitude, spot location and size, number of shots at the same location) are considered.

6.3.3 Step 1: Optimization using a 2D Model

In this section, the first optimization step is implemented employing 2*D* simulation. There are three LP parameters in the optimization: pressure magnitude (p), shot radius (r), and pressure pulse shape (t). As shown in Figure 6.3, the pressure pulse shape is defined using two design variables (t_1, t_2); as a result, there are a total of four design variables (p, r, t_1, t_2). Based on the capabilities of the equipment, the peak pressure (p) range is 3.5 to 8.8 *GPa*, and the spot radius range is 2.0 to 3.0 *mm*. For pressure pulse shape, a sharp rise (peak in 3 *ns*) is preselected, and the rate of drop is determined by the variables (t_1, t_2).

The ranges of the variables are such that these can generate any type of pulse between a sudden (lower limits) and slow (upper limits) pressure drop. The ranges of the two shape variables are 15 to 50 ns (t_1) and 90 to 150 ns (t_2). The optimization problem statement is given by:

$$
\begin{aligned}
&\textit{Maximize}: && \textit{Compressive Stress Volume} \\
&\textit{Subjected to}: && \textit{Compressive Stress}(d) \geq \textit{Compressive Stress}(d+\Delta d) \\
& && \textit{Compressive Stress Depth} \geq 1.0\,\textit{mm} \\
& && \textit{Maximum Tensile Stress} \leq 150\,\textit{MPa}, \\
&\textit{Variable Bounds}: && 3.5 \leq p \leq 8.8\,\textit{GPa}, \\
& && 2.0 \leq r \leq 3.0\,\textit{mm}, \\
& && 15.0 \leq t_1 \leq 50.0\,\textit{ns}, \\
& && 90.0 \leq t_2 \leq 150.0\,\textit{ns},
\end{aligned}
$$

The number of particles and generations in PSO are set at 20. The values c_{i1} and c_{i2} are taken as 1.7. The optimization results show that a peak pressure of 5.42 *GPa*, a spot radius of 2.1 *mm*, and pressure shape parameters of 17.0 *ns* and 150.0 *ns* are needed to achieve the desired residual stress profile. The formulation can achieve the required depth and limit the maximum tensile stresses within the specified limit. The maximum tensile stress constraint is the active constraint at the optimum. It can be seen from the results that the low spot radius can keep the reduced compressive region at the center of the spot to within the limit. The first shape parameter (t_1) is near the lower bound of the variable range, and the second shape parameter (t_2) is at the upper bound

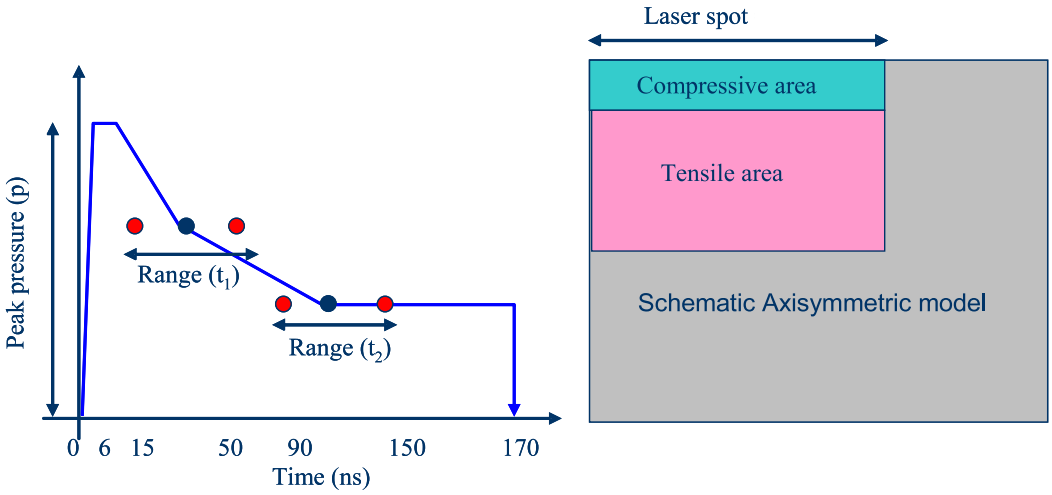

Figure 6.3: Optimization Formulation

of the variable range. This indicates a sharp drop, but a long pressure pulse is favored for the formulation.

6.3.4 Step 2: Optimization using a symmetric 3D model

In this section the second step of the strategy is implemented. Pressure pulse magnitude (p_i), number of shots (n), and laser shot shape (s_i) are the variables. The pressure pulse shape is taken from the previous step, and the pressure magnitude range is reduced for better exploration of the design space. This model obtains a effective starting point from the previous step but experiences computational challenges. A surrogate model is used to reduce the computational expense. A detailed description of the model can be found in section 5.5.2 in Chapter 5.

In pressure pulse magnitude (p_i) and spot shape (s_i) the subscript i denotes the i^{th} shot of the process. In the following formulation, the volume of the compressive region is the objective function. All the constraints and variable bounds for fatigue strength are shown in the equation:

$$
\begin{aligned}
&Maximize: && Compressive\ Stress\ Volume \\
&Subjected\ to: && Compressive\ Stress(d) \geq Compressive\ Stress(d+\Delta d) \\
& && Compressive\ Stress\ Depth \geq 1.0\ mm \\
& && Maximum\ Tensile\ Stress \leq 150\ MPa, \\
&Variable\ Bounds: && 4.0 \leq p_i \leq 6.5\ GPa, \\
& && 0.5 \leq s_i \leq 1.0, \\
& && 2.0 \leq r \leq 2.5\ mm, \\
& && 1 \leq n_i \leq 3,
\end{aligned}
$$

The results of the problem show that two shots with pressure pulse magnitudes of 3.6 and 4.7 *GPa*, radius of 2.28 *mm*, and shape parameters of 1.0 and 0.80 are the optima. The pressure magnitude, radius, and shape variables are guided by the profile constraint. In this optimization the profile constraint is an active constraint.

6.3.5 Methodology Validation

An assumption of the proposed optimization strategy is that a comparatively lower fidelity model (2*D*) can provide a solution similar to that of higher fidelity models (3*D* and plate). To validate this assumption, the problem for-

Table 6.1: Results for methodology validation

Problem Number	Model used	p (GPa)	r (mm)	t_1 (ns)	t_2 (ns)
Problem 1	2D	5.72	2.49	33.5	150.0
Problem 1	3D	5.58	2.44	38.1	110.1
Problem 2	2D	8.00	2.29	33.1	150.0
Problem 2	3D	8.00	2.39	26.6	149.1

mulated for the $2D$ model is solved using both $2D$ and $3D$ models. The same PSO parameters are used for both models. The termination criterion in both approaches is the maximum number of iterations. This is because a population based technique can easily determine the potential region but can require a large number of iterations to find the converged optima.

The results from both models are shown in Table 6.1. The solutions in the table show that results from both models are similar. The table shows that the parameters pressure magnitude (p= 5.72 and 5.58 GPa), and radius (r = 2.49 and 2.44 mm) are similar for both models. The pressure pulse shape parameters (t_1 and t_2) are different in both solutions. In the $2D$ solution t_1 is greater, and in the $3D$ solution t_2 is greater. These differences cancel each other out to some extent, creating similar results.

A second problem is also solved using both models. The second problem is the same as that of the first problem, except that the constraint on the residual stress profile is removed (the first constraint from the formulation in Section

3.4). Table 6.1 shows that the results from both models are similar. The results of the second problem indicate that the pressure magnitude has a direct relationship with the compressive stress profile. The pressure magnitude value is at the maximum possible. The radius and shape are not at maximum to control the reduced compression at the center of the spot. This study shows that $2D$ simulation can be employed to save computational time and that the assumption made in the optimization strategy is reasonable.

6.3.6 Step 3: Optimization using a Parametric Plate Model

At this point, the first two steps of the optimization strategy have been implemented. The third step of the strategy is important because the model in this step considers the greatest number of variables of any model. For example in LP, it is necessary to include the impulse location variables that can generate various overlapping configurations or layouts. To do that, it is necessary to use the parametric plate model. However, the required 4-day CPU time forces us to use the proposed surrogate model.

Surrogate Model

The parameters that define an LP shot are pressure pulse magnitude, shape, and duration, spot shape and size, and amount of overlap. Two LP shots with the same parameters at two locations generate similar local residual stress fields. Therefore, the proposed surrogate model can be applied to the LP problem.

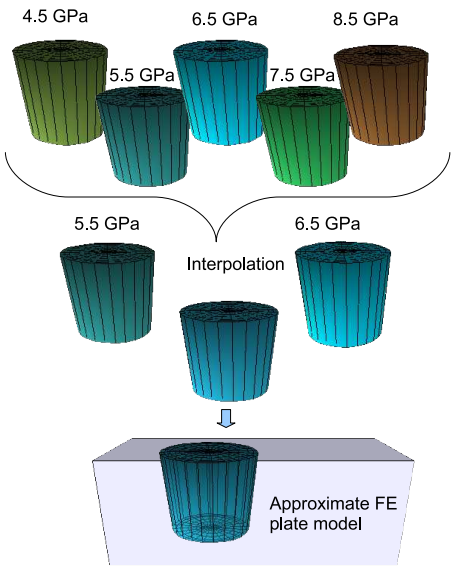

Figure 6.4: Schematic of combining database information to obtain desired stress field

For the parametric plate, three shot simulations are performed to extract the effects of individual parameters. Information collection take less time using three shot simulations than five-shot simulations. Once the individual parameters and interaction effects are extracted, they can be combined to approximate the residual stress profile for most configurations.

An example of the surrogate model is shown in Figure 6.4. This example is a schematic for only one variable (pressure magnitude). Suppose a design needs a residual stress field for 6.0 *GPa* pressure magnitude. The database is available for 4.5, 5.5, 6.5, 7.5, and 8.5 GPa pressure magnitudes. The database for each magnitude contains residual stress values at the plate nodes. To approximate the residual stress field for 6.0 GPa , the residual stress fields from 5.5 and 6.5 are used. Equation 6.1 shows the formulation to approximate the

residual stress field. Here $R_{(p)}$ indicate the residual stress field at pressure p.

$$R_{6.0} = \frac{6.0-5.5}{6.5-5.5}R_{5.5} + \frac{6.5-6.0}{6.5-5.5}R_{6.5} \tag{6.1}$$

Similarly an example for two variables, the five simulations at 4.5, 5.5, 6.5, 7.5, and 8.5 *GPa* are performed, and the local residual stress field at the laser spot is analyzed and saved. For the amount of overlap, simulations are performed for 0, 25, 50, 75 and 100% overlapping configurations. The effects of the second and the third shots at the same location are different from each other; therefore, the 100% overlapping configration for the third shot is performed seprately. To generate the residual stress field for five shots on different locations with 20% overlap for 2^{nd} to 5^{th} shots and 6.1 *GPa* pressure for all shots, the following process is used. The effects of the first shot are directly interpolated from the local residual stress fields of 5.5 and 6.5 *GPa* magnitudes. The second shot is interpolated from the local residual stress fields of 5.5 and 6.5 *GPa* pressure pulses and the local residual stress fields of the 0 and 25% overlap configurations.

Similarly, the approximate residual stress field can be generated for any number of shots on the plate. In this research, linear interpolation is used; however, depending upon the parametric investigations, this can be changed to higher-order interpolations. This approach does not need updates within the move limits. Just as with the surrogate model for the full 3*D* model, this also provides the residual stress field for all the nodes instead of a selected node. A

limited number of five-shot simulations are needed to construct the database because the fifth shot is often located at the center of the plate overlapping the previous four shots.

Surrogate Model Validation

The following investigations were performed to compare the estimates of the surrogate model with FE simulations. Four random peening configurations are selected. FE analysis is performed to determine the compressive stress volume, depth, and maximum magnitude. The surrogate model is also used to determine these quantities. Here, p_i indicates the pressure magnitude of the i^{th} shot, x_i indicates the x co-ordinate of the i^{th} shot location, and y_i indicates the y co-ordinate of the i^{th} shot location. The peening parameters in the first configuration are $p_1 = 4.1$, $p_2 = 5.3$, $p_3 = 4.6$, $p_4 = 5.1$, $p_5 = 3.9$, $x_1 = 3.6$, $x_2 = 5.8$, $x_3 = 2.9$, $x_4 = 5.6$, $x_5 = 4.1$, $y_1 = 3.8$, $y_2 = 3.2$, $y_3 = 6.4$, $y_4 = 5.8$, and $y_5 = 6.0$. The peening parameters in the second configuration are 4.7, 5.6, 4.3, 5.6, 4.7, 3.3, 6.4, 4.0, 5.6, 5.2, 3.1, 3.4, 5.7, 6.5, and 5.3. The peening parameters in the third configuration are 5.6, 4.2, 4.8, 4.6, 6.0, 2.6, 6.5, 4.3, 5.7, 5.0, 3.4, 2.9, 5.8, 5.9, and 4.6. The peening parameters in the fourth configuration are 5.5, 4.1, 5.7, 5.1, 5.1, 2.7, 6.4, 2.5, 6.4, 4.1, 4.4, 3.1, 5.9, 6.2, and 4.0.

Table 6.2 shows the results from both approaches. The comparison shows that the approximation and the FE models do not match exactly. However,

Table 6.2: Comparison of results from Surrogate and FEA models

	1		2		3		4	
	FEA	App.	FEA	App.	FEA	App.	FEA	App.
CV	34.7	26.7	43.1	32.8	44.9	32.4	42.5	33.5
MC	-419.7	-479.8	-563.1	-612.1	-529.6	-623.6	-479.2	-398.3
CD	0.63	0.54	0.63	0.63	1.00	1.13	0.75	0.75
MT	77.1	93.8	97.6	98.5	84.8	85.3	110.0	97.0

the surrogate model is able to capture the trends. The minimum errors in the compressive stress volume, depth, and maximum magnitude and tensile stress maximum magnitude are 21.2%, 0.0%, 8.7%, and 0.06%. The maximum errors are 27.8%, 14.3%, 17.7%, and 21.1%, respectively. Overall, the proposed surrogate model has the potential to be used in the optimization. An important aspect to note is that the finite element estimation took 4 CPU days, while the surrogate model estimation took just 10 CPU minutes.

Optimization Formulation and Results

The optimization formulation and results of the third step are provided below. Similar to the results of the previous two steps, the results show that a lower pressure magnitude is favored because of the residual stress profile constraint. The spot layout is shown in Figure 6.5. In this problem, the constraint on the residual stress profile and the maximum tensile stresses restricts the maximum

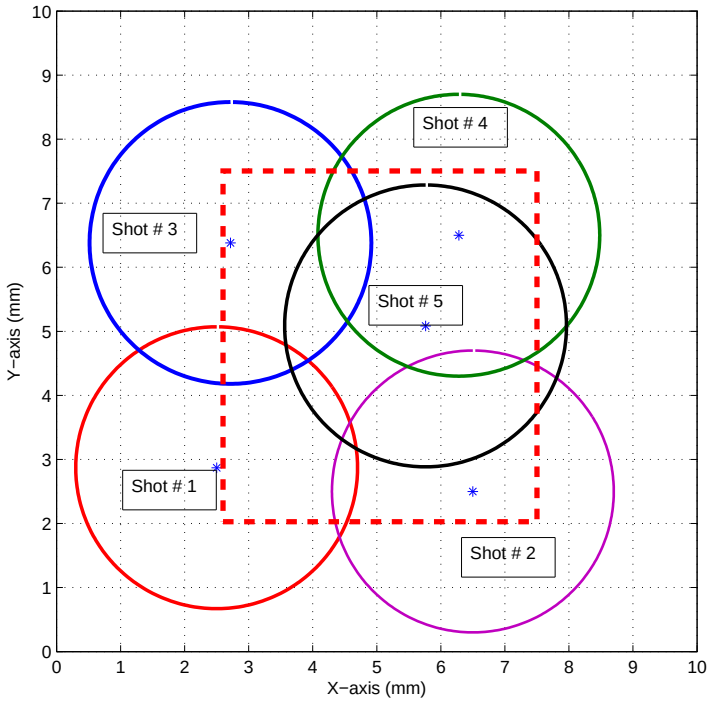

Figure 6.5: Optimal layout of the peening process

compressive stress magnitude and the compressive stress volume:

$$
\begin{aligned}
&\textit{Maximize}: && \textit{Compressive Stress Volume} \\
&\textit{Subjected to}: && \textit{Compressive Stress}(d) \geq \textit{Compressive Stress}(d+\Delta d) \\
& && \textit{Compressive Stress Depth} \geq 1.0 \ \textit{mm} \\
& && \textit{Maximum Tensile Stress} \leq 150 \ \textit{MPa},
\end{aligned}
$$

$$
\begin{aligned}
\textit{Variable Bounds}: \quad & 2.5 \leq x_i \leq 7.5 \, \textit{mm}, \\
& 2.5 \leq y_i \leq 7.5 \, \textit{mm}, \\
& 3.5 \leq p_i \leq 6.5 \, \textit{GPa}, \\
& 1 \leq n_i \leq 3,
\end{aligned}
$$

The optimization results are given in Table 6.3. In addition to achieving the set objective and complying with the constraints, the optimization is able

Table 6.3: Results of optimization strategy

Shot No.	Pressure magnitude(GPa)	Location x (mm)	Location y (mm)	Radius (mm)	No. of shots
1	4.42	2.5	2.87	2.28	1
2	4.67	6.5	2.5	2.28	1
3	4.53	2.72	6.38	2.28	1
4	6.20	6.28	6.5	2.28	1
5	4.37	5.76	5.08	2.28	1

to find a layout that covers the region of interest. The region of interest is in between 2.0 and 7.5 on both (x and y) axes and is shown by a red dotted line in Figure 6.5. The results indicate that for the formulated problem, a pressure magnitude of approximately 4.5 *GPa* can achieve the objective. The magnitude of the 4^{th} shot is different from the other shots at 6.2 *GPa*. A possible reason for this is that the 5^{th} shot overlaps the 4^{th} shot. Because of this overlap, the reduction of compressive stress at the center of the spot is negated by the subsequent shot. Another interesting result is that at all the locations the objective is achieved using only one shot.

6.4 Discussion

The optimization of structural components subjected to high-energy impulses can involve nonlinear elastic-plastic behavior, time-consuming finite element simulations, and mixed optimization variables. To solve such problems, this research develops the progressive multifidelity optimization strategy. The strat-

egy begins with parametric investigations using lower fidelity models to determine sensitive parameters and to localize the design space. In each step of the strategy, the design space is reduced and parameters are eliminated, with the goal of reaching an optimal solution.

The demonstration shows that pressure pulse magnitude, spot shape and size, and layout are critical parameters. The first step determines the shape and duration of the pressure pulse that is suitable for the formulated problems. In the second step, a bigger spot size is determined better for the given formulation. Based on the results from the first two steps, the problem is formulated for the third step. Finally, the third step determines a five-shot LP layout that can meet the requirements set forth in the optimization formulation. Compared to a traditional approach, the combination of three steps and the use of surrogate models substantially reduces the computational cost.

Overall, a progressive multifidelity optimization strategy is developed in this chapter. A surrogate model is proposed that can be used for impulse-type simulations. The proposed surrogate model accommodates the presence of repeated impulse loads. To effectively solve the optimization problem, modifications are introduced into PSO: LHS-based particle generation and a discrete variable handling technique. Computational time is further reduced by utilizing the parallel processing advantage of a population-based optimization technique. The strategy is validated and successfully employed to determine the optimal LP parameters. This design strategy and the proposed surrogate

model can be applied to other impulse-type problems with mixed variables of optimization.

Chapter 7

Summary and Future Directions

This chapter presents the contributions and summary of the research work performed in this dissertation. The tasks performed in this dissertation involve the development of simulation capabilities, surrogate models for a flat surface, optimization of a laser peening process at one-location, and optimization of a laser peening process at multiple-locations.

7.1 Contributions

7.1.1 FE Simulation

Modeling and Parameter Design of a Laser Peening Process. [68, 113]

A framework was developed for parametric simulations that can consider many of the LP variables. The framework incorporates a 3D model drawn from the literature. The 3D model was used to investigate the LP variables such as temporal variation of pressure, pressure pulse magnitude, and spot shape and size. Minor modifications to the symmetric 3D model allowed us to investigate com-

ponent thickness, a two-shot sequence at multiple locations, and a seven-shot sequence at multiple locations. These investigations led to following findings:

(i) Spot shape can be employed to the decrease maximum tensile stress without significantly compromising the maximum compressive stress.

(ii) An increase in pressure magnitude increases compressive depth, volume, and maximum stress; however, compared to the compressive stress, the increase in maximum tensile stress is greater.

(iii) The depth of compressive stress tends to increase with thickness and saturates after 5 *mm*. The maximum tensile stress first increases and then decreases with thickness.

(iv) Interaction of the induced residual stress profile of two sequential shots is dependent upon the distance between the two shots. The interaction exists even when there is no overlap.

(v) In the considered parameters and the geometric model (symmetric flat cylinder), there is no significant change in residual stress profile due to the sequence of shots; however, layout and number of shots show significant sensitivities.

7.1.2 Optimization

LP Optimization: One location

Modified PSO for Multimodal Mixed-variable Optimization. [114]

A modified PSO method is proposed to solve a multimodal mixed-variable op-

timization problem. The modified PSO employs a surrogate model, a niching strategy, and a mixed-variable handling technique: the surrogate model is employed to manage computational cost, the niching strategy is used to find and preserve multiple optima, and the mixed-variable technique is used to manage continuous and integer variables. The method is demonstrated on multiple test problems and on a one-location laser peening optimization. The solution of the laser peening problem provides the designer with multiple options. The designer can select the most suitable option, depending upon the component requirements.

(i) Multiple solutions exist to achieve the target residual stress profile.

(ii) Modified PSO handles mixed variables effectively and finds multiple optimal solutions.

(iii) Multiple shots at lower pressure at the same location create a higher depth of compressive stresses compared to a single shot of higher pressure.

(iv) One shot at higher pressure creates a higher magnitude the maximum compressive stress compared to multiple shots at lower pressure.

(v) An elliptical spot shape, compared to a circular spot shape, induces a lower magnitude of tensile stress for similar compressive stress magnitude.

Successful demonstration on multiple problems show that the proposed method can be employed to solve multimodal mixed-variable problems.

Mixed-variable Optimization Strategy Employing Multi-fidelity Simulation and Surrogate Models. [115,116]

A progressive, simulation-based, mixed-variable optimization strategy is developed. This strategy involves three steps and progressively employs axisymmetric, symmetric 3*D*, and parametric models. A surrogate model is proposed that can be used for impulse-type simulations. The proposed surrogate models accommodate the presence of repeated impulse loads. To effectively solve the optimization problem, two modifications are introduced into PSO: LHS-based particle generation and a discrete variable handling technique. Computational time is further reduced by utilizing the parallel processing advantage of a population-based optimization technique. The strategy is validated and successfully employed to determine the optimal LP parameters. This design strategy and the proposed surrogate model can be applied to other impulse-type problems with mixed optimization variables.

(i) A progressive three-step optimization strategy was developed that can be applied to nonlinear impulse type processes such as laser peening, shot peening, and bullet impacts on structures.

(ii) A surrogate model is proposed to alleviate the prohibitive computational cost of an iterative optimization process.

(iii) A parallel processing technique (MATLAB+PuTTy) is developed for ef-

fective population-based optimization.

7.2 Research Summary

Overall, a simulation capability is developed that includes a symmetric 3D model, a parametric plate, and rectangular bar coupon models. These models were employed to investigate the individual LP parameters, optimize single and multiple locations peening. The investigations and optimization assist an engineer to achieve desired residual stress profile. A multimodal mixed-variable optimization method was developed to solve the one-location laser peening optimization problem. The method modifies particle swarm optimization to incorporate multimodality and mixed-variable handling properties. A progressive multifidelity optimization strategy was developed to solve the multiple-location laser peening optimization problem. The PMOS combines modified PSO, LHS, mixed-variable strategy, and multifidelity surrogate models to solve a laser peening optimization problem.

7.3 Future Direction

The presented research work can be continued in many directions. The four major objectives can be reduction in the simulation time, parametric interactions effects, process optimization for a practical geometry, and uncertainty quantification of the LP process. The parametric investigations, optimization,

and uncertainty quantification can be simplified if the simulation time can be reduced by further research. Empirical formulations, surrogate models, and spectral finite element method [117] can be investigated for this purpose. The parametric investigations performed in this research are limited to one variable at a time, ignoring the interaction effects. It will be interesting to determine various interaction effects of the parameters.

Determining optimized process parameters for a practical 3D problem can be very useful for the industrial application. This is possible by aggressively employing surrogate model. Surrogate models developed in this research can be advanced to use in a practical problem such as aircraft lug. As discussed in the dissertation, LP is a mixed-variable process. The development of a mixed-variable uncertainty quantification method can assist in uncertainty quantification of the LP process. Additional potential areas include experimental validation of multiple-location peening, optimization, and fatigue life optimization strategies [118]. This experimental work will not only provide additional validation of the simulation work but also facilitate the development of an optimization strategy for practical surface enhancement and fatigue problems.

Bibliography

[1] Clauer, A. H., Fairand, B. P., and Wilcox, B. A., "Laser Shock Hardening of Weld Zones in Aluminum Alloys," *Metallurgical Transactions A*, Vol. 8A, 1977, pp. 1871–1876.

[2] Clauer, A. H., Fairand, B. P., and Wilcox, B. A., "Pulsed Laser Induced Deformation in an Fe-3 Wt Pct Si Alloy," *Metallurgical Transactions A*, Vol. 8A, 1977, pp. 119–125.

[3] Fairand, B. P., Clauer, A. H., Jung, R. G., and Wilcox, B. A., "Quantitive Assessment of Laser-Induced Stress Waves Generated at Confined Surfaces," *Applied Physics Letters*, Vol. 25(8), 1974, pp. 431–433.

[4] Fairand, B. P. and Clauer, A. H., "Laser Generated Stress Waves: Their Characteristics and Their Effects to Materials," *Laser-Solid Interactions and Laser Processing*, Vol. 50(1), 1979, pp. 27–42.

[5] Fairand, B. P. and Clauer, A. H., "Laser Generation of High-amplitude Stress Waves in Materials," *Journal of Applied Physics*, Vol. 50(3),

1978, pp. 1497–1502.

[6] Peyre, P., Fabbro, R., Merrien, P., and Lieurade, H. P., “Laser Shock Processing of Aluminium Alloys. Application to High Cycle Fatigue Behavior,” *Material Science and Engineering*, Vol. A210, 1996, pp. 102–113.

[7] Peyre, P., Berthe, L., Scherpereel, X., and Fabbro, R., “Laser-shock Processing of Aluminium-coated 55C1 Steel in Water-confinement Regime, Characterization and Application to High-cycle Fatigue Behavior,” *Journal of Material Science*, Vol. 33, 1998, pp. 1421–1429.

[8] Braisted, W. and Brockman, R., “Finite Element Simulation of Laser Shock Peening,” *International Journal of Fatigue*, Vol. 21(7), 1999, pp. 719–724.

[9] Nam, T., *Finite Element Analysis of Residual Stress Field Induced by Laser Shock Peening*, PhD Dissertation, The Ohio State University, Columbus, OH, 2002.

[10] Noll, S. A., *Residual Stress Fields Due to Laser-Pulse-Generated Shock Waves*, Master’s thesis, The Ohio State University, Columbus, OH, 1999.

[11] Ding, K. and Ye, L., “Three Dimensional Dynamic Finite Element Analsyis of Multiple Laser Shock Peening Processes.” *Surface Engineering*, Vol. 19(5), 2003, pp. 351–358.

[12] Vanluchene, R., Johnson, J., and Carpenter, R., “Induced Stress Relationships for Wing Skin Forming by Shot Peening,” *Journal of Materials Engineering and Performance*, Vol. 4(3), 1995, pp. 283–290.

[13] Niku-Lari, A., *First International Conference on SHOT PEENING*, Pergamon Press, Paris, 1982.

[14] Eckersley, J. S. and Champaigne, J., *Shot Peening: Theory and Application*, IITT International, Gournay-sur-Marne, France, 1991.

[15] Wagner, L., *Shot Peening*, WILEY-VCH Verlag GmbH & Co. KGaA, Weinheim, Germany, 2006.

[16] Honda, T., Ramulu, M., and Kobayashi, A., “Fatigue of shot peening 7075-T7351 SENB Specimen - A 3-D Analysis,” *Journal of Fatigue & Fracture of Engineering Materials & Structures*, Vol. 29, January 2006, pp. 416–424.

[17] Johnson, W., “Parametric Two-dimensional Finite Eelement Investigation: Shot Peening of High-strength Steel,” *AIAA Journal*, Vol. 44(9), 2006, pp. 1973–1982.

[18] Kolcke, F. and Lier, J., “Roller Burnishing for Hard Turned Surface,” *International Journal of Machine Tools and Manufacture*, Vol. 38 (5/6), 1998, pp. 419–423.

[19] Prevey, P. S., Teleman, J., Gabb, J. T., and Kantzos, P., “FOD Resistance and Fatigue Ccrack Arrest in Low Plasticity Burnished IN718,” *5th National Turbine High cycle fatigue conference, Chandler, AZ, March 7-9*, 2000, pp. 1–12.

[20] Arola, D., McCain, M. L., Kunaporn, S., and Ramulu, M., “Waterjet and Abrasive Waterjet Surface Treatment of Titanium: a Comparison of Surface Texture and Residual Stress,” *An International Journal on the Science and Technology of Friction, Lubrication and Wear*, Vol. 249 (10-11), 2002, pp. 943–950.

[21] Ramulu, M., Kunaporn, S., Arola, D., Hashish, M., and Hopkins, J., “Waterjet Machining and Peening of Metals,” *Journal of Pressure Vessel Technology*, Vol. 122(1), 2000, pp. 90–95.

[22] Kunaporn, S., Ramulu, R., and Hashish, M., “Mathematical Modeling of Ultra-High-Pressure Waterjet Peening,” *Journal of Engineering Materials and Technology*, Vol. 127, 2005, pp. 186–191.

[23] Bertolotti, M., *The History of Laser*, Bristol : Institute of Physics Publisher, 2005.

[24] Csele, M., *Fundamentals of Light Source and Lasers*, Wiley, Hoboken, NJ, September 2004.

[25] Kolsky, H., *Stress waves in Solids*, Dover Publications, Inc., NewYork, USA, 1963.

[26] Meyers, M. A., *Dynamic Behavior of Materials*, John Wiley & Sons, Inc., NewYork, USA, 1994.

[27] Ballard, P., *Contraintes Residuelles Induites par Impact Rapide, Application au Choc-Laser*, PhD Dissertation, Ecole Polytechnique, Paris, France, 1991.

[28] Ballard, P., Fournier, J., Fabbro, R., and Frelat, J., "Residual Stresses Induced by Laser-shock," *Journal of Physics III*, Vol. 1(c3), 1991, pp. 487–494.

[29] White, R. M., "Elastic Wave Generation by Electron Bombardment or Electromagnetic Wave Absorption," *Journal of Applied Physics*, Vol. 34, 1963, pp. 2123–2124.

[30] Ready, J., "Effects Due to Absorption of Laser Radiation," *Journal of Applied Physics*, Vol. 36, 1965, pp. 462–468.

[31] Neuman, F., "Momentum Transfer and Cratering Effects Produced by Giant Laser Pulses," *Applied Physics Letters*, Vol. 4(9), 1964, pp. 167–169.

[32] Gregg, D. W. and Thomas, S. J., "Momentum Transfer Produced by Focused Laser Giant Pulses," *Journal of Applied Physics*, Vol. 37(7), 1966, pp. 2787–2789.

[33] Malozzi, P. and Fairland, B. P., *Altering Material Properties*, US Patent 3,850,698, 1974.

[34] Metz, S. A. and Smith, F. A., “Production of Vacancies by Laser Bombardment,” *Applied Physics Letters*, Vol. 19(6), 1971, pp. 207–208.

[35] Yang, L. C. and Menichelli, V. J., “Detonation of Insensitive High Explosives by a Q-Switched Ruby Laser,” *Applied Physics Letters*, Vol. 19(11), 1971, pp. 473–475.

[36] Fairand, B. P., Wilcox, B. A., Gallagher, W. J., and Williams, D. N., “Laser shock-induced Microstructural and Mechanical Property changes in 7075 Aluminum,” *Journal of Applied Physics*, Vol. 43(9), 1972, pp. 3893–3895.

[37] Anderhlom, N. C., “Laser-generated Stress Waves,” *Applied Physics Letters*, Vol. 16(1), February 1970, pp. 113–14.

[38] Clauer, A. H., Walters, C. T., and Frod, S. C., “The effects of Laser Shock Peening on the Fatigue Properties of 2024-T3 Aluminum,” *Lasers in Materials Processing, American Society of Metals, Metals Park, OH*, Vol. 7, 1983, pp. 7–22.

[39] Clauer, A. H., “Laser Shock Processing Increases the Fatigue Life of Metal Parts,” Materials & Processing Report 6(6), LSP Technology, Dublin, OH, August 1991.

[40] Fox, J. A., “Effect of Coating on Laser-irradiated Targets,” *Applied Physics Letters*, Vol. 24, 1974, pp. 461–464.

[41] Ford, S. C., Fairand, B. P., Clauer, A. H., and Galliher, R. D., “Investigation of Laser Shock Processing,” Tech. rep., AFWAL-TR-80-3001, Wright-Patterson Airforce Base, Ohio, 1976.

[42] Ortiz, A. L., Penny, C. M., Jones, M. G., and Erikson, C. E., *Laser Peening System and Method*, US Patent 4,937,421, 1990.

[43] Forget, P., Strude, J., Jeandin, M., Lu, J., and Castex, L., “Laser Shock Surface Treatment of Ni-based Superalloys,” *Materials and Manufacturing Processes*, Vol. 5(4), 1990, pp. 501–528.

[44] Brar, N. S., Hopkins, A., and Laber, M. W., “Laser Shock Peening of Titanium 6-4 Alloy,” *Shock Cmpression of Condensed Matter, American Intitute of Physics Conference Proceeding, Gaithersburg*, Vol. 505, 2000, pp. 435–438.

[45] Chu, J. P., *Microstructure and Mechanical Properties of Laser Shocked Iron-Based Alloys*, PhD Dissertation, University of Illinois, Urbana-Chanpaign, IL, 1992.

[46] Mannava, S. R. and Cowie, W. D., *Laser Shock Peening Disk with Loading and Locking Slots for Turbomachinery*, US Patent 5,522,706, 1996.

[47] Ferrigno, S. J., Cowie, W. D., and Mannava, S. R., *Laser Shock Peening for Gas Turbine Engine Weld Repair*, US Patent 5,735,044, 1998.

[48] Clauer, A. H., Bolbbrook, J. H., and Fairand, B. P., *Effect of Laser Induced Shock Wave on Metals*, M.A. Meyers and L.E. Murr (eds) Plenum Publishing Corporation, New-York, 1981.

[49] Forget, P. and Jeandin, M., "Dformation Lchelle Cristallographique Dd'alliages Base de Nickel Mono- et polycristallins par Choc Laser en Mode Confin," *Journal of Physics III, France*, Vol. 5(8), 1995, pp. 1133–1144.

[50] Sano, Y., Mukai, N., Okazaki, K., and Obata, M., "Residual Stress Improvement in Metal Surface by Underwater Laser irradiation," *Nuclear Intruments and Methods in Physics, Research B*, Vol. 121, 2004, pp. 432–436.

[51] Hong, X., Wang, S. B., Guo, D. H., Wu, H. X., Wang, J., Dai, Y. S., Xia, X. P., and Xie, Y. N., "Confining Medium and Absorptive Overlay : Their Effets on a Laser-induced Shock Wave," *Journal of Optics and Laser in Engineering*, Vol. 29, 1998, pp. 447–455.

[52] Staver, P. H. and Unternahrer, J. R., *Method and Apparatus for Shaping a Laser Pulse*, US Patent 5,987,042, 1999.

[53] Fabbro, R., Peyre, P., Berthe, L., and Scherpereel, X., "Physics and Applications of Laser-shock Processing," *Journal of Laser Applications*, Vol. 10(6), 1998, pp. 265–279.

[54] Wu, B. and Shin, Y. C., "A Self-closed Thermal Model for Laser Shock Peening Under the Water Confinement Regime Vonfiguration and Comparisons to Experiments," *Journal of Applied Physics*, Vol. 97, 2005, pp. 113517(1)–113517(11).

[55] Wu, B. and Shin, Y. C., "From Incident Laser Pulse to Residual Stress: A Complete and Self-Closed Model for Laser Shock Peening," *Journal of Manufacturing Science and Engineering*, Vol. 129(1), 2007, pp. 117–125.

[56] Love, A. E. H., *A Treatise on the Mathematical Theory of Elasticity*, Dover Publications, NewYork, 1944.

[57] Clauer, A. H. and Lahrman, D. F., "Laser Shock Processing as a Surface Enhancement Process," *Key Engineering Materials (Switzerland)*, Vol. 197 (1), 2001, pp. 121–144.

[58] Peyre, P., Sollier, A., Chaieb, I., Berthe, L., Braham, C., and Farbbro, R., "FEM Simulation of Residual Stresses Induced by Laser Peening," *The European Physical Journal Applied Physics*, Vol. 23, 2003, pp. 83–88.

[59] Peyre, P., Chaieb, I., and Braham, C., "FEM Calculations of Residual Stresses Induced by Laser Shock Processing in Stainless Steels," *Mod-*

elling and Simulations in Material Science and Engineering, Vol. 15, 2007, pp. 205–221.

[60] Ding, K. and Ye, L., *Laser Shock Peening Performance and Process Simulation*, Woodhead Publishing Limited, Cambridge, England, 2006.

[61] Zhang, W., Tao, Y. L., and Noyan, I. C., "Microscale Laser Shock Peening of Thin Films, Part 1: Experiment, Modeling and Simulation," *Journal of Manufacturing Science and Engineering*, Vol. 126, 2004, pp. 10–17.

[62] Lawrence, W. L. and Klaassen, R. E., *Method for Setting Up and Controlling Confinement Media Flow in Laser Shock Peening*, US Patent 6,333,488, 2001.

[63] Clauer, A. H., Toller, S. M., and Dulaney, J. L., *Beam Path Clearing for Laser Peening*, US Patent 6,521,860, 2003.

[64] Barker, L. M. and Hollenbach, R. E., "Laser Interferometer for Measuring High Velocities of Any Reflecting Surface," *Journal of Applied Physics*, Vol. 43(11), 1972, pp. 4669–4675.

[65] Fleming, K. J. and Broyles, T. A., "Shock Analysis using the Multipoint Velocimeter (VISAR)," Tech. rep., SAND2003-3759, Sandia National Laboratories, Albuquerque, NM, 2003.

[66] Johnson, G. R. and Cook, W. H., “A Constitutive Model and Data for Metals Subjected to Large Strains, High Rates and High Temperatues,” *Proceedings of the Seventh International Symposium on Ballistics, The Netherlands*, 1983, pp. 541–547.

[67] Lesuer, D. R., “Experimental Investigations of Material Models for Ti-6Al-4V Titanium and 2024-T3 Aluminum,” Tech. rep., DOT/FAA/AR-00/25, Lawrence Livermore National Laboratory, Livermore, CA, 2000.

[68] Amarchinta, H., Singh, G., Grandhi, R. V., and Stargel, D. S., “Validation of Material Models for a High-strain Rate Process,” 12^{th} *AIAA/ISSMO Multidisciplinary Analysis and Optimization Conference, Vitoria, Canada*, 2008, p. submitted.

[69] Systemes, D., *ABAQUS user’s Mannual Version 6.6*, Hibbitt, Karlsson & Sorensen Inc, Pawtucket(RI), USA, 2006.

[70] Reddy, J. N., *An Introduction to Nonlinear Finite Element Aanalysis*, Oxford University Press Inc., New York, 2004.

[71] Cook, R. D., Malkus, D. S., Plesha, M. E., and Witt, R. J., *Concepts and Applications of Finite Element Analysis*, John Wiley and Sons, Inc., New York, 4th ed., 2001.

[72] Newmark, N. M., “A Method of Computation for Structural Dynamics,” *ASCE Journal of the Engineering Mechanics Division*, Vol. 32 (EM3), 1959, pp. 67–94.

[73] OSC, “High Performance Computing Systems,” 2009, available at http://www.osc.edu/supercomputing/hardware/.

[74] Land, A. H. and Doig, A. G., “An Automatic Method of Solving Discrete Programming Problems,” *Econometrica*, Vol. 28(3), 1960, pp. 497–520.

[75] Holland, J. H., *Adaptation in Natural and Artificial Systems*, Univeristy of Michigan Press, Ann Arbot, 1975.

[76] Goldberg, D. E., *Genetic Algorithm in Search, Optimization, and Machine Learning*, Addison-Wesley, New York, NY, 1989.

[77] Kennedy, J. and Eberhart, R. C., “Particle Swarm Optimization,” *Procedding of IEEE conference on Neural Network, IV, Piscataway, NJ*, 1995, pp. 1942–1948.

[78] Singh, G., Wynne, S., and Vanhorn, M., “Utilising the Ohio Supercomputing Center for Computationally Intensive Simulation Processes,” 2009, Unpublished Project Report for EGR 535, Technical Communications for Engineers and Computer Scientist.

[79] Bhuvaneshwaran, V., Langari, R., and Temponi, C., “A Genetic Algorithm and Fuzzy Approach (GAFA) for Constraint Nonlinear Optimization in Design,” *International Journal of Computational Methods in Engineering Science and Mechanics*, Vol. 7(3), July 2006, pp. 173–189.

[80] Ghanmi, S., Guedri, M., Bouazizi, M.-L., and Bouhaddi, N., “Use of Metamodels in the Multi-Objective Optimization of Mechanical Structures with Uncertainties,” *International Journal of Computational Methods in Engineering Science and Mechanics*, Vol. 8(5), 2007, pp. 283–302.

[81] Antonio, C. A. C., “A Hierarchical Genetic Algorithm with Age Structure for Multimodal Optimal Design of Hybrid Composites.” *Structural and Multidisciplinary Optimization*, Vol. 31(4), 2006, pp. 280–294.

[82] Bochenek, B. and Forys, P., “Structural Optimization for Post-buckling Behavior Using Particle Swarm,” *Structural and Multidisciplinary Optimization*, Vol. 32(6), 2006, pp. 521–531.

[83] Venter, G. and Sobieszczanski-Sobieski, J., “Multidisciplinary Optimization of a Transport Aaircraft Wing using Particle Swarm Optimization,” *Structural and Multidisciplinary Optimization*, Vol. 26(1/2), 2004, pp. 121–131.

[84] Deb, K., *Optimization of Engineering Design: Algorithm and Examples*, Prentice-Hall of India Pvt. Ltd., New Delhi, India, 2005.

[85] Olsen, G. N. and Vanderplaats, G. N., “Method for nonlinear optimization with discrete variables.” *AIAA Journal*, Vol. 27(11), 1989, pp. 1584–1589.

[86] Sedlaczek, K. and Eberhard, P., “Using augmented Lagrangian Particle Swarm Optimization for Constrained Problems in Engineering,” *Structural and Multidisciplinary Optimization*, Vol. 32(4), 2006, pp. 277–286.

[87] Seo, J.-H., Im, C.-H., Kim, J.-K., Jung, H.-K., and Lee, C.-G., “Multimodel Function Optimization Based on Particle Swarm Optimization,” *IEEE Transactions on Magnetics*, Vol. 42(4), 2006, pp. 1095–1098.

[88] Kitayama, S., Arakawa, M., and Yamazaki, K., “Penalty Function Approach for the Mixed Discrete Nonlinear Problems by Particle Swarm Optimization,” *Structural and Multidisciplinary Optimization*, Vol. 32(3), 2006, pp. 191–202.

[89] AlRashidi, A. R. and El-Hawary, M. E., “Hybrid Particle Swarm Optimization Approach for Solving the Discrete OPF problem considering the value loading effect,” *IEEE Transactions on Power Systems*, Vol. 22, 2007, pp. 2030–2038.

[90] Seo, J.-H., Im, C.-H., Kwak, S.-Y., Lee, C.-G., and Jung, H.-K., “An Improved Particle Swarm Optimization Algorithm Mimicking Territorial Dispute Between Groups for Multimodal Function Optimization Problems,” *IEEE Transactions on Magnetics*, Vol. 44(6), 2008, pp. 1046–1049.

[91] Singh, G. and Deb, K., “Comparison of Multi-modal Optimization Algorithms Based on Evolutionary Algorithms,” *Proceedings of the 8th annual conference on Genetic and evolutionary computation, Seattle, WA*, 2006, pp. 1305–1312.

[92] Parsopoulos, K. E. and Vrahatis, M. N., “Modification of the Particle Swarm Optimizer for Locating all the Gglobal Minima,” *Artificial Neural Networks and Genetic Algorithms, Prague, Czech Republic*, 2001, pp. 324–327.

[93] Brits, E., Engelbrecht, A., and van der Bergh, F., “A niching Particle Swarm Optimizer,” *Proceedings of the 4th Asia-Pacific Conference on Simulated Evolution and Learning, Singapore*, 2002, pp. 692–696.

[94] Shin, D. K., Gurdal, Z., and Griffin(Jr), O. H., “A Penalty Approach For Nonlinear Optimization With Discrete Design Variables,” *Engineering Optimization*, Vol. 16(1), 1990, pp. 29–42.

[95] Fourie, P. C. and Groenwold, A. A., “The Particle Swarm Algorithm in Size and Shape Optimization,” *Structural and Multidisciplinary Optimization*, Vol. 23(4), 2002, pp. 259–267.

[96] Schuttle, J. and Groenwold, A. A., “Sizing Design of Truss structures using Particle Swarm Optimization,” *Structural and Multidisciplinary Optimization*, Vol. 31(1), 2003, pp. 93–108.

[97] Srivastava, A., Hacker, K., Lewis, K., and Simpson, T. W., “A Method for using Legacy Data for Metamodel-based Design of Large-scale Systems,” *Structural and Multidisciplinary Optimization*, Vol. 28(2/3), 2004, pp. 146–155.

[98] Li, G., Azarm, S., Farhang-Mehr, A., and Diaz, A. R., “Approximation of multiresponse deterministic Engineering Simulations: A Dependent Metamodeling Approach,” *Structural and Multidisciplinary Optimization*, Vol. 31(4), 2006, pp. 260–269.

[99] Rajan, S. D. and Nguyen, D. T., “Design of Optimization of Discrete Structural System using MPI-enabled genetic algorithm,” *Structural and Multidisciplinary Optimization*, Vol. 28(1), 2004, pp. 340–348.

[100] Kalivarapu, V. K., Foo, J. L., and Winer, E. H., “Improving Solution Characteristics of Particle Swarm Optimization using Digital Pheromones,” *Structural and Multidisciplinary Optimization*, Vol. 37(4), 2008, pp. 415–427.

[101] Hatamleh, O., Lyons, J., and Forman, R., “Laser and Shot Peening Effects on Fatigue Crack Growth in Friction Stir Welded 7075-T7351 Aluminum Alloy Joints,” *International Journal of Fatigue*, Vol. 29(3), 2007, pp. 421–434.

[102] Warren, A. W., Guo, Y. B., and Chen, S. C., “Massive Parallel Laser Shock Peening: Simulation, Analysis and Validation,” *International*

Journal of Fatigue, Vol. 30, 2008, pp. 188–197.

[103] Choi, S. K., Grandhi, R. V., and Canfield, R. A., *Reliability-based Structural Design*, Springer, London, 2006.

[104] Ratnaweera, A., Halgamuge, S., and Watson, H., "Self-organizing hierarchical particle swarm optimizer with time-varying acceleration coefficient." *IEEE Transactions on Evolutionary Computation*, Vol. 8(3), 2004, pp. 240–255.

[105] Livne, E. and Navarro, I., "Nonlinear Equivalent Plate Modeling of Wing Box Structures." *AIAA Journal of Aircraft*, Vol. 36(5), 1999, pp. 851–865.

[106] Robinson, T. D., Eldred, M. S., Willcox, K. E., and Haimes, R., "Surrogate-based Optimization Using Multifidelity Models with Variable Parameterization and Corrected Space Mapping," *AIAA Journal*, Vol. 46(11), 2008, pp. 2814–2822.

[107] Chen, S., Xiong, Y., and Chen, W., "Multiresponse and Multistage Metamodelaing Approach for Design Optimziation," *AIAA Journal*, Vol. 47(1), 2009, pp. 206–218.

[108] Glaz, B., Goel, T., Liu, L., Friedmann, P., and Haftka, R., "Multiple-Surrogate Approach to Helicopter Rotor Blade Vibration Reducation." *AIAA Journal*, Vol. 47(1), 2009, pp. 271–282.

[109] Kim, C., Wang, S., and Choi, K. K., "Efficient Response Surface Modeling by Using Moving Least-Squares Method and Sensitivity," *AIAA Journal*, Vol. 43(11), 2001, pp. 2404–2411.

[110] Jin, R., Chen, W., and Simpson, T. W., "Comparative Studies of Metamodeling Techniques Under Multiple Criteria," *Structural and Multidisciplinary Optimization*, Vol. 23(1), 2001, pp. 1–13.

[111] Clauer, A., Walters, C. T., and Frod, S. C., "The effects of Laser Shock Peening on the Fatigue Properties of 2024-T3 Aluminum," *Lasers in Materials Processing, American Society of Metals, Metals Park, OH*, Vol. 7, 1983, pp. 7–22.

[112] Zu, J. and Behdinan, K., "Reliability-based Design Optimization of Cantilever Beams Under Fatigue Constraint," *AIAA Journal*, Vol. 45, 2008, pp. 2737–2746.

[113] Singh, G., Grandhi, R. V., and Stargel, D. S., "Modeling and Parameter Design of a Laser Shock Peening Process," *International Journal of Computational Methods in Engineering Science and Mechanics (in print)*, 2008.

[114] Singh, G. and Grandhi, R. V., "Modified PSO for Multimodal Mixed-variable Optimization of a Laser Shock Process." *Structural and Multidisciplinary Optimization Journal (Submitted, SMO-09-0049)*, 2009.

[115] Singh, G., Grandhi, R. V., Stargel, D. S., and Langer, K., “Modeling and Optimization of a Laser Shock Peening Process, AIAA-2008-5838,” 12^{th} *AIAA/ISSMO Multidisciplinary Analysis and Optimization Conference, Victoria, Canada*, 2008, pp. 5838–5850.

[116] Singh, G. and Grandhi, R. V., “Mixed-variable Optimization Strategy by Employing Multi-fidelity Simulation and Surrogate Models,” *AIAA Journal (resubmitted after minor revisions, 43469)*, 2009.

[117] Gopalakrishnan, S., Chakraborty, A., and Mahapatra, D. R., *Spectral Finite Element Method: Wave Propagation, Diagnostics and Control in Anisotropic and Inhomogeneous Structures*, Springer-Verlag New York, LLC, 2008.

[118] Singh, G., Spradlin, T. J., and Grandhi, R. V., “Fatigue Life Optimization using Laser Shock Peening Process, AIAA-2009-2184,” *50th Structures, Structural Dynamics, and Materials Conference, May 4-7, 2009, Palm Springs, California, USA.*, 2009, pp. 2184–2193.